The Dissertation Committee for Collin David Davies certifies that this is the approved version of the following Dissertation:

Electrochemically Generated Ion Depletion Zones for Continuous Separations in Microelectrochemical Devices

Committee:

Richard M. Crooks, Supervisor

Charles Buddie Mullins

Jason B. Shear

Lynn E. Katz

Matthew T. Balhoff

Electrochemically Generated Ion Depletion Zones for Continuous Separations in Microelectrochemical Devices

by

Collin David Davies

Dissertation

Presented to the Faculty of the Graduate School of

The University of Texas at Austin

in Partial Fulfillment

of the Requirements

for the Degree of

Doctor of Philosophy

The University of Texas at Austin

May, 2020

Dedication

To those whose dreams of higher education are yet unrealized.

Acknowledgements

All glory, honor, and praise is due only to my Heavenly Father. Your constant presence sustains me and Your unconditional love and favor guarantee that I have all that I need. Apart from You, I am nothing. In Your presence is found fullness of joy. I am confident of that.

I have to start by thanking my beautiful bride, JC. From encouraging me to pursue a graduate degree to tirelessly cheering me on, reminding me of what is true, and committing to stand with me through every moment of this season, you have loved me with all of your being. That means the world to me.

To my parents, you have sacrificed more than I will ever know to champion my interests and dreams. Mom, you have instilled in me a curiosity for the world around me. Dad, you have modeled for me the most dogged, yet balanced work ethic I have ever witnessed. Both of you have taught me the value of integrity, given me the confidence to tackle difficult problems, and gifted me the freedom of knowing that your delight in me does not depend on my performance. Thank you.

I would like to gratefully acknowledge my research advisor, Prof. Dick Crooks. Dick, you have faithfully

provided the resources, time, and attention necessary for me to explore interesting and challenging research. You have encouraged my professional growth through conferences, writing opportunities, and mentorships. Because of your investment, I am a more competent scientist, refined communicator, and creative thinker than I was nearly five years ago.

To the members of the Crooks Laboratory, you have made the daily routine of graduate school a rich and memorable experience. You are a caring, kind, and welcoming group. Logan, I have enjoyed sharing a desk with you. I couldn`t imagine it any other way. Morgan, Eunsoo, and Jan, thank you for taking me under your wings during my first years in the group. I owe a lot of my success to your willingness to mentor me. Jon and Sarah, you are incredibly bright and talented individuals and I have enjoyed the chance to tackle meaningful and challenging science alongside you. I am excited to see where the next five years will take each of you.

I would also like to thank the incredible staff members at The University of Texas at Austin who have made my research progress possible. Angie, you are a details wizard. I appreciate you. Tim and Adam, you and your shops have provided respite for me on many occasions. Both of you are generous with your time and incredible listeners.

Raluca, thank you for taking my phone calls from the cleanroom and maintaining high quality instrumentation. Xiaole (Joy), thank you for advocating for me and my computational needs.

Abstract

Electrochemically Generated Ion Depletion Zones for Continuous Separations in Microelectrochemical Devices

Collin David Davies, Ph.D.

The University of Texas at Austin, 2020

Supervisor: Richard M. Crooks

The separation of chemical mixtures into pure and purer constituents is essential to humankind. However, the most common techniques for chemical separations are energy intensive and improvements in their efficiency are only incremental. To meet the rising demands of an ever-increasing global population, new techniques that separate chemicals on the basis of phenomena fundamentally different than that of the existing methods must be developed. To that end, we set out nearly five years ago with the goal to continuously separate charged objects within ion depletion zones formed by electrochemical processes in microfluidic channels. Ion depletion zones yield co-located electric field gradients that interact with charged objects in solution in a manner related to the electrophoretic mobilities of the objects. Importantly, by judiciously

tuning the forces of electromigration and convection in microchannels, the motion of charged objects can be controlled in useful ways.

Herein, we report three studies that describe our scientific progress thus far toward the stated goal. The first study outlines the processes fundamental to controlling the flow of charged objects with a local electric field gradient. The key finding from this study is that an electric field gradient in the vicinity of a channel bifurcation directs the flow of nearly 100% of charged microplastic particles into a specific outlet channel. The second study introduces a more sophisticated microelectrochemical device than that used in the first study. In this case, two electric field gradients formed within a trifurcated microchannel continuously sort and separate two microplastics having different electrophoretic mobilities. The third study investigates electrochemically oxidizing Cl^- to neutral Cl_2 to form ion depletion zones in Cl^--containing solutions like seawater. Success in this endeavor would make it possible to leverage the discoveries from the first two studies in which the ion depletion zones formed in Tris buffer solutions to chemical separations in an environmentally relevant solution. The main finding from the third study, however, is that electrochemically generated Cl_2 rapidly reacts in water to form an ion

enrichment zone, rather than an ion depletion zone, in solution. Notwithstanding, these findings represent significant advancements in our understanding of the processes fundamental to continuously separating charged objects within ion depletion zones and electric field gradients formed by electrochemical processes.

Table of Contents

List of Tables

List of Figures

List of Illustrations

Chapter One: Introduction

1.1 Motivation and objectives

Modern humanity depends on many important chemical separations performed daily on an industrial scale.[1] The majority of separation strategies utilize thermal distillation techniques invented more than 1000 years ago and separate chemical species by boiling point.[2,3] Because of the historical dependence on distillation techniques, which are energy intensive, chemical separations account for 10-15% of energy consumption worldwide.[2] Alternative membrane-based separation strategies mitigate the energy demand of distillation, yet prove challenging to scale up and possess intrinsic limitations. For example, membranes usually separate species based on size and charge exclusion mechanisms.[4-6] Notably, improvements in the selectivity of membranes almost always lead to lower permeability, and vice versa.[7-12] While ongoing research in the field of membrane-based separations seeks to break through the scaling relationship between membrane selectivity and permeability, as well as improve membrane lifetime and stability, advancements in these areas are incremental. For these reasons, it is essential to develop alternative approaches to chemical separations.

One of the most promising alternative strategies for chemical separations utilizes electric field gradients (EFGs) to control the motion of charged objects in solution.[13-17] *Charged objects experience enhanced electromigration within EFGs. Accordingly, the motion of charged objects can be controlled in beneficial ways by judiciously tuning the forces of electromigration and convection acting on the objects.*

Some of the earliest reports describing EFG-based separations relied on selective transport phenomena at nanopores or at permselective membranes to form EFGs in micron-scale channels.[18-22] *These experimental configurations could be thoroughly described by numerical simulations, which resulted in rapid advancement in understanding the behavior of separations along EFGs.*[23-26] *However, nanopores and membranes are difficult to integrate into microfluidic systems,*[27,28] *are prone to failure by fouling and clogging,*[29-32] *and exhibit non-ideal permselectivity.*[7,33]

In 2008, our group developed a membrane-free electrochemical approach to form EFGs in microfluidic systems containing buffered solutions.[34,35] *This was a significant finding and enabled potential control over the formation of EFGs at mechanically robust electrodes, which we fabricated using standard photolithography procedures.*

Subsequent work defined the principles fundamental to forming EFGs by electrochemical reaction in buffered solutions and applied this understanding to enrich or deplete charged objects within straight microchannels.[36-40] *Ultimately, the pinnacle of this incipient research was the 500,000-fold enrichment of a fluorescent tracer in 150 min.*[38] *However, the long-term goal of this work is to continuously control the flow of charged objects using EFGs formed by electrochemical processes in solutions of more environmental relevance than inorganic buffer solutions.*

Therefore, the objectives of the research discussed in this dissertation are twofold. The first objective is to develop a thorough understanding of how EFGs formed by electrochemical processes can be utilized to continuously manipulate the flow of charged objects in forked microchannels. The second objective is to investigate an additional electrochemical approach to form EFGs in environmentally relevant solutions (e.g., natural waters). A combination of experimental and computational methods were carried out to address these objectives. The results of efforts focused on the first objective are presented in Chapters 3 and 4, while the results of efforts focused on the second objective are presented in Chapter 5.

1.2 Background

1.2.1 Ion depletion zones and electric field gradients

One of the most interesting strategies to control the motion of charged objects in microchannels relies on the presence of ion depletion zones (IDZs) and their corresponding EFGs.[16,20] An IDZ refers to a region of solution that contains fewer ionic species—and therefore has higher electrical resistivity—than the bulk. When a voltage is applied across a channel containing an IDZ, a disproportionate amount of the voltage drops within the IDZ resulting in an EFG in solution. Importantly, charged objects experience enhanced electromigration within the EFG. By tuning the magnitude and location of the EFG, the motion of charged objects can be controlled in useful ways.

Perhaps the simplest example of controlling the motion of charged objects along EFGs is EFG focusing.[13,14,16] In this method, the motion of a charged object is controlled by the interplay of two forces: electromigration and convection. To understand the mechanism of EFG focusing, consider the motion of the negatively charged object located at position A in Illustration 1.1. At this position, the electric field is weak, convection dominates electromigration, and the object moves from right to left. As the object moves to the left, however, it encounters the IDZ and the locally enhanced electric field. Accordingly,

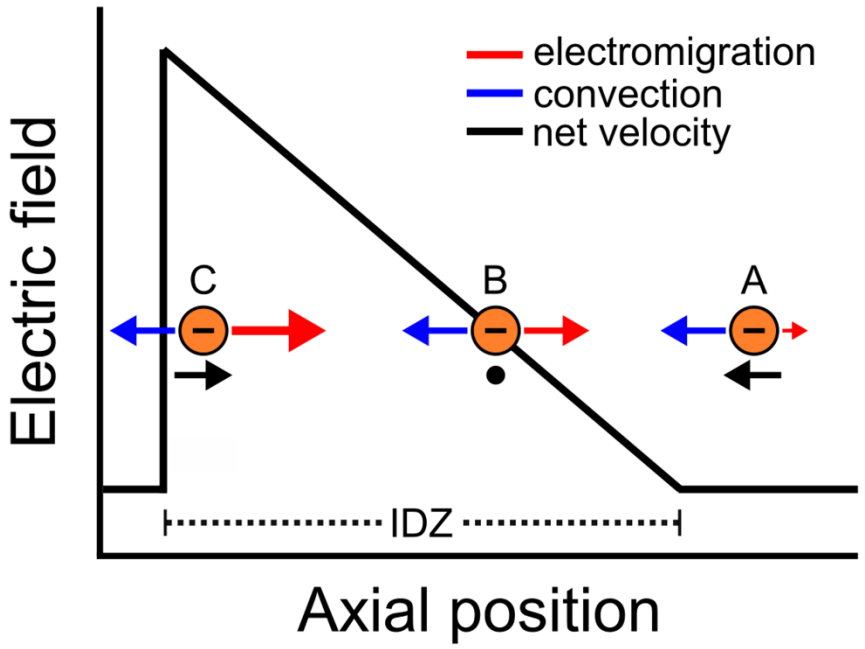

Illustration 1.1

when the object reaches position B, the forces of electromigration and convection acting on the object are exactly balanced, and its net velocity is zero. Nevertheless, if the object were to diffuse to position C, electromigration would operate in a restorative manner to return the object to position B. The net effect is that the charged object is focused at position B.

Since the development of EFG focusing in 1996, the notion that the transport of charged objects in microchannels can be controlled by carefully modulating the forces of electromigration and convection has been successfully applied to a variety of analytical separations. For example, EFGs have been shown to simultaneously separate

and enrich different oxidation states of the protein myoglobin,[13] enrich the local concentration of green fluorescent protein by more than a millionfold,[20] and continuously separate red blood cells from dilute whole blood.[41] The important point, however, is that IDZs and their corresponding EFGs separate chemical species on the basis of electrophoretic mobility. This is fundamentally different than separations by thermal distillation and membrane-based techniques. Accordingly, an improved understanding of EFG-based separations may pave the way for the development of more energy-efficient strategies for chemical separations.

1.2.2 Ion concentration polarization

Some of the earliest reports of EFGs controlling the motion of charged species in solution relied on IDZs formed by ion concentration polarization (ICP).[17-20,25,42] ICP usually refers to the redistribution of ions near nanopores or permselective membranes due to selective transport phenomena. Illustration 1.2 is a schematic of a common system configuration for ICP experiments. It shows two microfluidic channels connected by a membrane having a negative surface charge. If a voltage of the indicated polarity is applied across the microfluidic system, the membrane selectively transports cations from the top channel

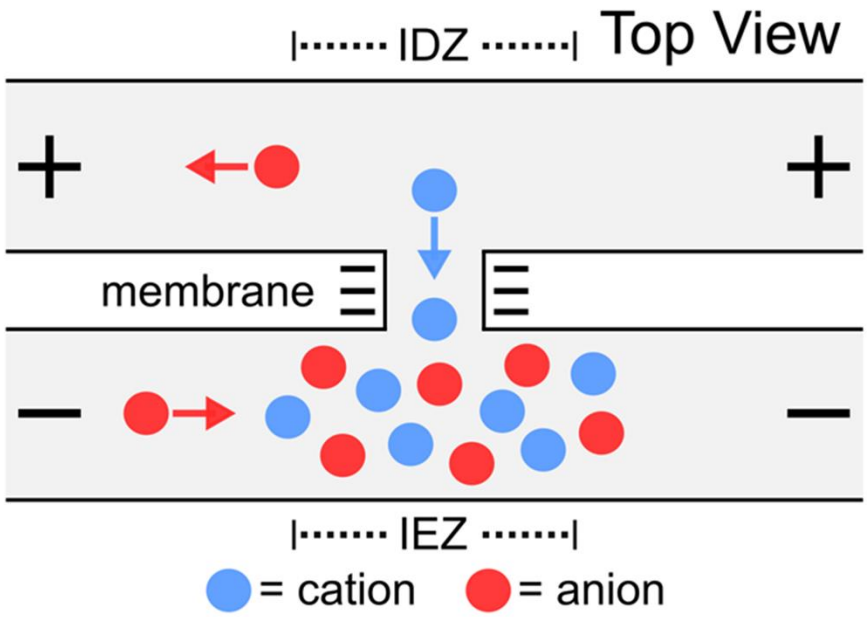

Illustration 1.2

to the bottom channel but rejects the passage of anions. To maintain electroneutrality throughout the microfluidic system, anions migrate as shown in Illustration 1.2. Importantly, selective transport produces an IDZ in solution near the intersection of the top channel and the membrane. A corresponding region of elevated ionic concentration, termed the ion enrichment zone (IEZ), forms in solution near the intersection of the bottom channel and the membrane. The main point is that the IDZ formed by ICP produces an EFG that can control the motion of charged objects in solution.

The study of IDZs formed by ICP has improved understanding of the processes fundamental to EFG-based separations. One reason for this is that membranes are

essentially large arrays of individual nanopores. Accordingly, ICP at one or a few microchannel-nanopore interfaces provides a simple experimental system to begin to understand how selective transport and the presence of an IDZ impact the motion of charged species in solution.[19,20,43,44] *Furthermore, ICP in these simple experimental domains can be accurately described by numerical models, which, in turn, inform future research directions.*[45,46] *In this way, experimental and computational methods have been used to thoroughly characterize the propagation of IDZs,*[23,24,47] *predict the location of focusing and stacking for charged analytes,*[44,48,49] *and describe the formation of recirculating backflows during ICP.*[50,51]

ICP also catalyzed the application of EFGs to many important chemical separations. For instance, ICP has been shown to separate, enrich, and purify nucleic acids from human serum,[52] *control the motion of biomolecules in paper-based analytical devices,*[53] *and desalinate seawater.*[54–58] *More recently, numerical simulations demonstrated that an ICP-based device can continuously extract* Li^+ *from high* Mg^{2+}/Li^+ *ratio brine solutions.*[59] *These findings are important and demonstrate that EFG-based strategies are broadly relevant to the separation of charged analytes.*

Ultimately, however, ICP relies on selective transport at nanopores and membranes to form IDZs and their

corresponding EFGs in solution. In other words, ICP is a membrane-based separation technique and thus suffers from the limitations intrinsic to membranes. For example, the selectivity of the membranes commonly used for ICP is non-ideal and decreases as the ionic strength of solution increases.[60–63] This limits the separation performance of ICP in electrolytes having concentrations >~100 mM.[33] Moreover, nanopores and membranes are difficult to integrate into microfluidic systems and are prone to failure by fouling and clogging.[29,31,64,65] For these reasons, our group was motivated to develop a membrane-free method to form IDZs and their corresponding EFGs in microfluidic systems.

1.2.3 Faradaic ion concentration polarization

In 2008, our group reported a membrane-free electrochemical variant to ICP.[34,35] This approach relied on faradaic processes proceeding at bipolar electrodes (BPEs) to form IDZs in microchannels and is referred to as faradaic ion concentration polarization (fICP). Illustration 1.3a is a schematic of the microfluidic system utilized for fICP experiments. It shows a BPE patterned along the floor of a microfluidic channel. A BPE is usually an electronically isolated piece of metal in contact with an electrolyte solution.[66–69] When a sufficiently large driving voltage

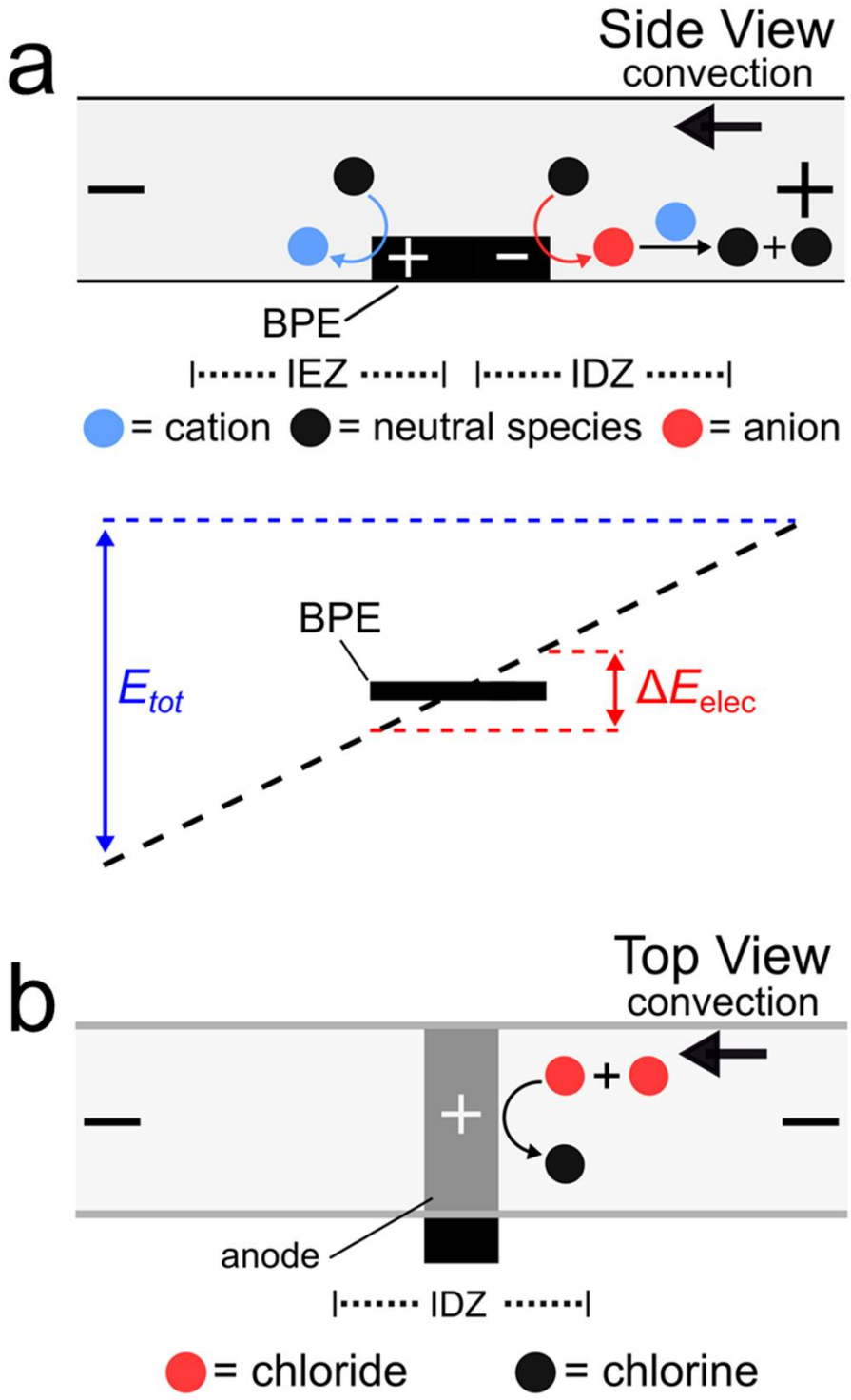

Illustration 1.3

(E_{tot}) is applied across a microchannel containing a conductive piece of metal, the metal develops anodic and cathodic poles where faradaic reactions proceed. The driving force for these reactions is the potential difference between the solution and the two ends of the BPE (ΔE_{elec}). ΔE_{elec} is generally related to E_{tot}, the length of the microchannel ($l_{channel}$), and the length of the BPE (l_{elec}), as described by eq 1.1.

$$\Delta E_{elec} = \frac{E_{tot}}{l_{channel}} l_{elec} \qquad (1.1)$$

For the case of fICP depicted in Illustration 1.3a, water electrolysis proceeds at the poles of the BPE when E_{tot} is sufficiently large. Water reduction at the cathodic pole produces OH^- (eq 1.2). If the microchannel contains Tris buffer solution, OH^- (red circle) neutralizes the cationic buffer species ($TrisH^+$, blue circle) forming an IDZ in the vicinity of the cathodic pole of the BPE (eq 1.3). To conserve charge, water oxidation proceeds at the anodic pole (eq 1.4). In this way, fICP forms an IDZ and an IEZ in solution near the cathodic and anodic poles of the BPE, respectively, and is analogous to ICP.[38]

$$\text{Cathode:} \quad 2\ H_2O + 2\ e^- \leftrightarrow 2\ OH^- + H_2 \qquad (1.2)$$

$$TrisH^+ + OH^- \leftrightarrow Tris + H_2O \qquad (1.3)$$

$$\text{Anode:} \quad 2\ H_2O \leftrightarrow 4\ H^+ + O_2 + 4\ e^- \qquad (1.4)$$

Compared to ICP, there are a few advantages to fICP. First, fICP proceeds at mechanically robust BPEs fabricated

by standard photolithography procedures. Second, IDZs and IEZs form under potential control. This means that by simply varying the magnitude of ΔE_{elec} *(most commonly by changing* E_{tot} *or* i_{elec}*), the IDZ and its associated EFG can be tuned for the specific chemical separation of interest or even prevented altogether.*[36,39] *Third, BPEs are wireless electrodes (i.e., no direct electrical contact). This is significant for two reasons: (1) BPEs can be easily integrated into the small features of microfluidic systems and (2) a single power supply can be used to control the potential difference across one BPE or 1000 BPEs.*[66] *For these reasons, we think that fICP at BPEs is a viable approach to scale up microfluidic-based separations to the macroscale.*

Our group first utilized fICP to enrich a fluorescent tracer at a static location within a straight microfluidic channel.[34] *Subsequent computational and experimental studies thoroughly characterized fICP phenomena in a straight channel and demonstrated that up to three fluorescent tracers could be simultaneously separated and enriched at distinct locations along the channel length.*[35,37] *Finally, our group reported that fICP in a forked microchannel gated the delivery of two fluorescent tracers resulting in a batch-type separation.*[70]

However, the long-term goal of this research is to continuously direct the flow of charged objects using EFGs formed in solutions of more environmental relevance than Tris buffer solutions. To this end, our group developed a new approach to fICP that relied on electrochemically oxidizing Cl^- to neutral Cl_2 (eq 1.5) to form an IDZ in Cl^--containing solutions like seawater.[71] *This approach is shown in Illustration 1.3b.*

$$2\ Cl^- \leftrightarrow Cl_2 + 2\ e^- \qquad (1.5)$$

Preliminary experimental and computational results led to the conclusion that electrochemical Cl^- oxidation forms an IDZ in solution and the associated EFG partially desalinates seawater.[72,73] *Since then, however, we have been unable to repeat these promising results. Therefore, the aims of the research described in this dissertation are: (1) to develop a thorough understanding of how EFGs formed by fICP can be utilized to continuously manipulate the flow of charged objects in forked microchannels and (2) to investigate the formation of IDZs and EFGs by electrochemical Cl^- oxidation in a microchannel. To this end, we employed a combination of experimental and computational methods.*

Many of the experiments reported in this dissertation were performed using solutions containing small, charged plastic particles. These particles are optically visible

and served as proxies for ions and charged molecules present in solution. However, we quickly realized that controlling the motion of plastic particles in solution was a significant finding in itself.

1.2.4 Microplastics

The discovery and development of synthetic plastics at the start of the 20th century and the subsequent wide-spread adoption of these inexpensive, moldable, versatile, and chemically and mechanically robust materials represent important technological and societal advancements.[74-76] *However, the long-term stability, large production volumes, and designed disposability of many plastic products pose significant challenges to the responsible management of plastic waste.*[77-79] *This is increasingly apparent with the growing quantity of plastic litter and debris present in both urban and rural settings and in the natural environment.*[80-84] *Macroscale plastic waste is visible to the eye, aesthetically displeasing, and detrimental to animal life.*[85-87] *For these reasons, large plastic waste prompted the revitalization of recycling practices in the 1970s.*[88] *Small plastics, on the other hand, are more difficult to perceive and thereby went largely unnoticed until more recently.*[89] *Nonetheless, a growing number of scientific studies conclude that small plastic particles, commonly*

referred to as microplastics, are ubiquitous in the environment, including in natural waters and, consequently, drinking water. In light of these findings, current research seeks to understand the fate and transport of microplastics throughout the environment and quantify the exposure and hazard of microplastics to humans and animals.[90,91]

Microplastics generally refer to particles composed of synthetic plastics having a length less than 5 mm. While plastic particles smaller than 0.1 or 1.0 µm are sometimes classified as nanoplastics, we will refer to all particles having a length of up to 5 mm as microplastics in this dissertation. Microplastics may be further categorized into two types: primary and secondary. Primary microplastics are intentionally manufactured to fall within the microplastic size range (e.g., microbeads in beauty products or plastic powders), while secondary microplastics form by the degradation and fragmentation of large plastic objects during normal wear and tear or by weathering processes following disposal. While primary and secondary microplastics are similar to macroscale plastics in composition and non-size-related physicochemical properties, there are unique hazards associated with the size of microplastics.

Microplastics have been detected in the food we eat, the water we drink, and the air we breathe.[92] *Based on their small size and pervasiveness, microplastics may be easily ingested or inhaled.*[93-96] *Upon entering the body, there are two principal hazards associated with microplastics. The first type of hazard is physical in nature. Specifically, small plastic particulates can abrade the surfaces of the respiratory and gastrointestinal systems and lead to inflammation, irritation, lesions, or even cancers.*[97-99] *In addition, animal studies have shown that small microplastics may absorb into the surrounding tissue or enter the circulatory system.*[100,101] *The accumulation of microplastics within tissue and the transport of microplastics throughout the body can further disrupt physiological functions.*[102,103]

The second type of hazard associated with microplastics is chemical or biological in nature. Microplastics can transport myriad harmful substances and microorganisms.[104-107] *For example, plastics often contain additives, dyes, and other toxic chemicals associated with polymerization processes.*[108,109] *Furthermore, the hydrophobic nature of microplastics can lead to the sorption of hydrophobic substances to the plastics, such as persistent organic pollutants (e.g., polychlorinated biphenyls, polycyclic aromatic hydrocarbons, organochlorine pesticides, etc.).*[110-

[112] *Finally, the colonization of microplastics by microorganisms in natural waters leads to the formation of biofilms on microplastic surfaces.*[113,114] *While the majority of microorganisms comprising biofilms are benign, some are pathogenic and lead to infectious disease.*[115] *Accordingly, microplastics act as vehicles for toxic chemical substances and pathogenic bacteria to enter the body. Once inside, leaching processes unload the harmful cargo from the microplastics and enable their spread throughout the respiratory, gastrointestinal, and circulatory systems.*[116]

While there are significant hazards associated with microplastics, the health risk of consuming microplastics is also inextricably linked to the level of exposure. Therefore, the goal of many recent and ongoing studies is to quantify the concentration of microplastics present in the environment. Despite a growing literature regarding microplastic concentrations in air, soil, marine environments, freshwater, and drinking water, a lack of standardized methods for sampling and analysis limits the reliability of the reported data.[117] *For example, a recent critical review commissioned by the World Health Organization assessed the quality of 50 studies that investigated the concentration of microplastics in freshwater and drinking water.*[118] *The main finding from the review is that the data from only four of the 50 studies*

were considered to be sufficiently reliable following assessment with an 18-point rubric. The critical review concludes that the development of standardized methodologies and quality control improvements with respect to sample treatment, polymer identification, processing conditions, and control studies are necessary to quantify the concentration of microplastics in the environment.

One other challenge to quantifying microplastic exposure levels is related to sampling.[90,91,118] *Most researchers rely on sieving or filtering processes to separate microplastics from water or high-density salt solutions.*[119–122] *Accordingly, the size class of microplastics collected depends on the pore size of the mesh or net passed through the solution. While these approaches are relatively straightforward and successfully capture many large microplastics, most of the meshes used are ineffective at capturing small microplastics (<10 μm). This is a significant problem because, while large microplastics may account for the majority of the volume of microplastics in an environmental medium, small microplastics are likely to account for the majority of the number of microplastics.*[90,91] *In addition to leading to the report of erroneous microplastic concentrations, the selective sampling of large microplastics limits understanding of the unique properties and toxicity of small microplastics.*[123–125] *For these*

reasons, the development of new approaches to separate small microplastics from solution is critical to the accurate quantification of microplastic exposure levels.[126]

Charged-based processes for separating microplastics from solutions are promising alternatives to size-based sieving and filtering processes.[127] *While predicting the surface charge of microplastics in water is complex and depends on factors such as the initial surface chemistry of the plastic and the chemistry of the water, a few general (but informative) trends are apparent from the literature. These trends are dictated by the fact that nearly every microplastic particle present in natural waters interacts with natural organic matter and also develops a surface-associated biofilm.*[113,128,129] *For positively charged microplastics, these processes tend to neutralize the positive surface charge or lead to charge inversion.*[130,131] *For neutral microplastics, these processes can induce a negative surface charge and decrease the likelihood that the microplastics aggregate and settle out of solution. For negatively charged microplastics, these processes tend to stabilize the initial negative surface charge.*[132] *In summary, natural organic matter interactions and biofilm formation result in the majority of suspended microplastic pollution having a negative surface charge in natural waters.*[133] *Importantly, the motion of charged microplastics*

can be controlled by the presence of an EFG in solution.[16,17,20,41,134]

In this dissertation, we demonstrate that IDZs and EFGs formed by fICP in microelectrochemical devices control the motion of charged microplastics. While the following studies employed commercially available microplastics present in solutions prepared from reagent-grade salts, we believe that fICP is also relevant to the separation of microplastic pollution from natural waters and provides at least two benefits relative to current sieving and filtering methods. First, it separates microplastics on the basis of surface charge rather than size. Accordingly, microplastics of various size classes—from less than a nanometer to more than a micron in diameter—can be effectively separated from solution using a single strategy. Second, the electrochemical process proceeds within a microelectrochemical device designed for conjunctive use with optical and fluorescence microscopy techniques. This enables the simultaneous separation and quantification of microplastics present in a sample.

Chapter Two: Experimental

2.1 Chemicals

Polystyrene microbeads surface functionalized with carboxyl groups (diameter = 0.99 µm, 1.04 µm, and 0.20 µm) were obtained from Bangs Laboratories, Inc. (FC04N, PC04N, and PC02N; Fishers, IN). BODIPY disulfonate fluorophore ($BODIPY^{2-}$) was obtained from Molecular Probes (Eugene, OR). Pluronic F108 was purchased from BASF (Florham Park, NJ). Tris(hydroxymethyl)aminomethane buffer solutions (Tris-HCl, pH 8.1; Tris-H_2SO_4, pH 8.0) were prepared by dissolving reagent-grade Trizma base (Sigma-Aldrich, St. Louis, MO) in deionized water (DI water, 18.0 MΩ cm, Milli-Q Gradient System, MilliporeSigma, Burlington, MA) and then adjusting solution pH by dropwise addition of HCl or H_2SO_4 (Fisher Scientific, Hampton, NH). NaCl and Na_2SO_4 solutions were prepared by dissolving the corresponding reagent-grade salt (Fisher Scientific) in DI water.

Microfluidic channels were fabricated with poly(dimethylsiloxane) (PDMS) prepared from a silicone elastomer kit (Sylgard 184, Dow, Midland, MI). SU-8 2025 photoresist, AZ 1518 photoresist, and AZ 400K developer were purchased from MicroChemicals GmbH (Germany). Adhesion promoter (Micro Prime HP Primer) was purchased from Shin-Etsu MicroSi (Phoenix, AZ). Ti and Pt deposition metals

were purchased from Kurt J. Lesker Company (Jefferson Hills, PA). Si wafers were obtained from UniversityWafer, Inc. (Boston, MA) and glass slides were obtained from Fisher Scientific.

2.2 MICROCHANNEL FABRICATION

Microfluidic channels fabricated in PDMS were prepared using standard soft lithography procedures. Briefly, a Si wafer (~1 in length, ~1 in width) was submerged in piranha solution (3:1 mixture of H_2SO_4 and 30% H_2O_2) for 15 min. Following piranha treatment, the wafer was thoroughly rinsed with DI water, dried under high-purity N_2, and then dehydrated on a hotplate at 180 °C for 5 min. Next, a spin coater (WS-650Mz-23NPPB, Laurell Technologies Corporation, North Wales, PA) programmed with a three-step procedure (500 rpm, 5 s; 4500 rpm, 60 s; 500 rpm, 10 s) was used to coat the top surface of the wafer with a ~20 µm thick layer of SU-8 2025 photoresist. Following spin coating, the wafer was heated on a hotplate for 2 min at 65 °C and then an additional 5 min at 95 °C.

Next, a mask aligner (MA6, Suss MicroTec, Germany) was used to orient a negative photomask (designed using CorelDRAW 12 software (Corel Corporation, Canada) and fabricated by CAD/Art Service, Inc. (Bandon, OR)) atop the wafer and expose the photoresist to UV light. After

exposure, the wafer was heated on a hotplate for 1 min at 65 °C and then an additional 5 min at 95 °C. Next, the photoresist was developed by submerging the wafer in propylene glycol methyl ether acetate solution for 1-2 min. After development, the wafer was rinsed with isopropyl alcohol, rinsed with DI water, and dried under high-purity N_2. The wafer was then placed in a petri dish and PDMS (10-parts base elastomer, 1-part curing agent) was poured over the wafer. The PDMS was cured in an oven at 65 °C for at least 12 h and then carefully separated from the Si wafer.

2.3 ELECTROCHEMICAL CIRCUITRY FABRICATION

Electrochemical circuitry was fabricated using standard lift-off photo-patterning procedures. Briefly, a glass slide (3 in length, 1 in width) was submerged in piranha solution (3:1 mixture of H_2SO_4 and 30% H_2O_2) for 15 min. Following piranha treatment, the slide was thoroughly rinsed with DI water, dried under high-purity N_2, and then dehydrated on a hotplate at 180 °C for 5 min. Next, a spin coater (WS-650Mz-23NPPB) programmed with a three-step procedure (500 rpm, 5 s; 3500 rpm, 45 s; 500 rpm, 10 s) was used to coat the top side of the glass slide with a layer of Micro Prime HP Primer. The slide was then heated on a hot plate at 150 °C for 1 min. Next, the spin coater programmed with the same three-step procedure was used to coat the

primer layer with AZ 1518 photoresist. Following spin coating, the glass slide was heated on a hot plate at 100 °C for 45 s.

Next, a mask aligner (MA6) was used to orient a negative photomask (designed using CorelDRAW 12 software and fabricated by CAD/Art Service, Inc.) atop the glass slide and expose the photoresist to UV light. After exposure, the slide was heated on a hotplate for 1 min at 100 °C and then an additional 1 min at 120 °C. Next, the photoresist was developed by submerging the glass slide in AZ 400K developer solution for 45 s. After development, the slide was rinsed with DI water and dried under high-purity N_2.

The glass slide patterned with photoresist was then placed in an electron beam physical vapor deposition system designed by Cooke Vacuum Products (Norwalk, CT) and the vacuum chamber was pumped down to at least 10^{-6} torr. First, a 10 nm adhesion layer of Ti was deposited on the glass. Then, a 100 nm layer of Pt was deposited atop the Ti adhesion layer. Following deposition, liftoff was performed by sonicating the slide in acetone and then wiping the surface clean with a Kim Wipe (Fisher Scientific).

2.4 MICROELECTROCHEMICAL DEVICE FABRICATION

Hybrid glass/PDMS microelectrochemical devices were fabricated using a previously reported procedure.[135] First,

3 mm reservoirs were punched at the ends of a PDMS microfluidic channel. Second, the microchannel and a Pt microwire-patterned glass slide were rinsed with ethanol and dried under high-purity N_2. Third, the glass and PDMS were exposed to an O_2 plasma for 45 s (medium power, 60 W, PDC-32G, Harrick Scientific Products Inc., Ossining, NY) and then joined together. Fourth, the assembled device was heated in an oven at 65 °C for 5 min to ensure irreversible bonding. Fifth, Cu wires were attached to the patterned Pt circuity using Ag conductive paint (Electron Microscopy Sciences, Hatfield, PA) and Devcon five-minute epoxy (Fisher Scientific).

2.5 Optical and fluorescence microscopy

The motion of polystyrene microbeads and $BODIPY^{2-}$ fluorophore during experiments was visualized using an inverted fluorescence microscope (Eclipse TE 2000-U, Nikon, Japan) equipped with a CCD camera (Cascade 512, Photometrics, Tucson, AZ) controlled by V++ software (DigitalOptics Corporation, San Jose, CA). Image analysis was performed in ImageJ (National Institutes of Health, Bethesda, MD). Fluorescence measurements were performed with the fluorescence lamp (X-Cite 120Q, Excelitas Technologies Corp., Waltham, MA) on, while optical studies were performed with the lamp off.

2.6 Flow rate measurements

The rate of pressure-driven flow (PDF) was determined by optically tracking the motion of polystyrene microbeads along the channel length in the absence of an applied voltage using an inverted microscope (Eclipse 2000-U).

2.7 Solution conductivity measurements

Solution conductivity measurements were obtained using a previously reported, home-built conductivity instrument.[136,137] Measurements were performed as follows. A function generator (Model 182A, Wavetek, San Diego, CA) was used to apply an ac sine wave to one Pt microband. The resulting current passed through solution to a detection microband patterned 30 μm (center-to-center) downstream, where it was amplified and converted back to a voltage by a transimpedance amplifier. The attenuation of the current passing through solution to the detection microband was related to solution conductivity using a calibration curve. Conductivity measurements were carried out at 20 ± 2 °C.

Chapter Three: Continuous Redirection and Separation of Microbeads via Faradaic Ion Concentration Polarization[1]

3.1 Synopsis

In this chapter, we report that faradaic ion concentration polarization can be used to sort and separate micron-scale objects within a bifurcated microelectrochemical device. In faradaic ion concentration polarization, a bipolar electrode is activated by a driving voltage, which results in formation of an ion depletion zone and an ion enrichment zone. By judicious control of the placement of the bipolar electrode and control of the driving voltage, the ion depletion zone and ion enrichment zone can be manipulated in a way that directs charged microbeads into a particular channel of the microelectrochemical device. The key findings are threefold. First, nearly 100% microbead redirection and separation may be achieved by faradaic ion concentration polarization. Second, the tracking of microbeads as they traverse the channel length permits visualization of local variations in electroosmotic flow. Third, variations in solution conductivity in different regions of the channel lead to differences in electroosmotic

[1] *The work described here was previously published: Davies, C. D.; Yoon, E.; Crooks, R. M. Continuous redirection and separation of microbeads via faradaic ion concentration polarization. ChemElectroChem* **2018**, *5*, 877-884. *CDD, EY, and RMC planned the experiments; CDD performed the experiments; CDD and EY analyzed the results; CDD wrote the article; CDD, EY, and RMC edited the article; and RMC supervised the research.*

flow that exert a significant influence over microbead trajectory.

3.2 Introduction

Ion concentration polarization (ICP) refers to a local redistribution of charge in an ionic solution. This redistribution results in a region of the solution depleted in charge (the ion depletion zone, IDZ) and another region that is enriched (the ion enrichment zone, IEZ).[17,25] *Illustration 3.1a illustrates one common method for creating an IDZ and an IEZ.*[17,18,25,26,134,138] *Here, two microchannels are connected by a permselective membrane*[18,134,138,139] *or nanochannel*[20,46,49,54,140,141] *that transmits only cations. When a voltage of the indicated polarity is applied at the ends of the two channels, cations in the top channel pass through the membrane, and to maintain charge neutrality, counter ions move toward the positive driving electrode. This local loss of ions near the intersection of the top channel and the membrane is the IDZ, and the region at the other end of the membrane is the IEZ.*

The loss of ions in the IDZ leads to a local increase in solution resistance and a corresponding electric field gradient (EFG) of the type shown in Illustration 3.1b. If, in addition to electromigration, ions are subject to a convective force, they can be enriched,[20,142] *depleted,*[143] *or*

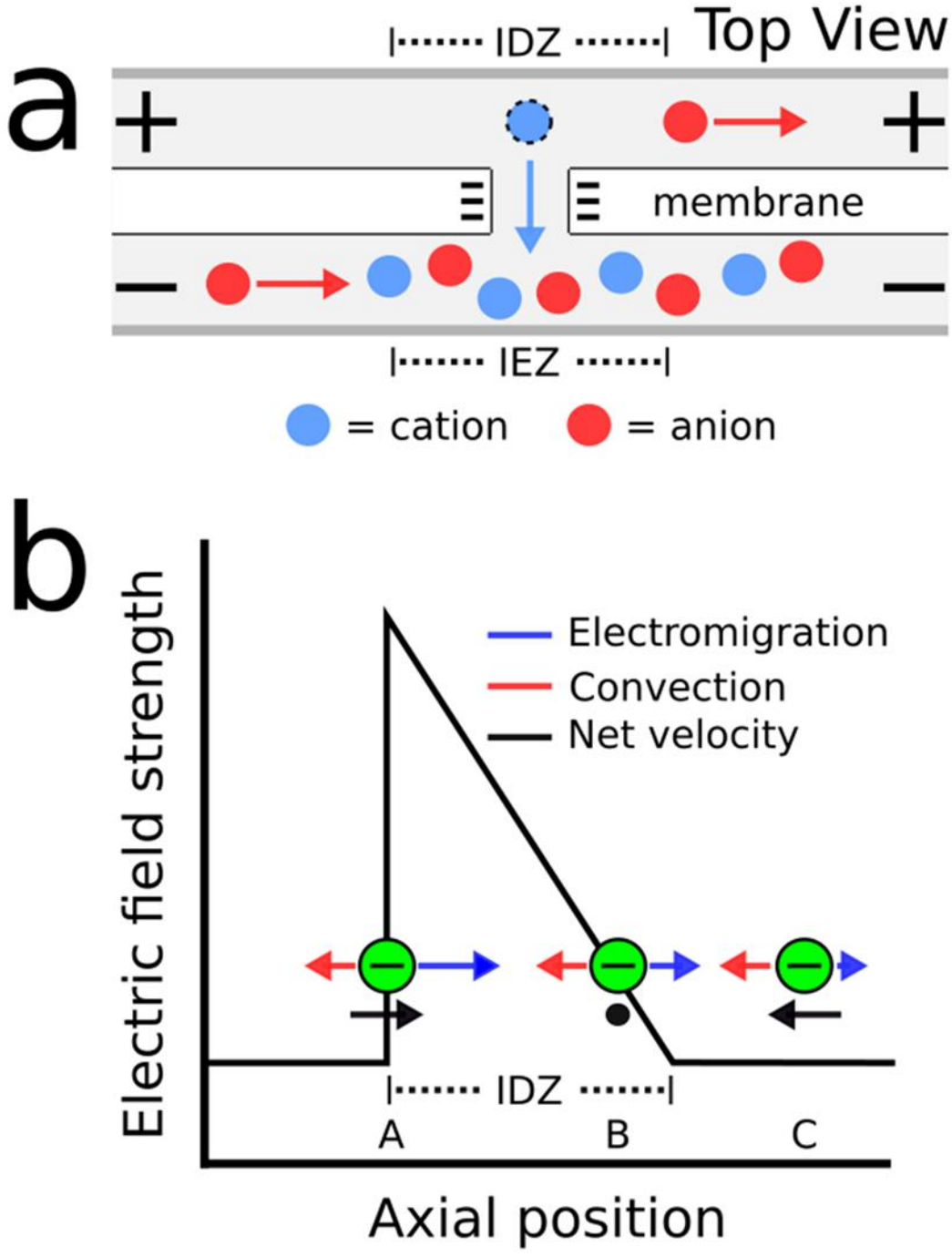

Illustration 3.1

separated[37,69] *via a mechanism known as EFG focusing.*[16,35,39] *For example, Illustration 3.1b shows how ions interact with opposing electromigration and convection in the vicinity of the IDZ. Consider a negatively charged ion at axial position A. At this location the local electric field is at its maximum, electromigration dominates convection, and the ion moves from left to right. When the ion reaches position B, the field strength is lower than at A, and therefore at this unique location the forces of electromigration and convection exactly balance, and there is no net external force acting on the ion. If the ion should move to position C (where the field strength is low) through normal diffusion, however, then convection dominates and the ion is returned to position B. Likewise, if the ion diffuses to the left of position B, it experiences a restoring force to the right and returns to its original location at position B. The net impact of the IDZ, therefore, is that all ions in the channel are eventually concentrated at position B. Accordingly, ICP provides a means for concentrating proteins, enzymes, ions, and charged particles.*[20,34,54,134]

While ICP most commonly relies on selective transport of cations or anions through a nanochannel or permselective membrane to develop the IDZ, there are some problems with this approach. First, membranes and nanochannels are difficult to fabricate in formats that are compatible with

microfluidic devices. Second, membranes and nanochannels are prone to clog, and, third, their selectivity is normally limited to either all cations or all anions. These factors led us to introduce a method we call faradaic ICP (fICP).[17,34-39,70,71,73,142-144]

The technique of fICP is an electrochemical variant of ICP that relies on faradaic processes to produce the IDZ.[38] *Illustration 3.2a shows a common experimental arrangement for implementing fICP. Here, application of a voltage between the driving electrodes located in reservoirs at the end of the channel ($Æ_{tot}$) results in a uniform electric field along the channel length. However, if a bipolar electrode (BPE) is present within the channel,*[66,69,145] *then a potential difference of magnitude $\Delta Æ_{elec}$ will exist between the solution and the two poles of this electrode (Illustration 3.2b). The magnitude of $\Delta Æ_{elec}$ depends primarily on the length of the BPE and the magnitude of $Æ_{tot}$.*[146]

In a typical fICP experiment, $\Delta Æ_{elec}$ is adjusted to a value at which a neutral species like water is reduced to yield OH^- (red circle in Illustration 3.2c) at the BPE cathode. If a buffer cation, such as $TrisH^+$ (blue circle), is present in solution, it will be neutralized by OH^-. The net effect is that two charged species (here, OH^- and $TrisH^+$) are neutralized (eqs 3.1 and 3.2; the corresponding

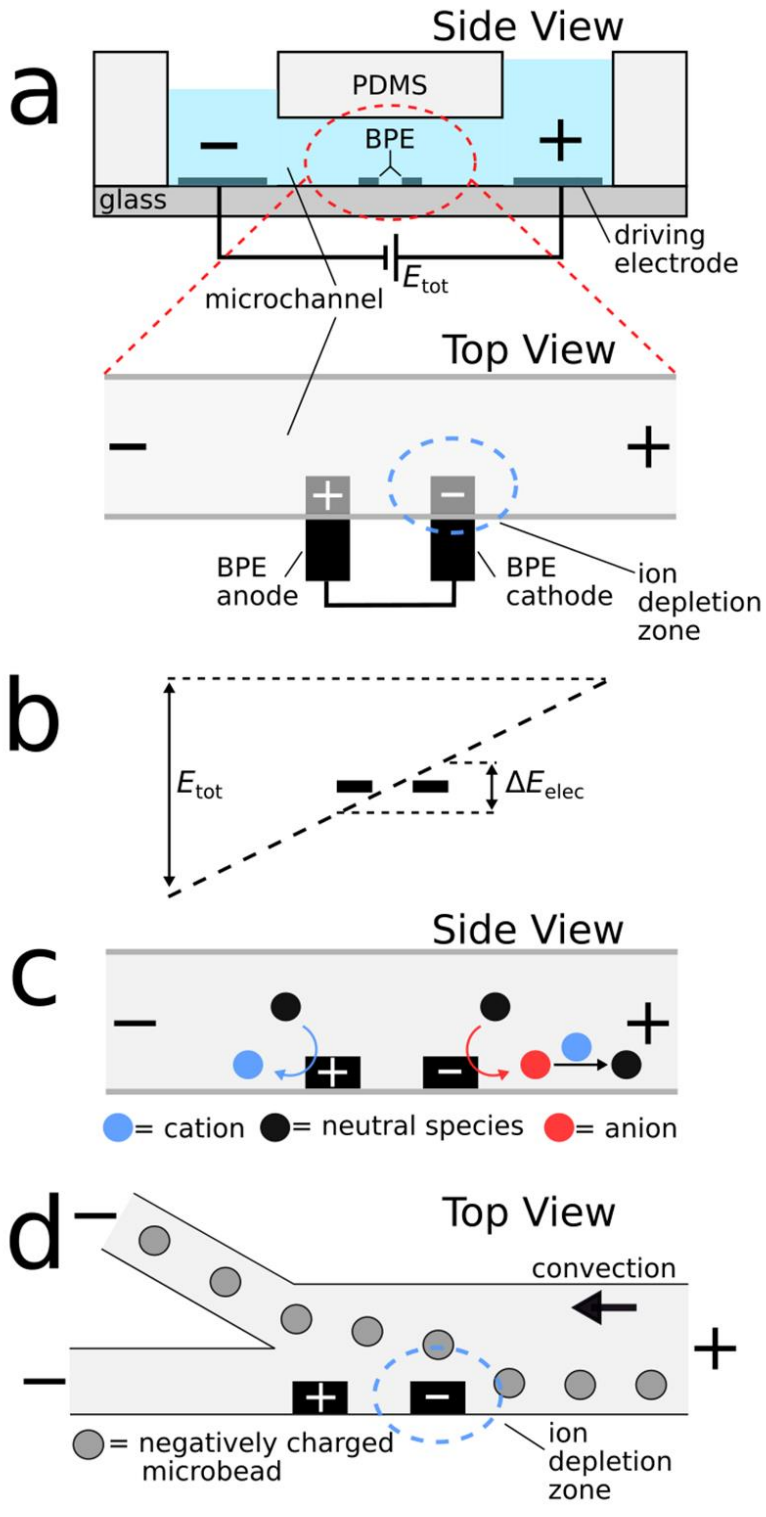

Illustration 3.2

anode reaction is given in eq 3.3), thereby lowering the number of charge carriers in the vicinity of the BPE cathode. This constitutes an IDZ and results in formation of a local EFG like that shown in Illustration 3.1b. If a convective force, like electroosmosis or pressure-driven flow (PDF) is also present in the microchannel, then all of the conditions required for EFG focusing are met.[16] *Note that in fICP there is no membrane, which simplifies fabrication of the microsystem and avoids clogging, and the magnitude of the IDZ can be continuously varied by exerting control over Æ$_{tot}$. We have previously used fICP to concentrate analytes by 500,000 fold,*[38] *simultaneously enrich multiple charged analytes in different locations of the microchannel,*[37] *and partially desalinate seawater.*[71,73]

$$\text{Cathode:}\quad 2\,H_2O + 2\,e^- \leftrightarrow 2\,OH^- + H_2 \qquad (3.1)$$

$$TrisH^+ + OH^- \leftrightarrow Tris + H_2O \qquad (3.2)$$

$$\text{Anode:}\quad 2\,H_2O \leftrightarrow 4\,H^+ + O_2 + 4\,e^- \qquad (3.3)$$

In the present study, we utilized buffer neutralization at a BPE to facilitate redirection of the fluorophore BODIPY^{2-} *and charged polystyrene microbeads. The results indicate that nearly 100% of microbeads flowing down the main channel can be redirected into a secondary channel, as shown in Illustration 3.2d. Additionally, we report that local differences in ion concentration, arising from formation of the IDZ and IEZ, result in local variations in*

electroosmotic flow (EOF) along the channel length. The use of microbeads as tracers reveals that both the EFG across the ion depletion zone and local variations in EOF exert significant perturbations to continuous microbead redirection by fICP. These findings are essential for understanding phenomena fundamental to fICP and for enabling applications to separation science.

3.3 EXPERIMENTAL SECTION

3.3.1 Chemicals

Fluorescent (Dragon green; Ex. 480 nm, Em. 520 nm) (fμB) and non-fluorescent (μB) polystyrene microbeads (diameter = 1.04 μm and 0.99 μm, respectively) surface functionalized with carboxyl groups (FC04F and PC04N; Zeta potential = -27.1 ± 0.6 mV)[147] were obtained from Bangs Laboratories (Fishers, IN). Fluorescent BODIPY disulfonate ($BODIPY^{2-}$) was obtained from Molecular Probes (Eugene, OR). Buffer solutions containing 10.0 mM Tris-HCl (pH 8.1) or 10.0 mM Tris-H_2SO_4 (pH 8.0) were prepared using deionized water (DI water, 18.0 MΩ cm, Milli-Q Gradient System, Millipore) and the corresponding reagent-grade Tris salts (Sigma Aldrich, St. Louis, MO). Unless otherwise indicated, the buffer was prepared using Tris-HCl. Poly(dimethylsiloxane) (PDMS), used to fabricate microfluidic channels, was prepared from a

silicone elastomer kit (Sylgard 184, K. R. Anderson, Morgan Hill, CA).

3.3.2 Microfluidic device fabrication

Hybrid glass/PDMS microfluidic devices were fabricated using a previously reported procedure.[148] Briefly, 3 mm reservoirs were punched at each end of a PDMS microfluidic channel (5 mm length, 200 µm width, 18 µm height). Pt microbands (10 nm Ti adhesion layer + 100 nm Pt, Kurt J. Lesker, Jefferson Hills, PA) were fabricated on glass slides using standard lift-off photo-patterning procedures. The glass and PDMS were joined following exposure to an O_2 plasma (60 W, PDC-32G Harrick Plasma, Ithaca, NY) for 45 s, and then the device was placed in an oven at 65 °C for 5 min to ensure irreversible bonding. The microfluidic channel was positioned so that the Pt microbands spanned 20-25% of the main channel width. For this study, both straight and bifurcated channels were utilized. The width of each of the smaller channels in the bifurcated devices was 50% that of the main channel.

3.3.3 Particle redirection experiments

Prior to making measurements, 2.0 µM $BODIPY^{2-}$, 3.0 pM µB or 56 fM fµB contained in 10.0 mM Tris buffer, were flowed through the microfluidic channel using PDF enabled by a difference in solution height in the two reservoirs

(Illustration 3.2a). The rate of PDF was calculated for each solution height difference in the absence of an applied voltage by measuring the velocity of particles as they traveled downstream.[142,144] Particle redirection experiments were performed as follows. First, two patterned microbands were connected external to the channel using a jumper wire to form a BPE of the desired length. Second, a driving voltage was applied across the channel using a power supply (Tektronix PWS 4721, Beaverton, OR) connected to Pt driving electrodes present on the floor of each reservoir. Third, particle motion was recorded by microscopy.

3.3.4 Optical and fluorescence microscopy

Particle redirection and separation were visualized using an inverted fluorescence microscope (Eclipse TE 2000-U, Nikon, Japan) equipped with a CCD camera (Cascade 512, Photometrics, Tucson, AZ). V++ (DigitalOptics Corporation, San Jose, CA) and ImageJ were used for image capture and analysis, respectively. Fluorescence images were obtained with the fluorescence lamp on, while optical studies were performed with the fluorescence lamp off.

3.3.5 Conductivity measurements

A previously reported design of a direct conductivity circuit was used to measure solution conductivities along the channel length.[71,136] In brief, an ac voltage was

applied to one patterned Pt microelectrode. The resulting current passed through solution to a second microelectrode positioned 15 µm upstream, where it was converted back to a voltage. The attenuation of current passing through the solution between the microelectrodes is proportional to the solution conductivity via a calibration curve (Appendix A).

3.4 Results and discussion

3.4.1 Redirection of $BODIPY^{2-}$ in a straight microfluidic channel

The goal of this study is to show that fICP can be used to precisely direct the motion of micron-scale objects. However, we begin by examining the behavior of a simpler tracer, the molecular fluorophore $BODIPY^{2-}$, to obtain a preliminary understanding of the characteristics of the IDZ in a straight channel.

We have previously examined the effect of an IDZ on the behavior of $BODIPY^{2-}$ in microfluidic devices in which a BPE spans the width of the channel.[35,36,39,70,143,144] In that case, the IDZ develops across the entire width of the channel, and therefore, as discussed in the Introduction, the analyte concentrates near the cathodic pole of the BPE. The goal here is different in that we wish to control the flow of $BODIPY^{2-}$ rather than simply concentrate it in a static location. In the present design, therefore, the BPE

inserts only partway into the main channel. Specifically, as shown in Figure 3.1a (and Illustration 3.2a), the BPE (outlined by a dashed white line) extends only 40-50 µm into the 200 µm-wide channel. In this case, the IDZ and EFG extend across only a portion of the channel width.

As mentioned earlier, the experiments discussed in this section were carried out in a hybrid glass/PDMS microelectrochemical device having a single straight channel. Additionally, all solutions were aqueous and were at neutral pH, and therefore the surfaces of both the glass and PDMS are negatively charged. Therefore, when Æ$_{tot}$ is applied, EOF is initiated toward the negative driving electrode (right to left in Figure 3.1a).[148] *For solutions having a uniform ion distribution, EOF velocity is proportional to Æ$_{tot}$.*[149]

Figure 3.1a is a fluorescence micrograph showing how the flow of BODIPY^{2-} is affected by the presence of the BPE. The micrograph was obtained after applying Æ$_{tot}$ and waiting for the flow to achieve steady state. Note that it has previously been shown that O_2 or Cl_2 electrogenerated at the BPE anode can quench BODIPY^{2-} fluorescence.[150] *In this case, however, the anode is placed downstream and will not affect upstream fluorescence. The important point is that the dark region to the left of the BPE cathode results from the*

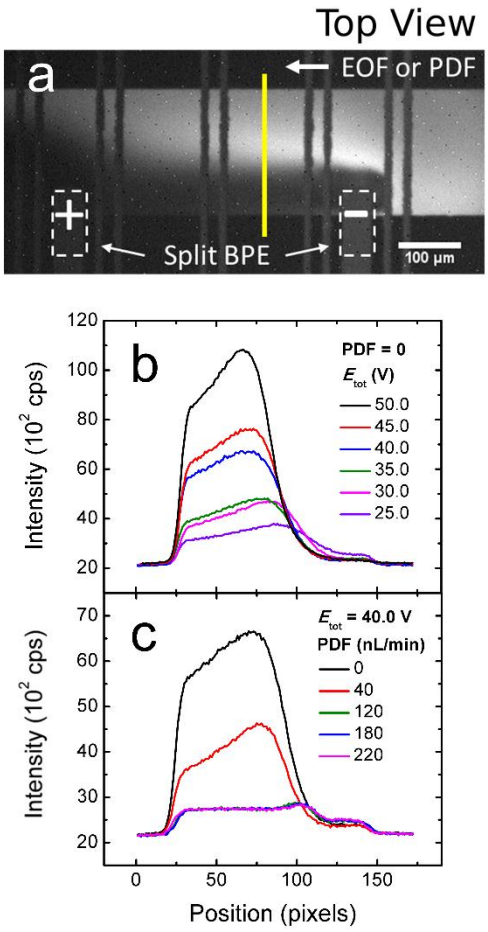

Figure 3.1

Redirection of $BODIPY^{2-}$ in a straight microfluidic channel. (a) A representative fluorescence micrograph obtained using a configuration like that shown in Illustration 3.2a, except in this case there was no PDF. The solution contained 2.0 µM $BODIPY^{2-}$ as a tracer, 3.0 pM µB, and 10.0 mM Tris buffer (pH = 8.1). E_{tot} = 40.0 V. The dashed white lines indicate the locations of the two poles of the BPE (500 µm long). (b) Fluorescence profiles as a function of E_{tot} with PDF = 0. (c) Fluorescence profiles as a function of PDF rate with E_{tot} = 40.0 V. The PDF rate was calculated by tracking the mobility of µB in the absence of an applied voltage. Both sets of profiles were obtained along the yellow line in (a). The top and bottom of the line in (a) represent positions 0 and 175, respectively, in (b) and (c). The vertical microbands spanning the channel width in (a) were not utilized during this study and may be ignored.

presence of an electric field like that illustrated in Illustration 3.1b.

Figure 3.1b is a fluorescence intensity profile, measured along the yellow line in Figure 3.1a, as a function of Æ$_{tot}$. In this case, the solution heights in the two reservoirs were equal, so convection arises from EOF only. The results show that the fluorescence intensity of BODIPY^{2-} increases monotonically as Æ$_{tot}$ increases. This occurs because ΔÆ$_{elec}$, and therefore the local EFG and electromigration velocity, scale with Æ$_{tot}$ (Illustration 3.2b).[69] *Additionally, it is important to note that the formation of an IDZ results in an increase in channel resistance (Figure A.2, Appendix A), which may result in ΔÆ$_{elec}$ deviating from the value calculated using the simplified assumption that it is equal to Æ$_{tot}$ normalized to the channel length.*

The data in Figure 3.1c are similar to those in Figure 3.1b, but in this case Æ$_{tot}$ was maintained constant at 40.0 V, and the rate of convection was varied by introducing PDF. To carry out the experiment, larger volumes of buffer solution were added to the reservoir at the right end of the microchannel (Illustration 3.2a) than the one on the left. The resulting height difference leads to PDF toward the negative driving electrode (right to left in Figure 3.1a). Next, Æ$_{tot}$ = 40.0 V was applied, leading to EOF (also from

right to left) and formation of an IDZ near the cathode and an IEZ near the anode. Finally, fluorescence images were collected under steady-state conditions. The resulting line profiles (Figure 3.1c) show that as the solution velocity increases (varying PDF plus near-constant EOF), the degree of $BODIPY^{2-}$ redirection decreases. In other words, the combined effects of EOF and PDF overwhelm the opposing electromigration force, resulting in minimal redirection of $BODIPY^{2-}$ as it traverses the IDZ. The findings from these studies of $BODIPY^{2-}$ redirection as a function of $Æ_{tot}$ and PDF provide useful guidelines for setting up experiments aimed at manipulating microbeads by fICP.

3.4.2 Redirection of microbeads in a straight channel

Thus far our studies of transport in fICP systems have focused exclusively on fluorescent molecular species.[34,35,37,39,70,142,144] There are some limitations to this approach, however. First, as we have reported previously,[71] fluorescent tracers are subject to bleaching by either O_2 or electrogenerated products (like Cl_2) near the poles of the BPE. Second, unlike microbeads, it is not possible to track individual $BODIPY^{2-}$ ions, which limits observations to bulk phenomena. In contrast, microbead tracers tracked via optical microscopy enable quantification of particle redirection and observation of discrete

particles as they traverse the IDZ. These factors, and an interest in developing a better understanding of the factors governing fICP, have motivated us to examine the motion of individual particles by optical microscopy.

Figure 3.2a is an illustration showing the device configuration used for the microbead experiments. It shows a pair of microband electrodes patterned on the microchannel floor and connected by an external jumper wire to form a 580 µm-long BPE. A third electrode is also shown and there is a fourth electrode to the left of the other three but that is outside the region of the channel shown in the illustration and micrographs. These latter two electrodes make it possible to change the length and location of the split BPE in other experiments that will be described later. The magnitude of ΔE_{elec} *is controlled by* E_{tot} *applied at the channel reservoirs.*

The remaining frames in Figure 3.2 are a series of optical micrographs showing manipulation of negatively charged, 0.99 µm-diameter polystyrene microbeads (µB) during fICP. These experiments were carried out as follows. First, equal heights of a solution containing 3.0 pM µB and 10.0 mM Tris buffer were added to each reservoir of the microelectrochemical device to eliminate PDF and ensure that flow is dominated by EOF. Second, the value of E_{tot} *was*

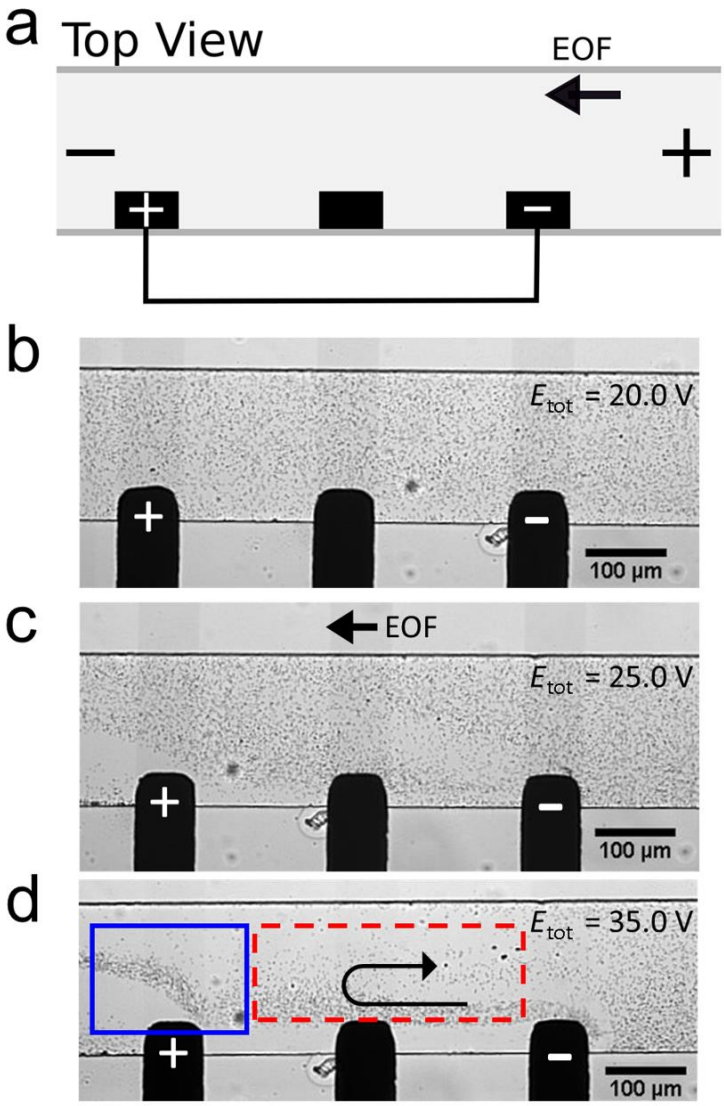

Figure 3.2

Redirection of µB in a straight microfluidic channel. (a) Schematic illustration of the microfluidic system and BPE configuration. The solution contained 3.0 pM µB as tracers and 10.0 mM Tris buffer (pH = 8.1). The length of the BPE was 580 µm and PDF = 0 (convection by EOF only). Optical micrographs showing µB redirection at E_{tot} = (b) 20.0 V, (c) 25.0 V, and (d) 35.0 V. The dashed red box outlines the region where solution vortexing occurs (vortexing can be more easily visualized in Movie A.1, Appendix A). The vortex rotates clockwise, as indicated by the black arrow. The blue box highlights microbead redirection at the BPE anode.

systematically varied and optical microscopy was used to track the motion of microbeads near the BPE.

When E_{tot} = 20.0 V, ΔE_{elec} = ~2.3 V, which is insufficient to drive significant water reduction (eq 3.1), the neutralization reaction (eq 3.2) does not occur, no local electric field forms and the uniform motion of μB is unaffected by the application of E_{tot} (Figure 3.2b). However, Figures 3.2c and 3.2d show that when E_{tot} = 25.0 V (ΔE_{elec} = ~2.9 V) and 35.0 V (ΔE_{elec} = ~4.1 V), respectively, ΔE_{elec} is sufficient to drive eq 3.1, and the resulting IDZ affects the motion of μB.

Optical tracking of individual microbeads as they traverse the channel length reveals significant redirection by the EFG within the IDZ. Two specific points are worth noting. First, the electrochemical process at the BPE anode (eq 3.3) contributes to the redirection of particles (blue box, Figure 3.2d). This finding is surprising because while there is a concentration gradient near the BPE anode due to electrogeneration of H^+,[36] no corresponding EFG has been observed. Second, a single vortex (indicated by the arrow in the red box in Figure 3.2d and in Movie A.1, Appendix A) is observed in the top portion of the channel between the edges of the BPE. The formation of vortexes within an IDZ is a commonly reported phenomenon,[26,48,149,151–153] but there are two differences between this vortex and those previously

reported, both of which are clearly identified in Movie A.1 (Appendix A). Specifically, this vortex is stable for the duration of the experiment (up to 1 min) and the flow rate within the vortex is slower than that of bulk solution flow. In contrast, others have shown vortexes to form sporadically, fluctuate in location throughout the IDZ, and exhibit an increased flow rate compared to that of bulk solution.[152,154] Vortexing will be discussed in more detail later, so suffice it to say here that it probably arises from ionic concentration gradients that develop during fICP. The key point for now, however, is that fICP phenomena, specifically the local electric field in the IDZ and variations in EOF, affect the flow of microbeads.

3.4.3 Continuous redirection and separation of microbeads in a bifurcated channel

Up to this point, we have shown that microbeads can be manipulated in a comprehensible way in a straight channel. We now turn our attention to continuous separation and collection of microbeads in a bifurcated channel. This type of split-channel design (Figure 3.3a) makes it possible to separate microbeads from the main channel and direct them into a specific secondary channel. Although demonstrated here for microbeads, it seems likely that any kind of charged, micron-scale object (e.g., bacteria) could similarly be sorted using this approach.

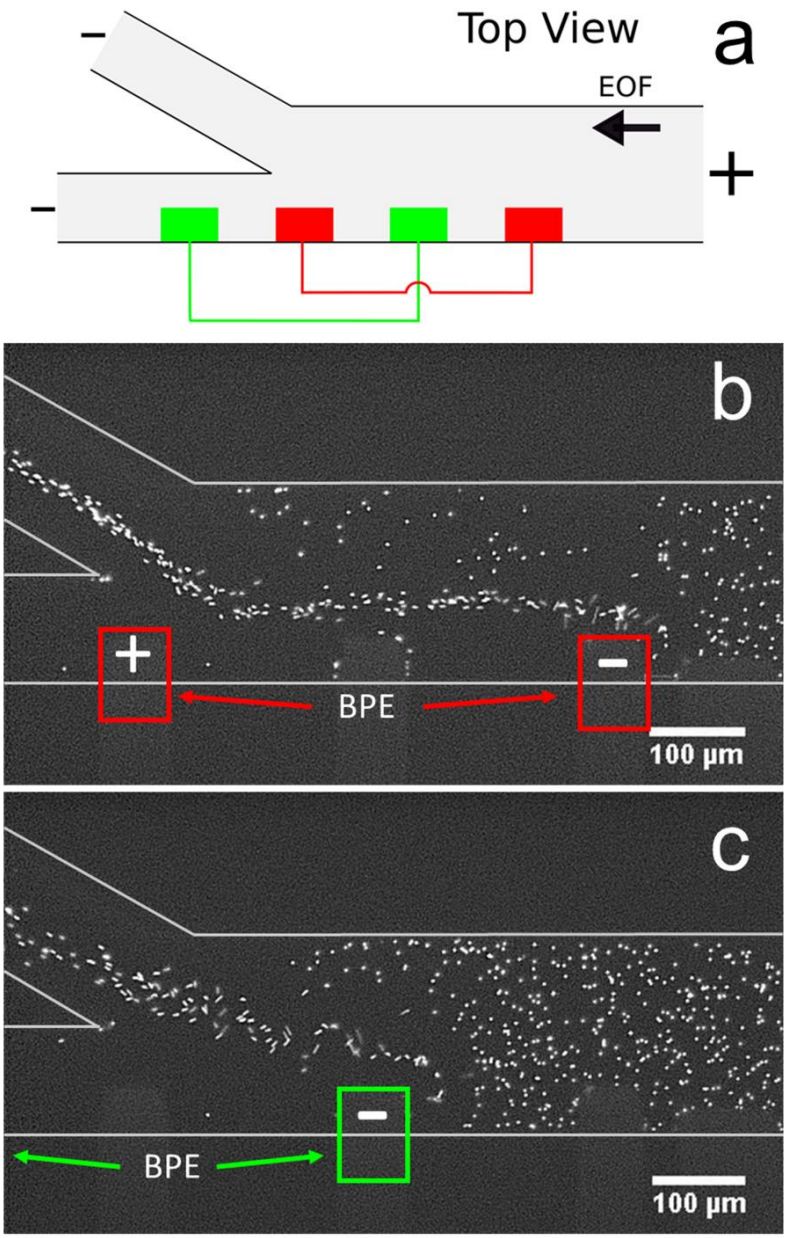

Figure 3.3

Redirection and separation of fμB in a bifurcated microfluidic channel. (a) Schematic illustration of the microfluidic system. (b) A fluorescence micrograph showing fμB redirection and separation obtained using the red BPE configuration in (a). (c) Same as (b), but obtained using the green BPE configuration in (a). The solution contained 56 fM fμB and 10.0 mM Tris buffer (pH = 8.1). E_{tot} = 35.0 V and the BPE length = 580 μm.

The device configuration in Figure 3.3a has two pairs of independently configurable BPEs. Both pairs have the same overall length, but the green configuration places the BPE anode downstream of the channel intersection, thereby eliminating any influence on bead motion by anodic processes of the type discussed in the context of the blue box in Figure 3.2d. In contrast, the red configuration moves the BPE anode into a location where it can affect particle motion prior to redirection into the upper channel.

Figure 3.3b is a fluorescence micrograph showing redirection of fluorescent microbeads. This experiment was set up exactly as described for Figure 3.2, except 56 fM fluorescent microbeads (fμB) were used as tracers. These microbeads had the same size and charge as those shown in Figure 3.2, but their fluorescent properties improve image contrast. The BPE was connected in the red configuration (Figure 3.3a), and then Æ$_{tot}$ = 35.0 V was applied along the channel length resulting in EOF from right to left and formation of the IDZ and IEZ at the BPE cathode and anode edges, respectively. The micrograph was collected under steady-state flow conditions. Figure 3.3c is a fluorescence micrograph collected using the same procedures, but with the BPE connected in the green configuration (Figure 3.3a). Continuous microbead redirection and separation are clearly observed for both the red and green BPE configurations and

is further demonstrated in Movie A.2 (Appendix A). To determine if there is an effect on particle motion by the buffer anion (Cl^-), which can be oxidized to Cl_2 and hence affect the IEZ, we carried out control experiments using a buffer based on Tris-H_2SO_4. However, the results of those experiments (Movie A.3, Appendix A) were the same as those shown in Figure 3.3 suggesting that H^+ generation dominates the anode process.

To better understand microbead redirection by the EFG and flow anomalies stemming from concentration gradients formed during fICP, direct in-situ conductivity measurements were performed. Figure 3.4a is a plot of conductivity signal as a function of time within the top microfluidic channel. This measurement was carried out as described for Figure 3.3, except a pair of microband electrodes, patterned 500 µm downstream of the channel split, was used to measure conductivity in the top channel. In this case, the green BPE configuration was used (Figure 3.3a) and $Æ_{tot}$ = 35.0 V was applied resulting in EOF toward the negative driving electrode. This resulted in redirection of the microbeads, just as in Figure 3.3. Figure 3.4b shows conductivity results obtained by repeating this experiment but measuring conductivity in the bottom channel.

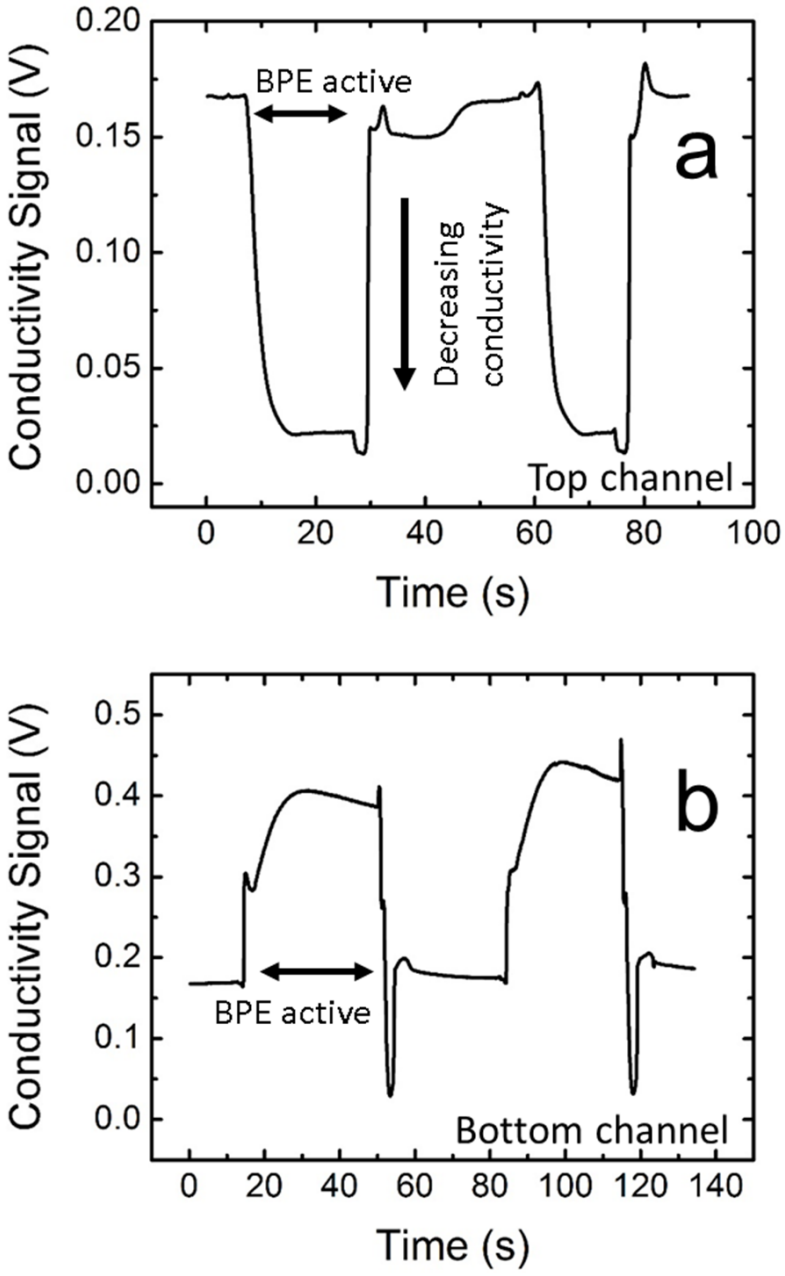

Figure 3.4

Direct solution conductivity measurements measured 500 µm downstream of the channel bifurcation (Figure 3.3a). The solution contained 3.0 pM µB and 10.0 mM Tris buffer (pH = 8.1). Convection was controlled by EOF, E_{tot} = 35.0 V, and the length of the BPE was 580 µm. (a) Conductivity in the top channel. (b) Conductivity in the bottom channel.

The conductivity measurements shown in Figure 3.4 reveal that following the start of fICP (BPE active), a significant reduction in solution conductivity is measured in the top channel (Figure 3.4a), while an increase in solution conductivity is measured in the bottom channel (Figure 3.4b). We believe the decrease in solution conductivity in the top channel corresponds to flow displacement of the IDZ downstream of the BPE cathode. It has previously been reported that Tris buffer neutralization results in a decrease of ~90% in the solution conductivity within the IDZ (compared to the bulk value),[142,143] which matches well with the conductivity decrease shown in Figure 3.4a. Neutralized Tris also flows into the bottom channel downstream of the IDZ, but there is a net increase in conductivity in the bottom channel downstream of the BPE anode resulting from water oxidation (electrogeneration of H^+, eq 3.3) at the BPE anode.

It is well known that local variations in solution conductivity, of the type described in the previous paragraph, result in alteration of the zeta potential of PDMS and glass channel surfaces. These, in turn, lead to local variations in EOF.[25,39,140,155-158] This effect is exacerbated in microfluidic systems, such as those used here, that have a high surface-area-to-volume ratio and convection dominated by EOF. Indeed, simulations have shown

that significant changes in EOF rates throughout the channel length occur during ICP, and we think these same types of effects are operative during fICP.[151,159-161] *Because convection is limited to EOF, tracking the motion of fluorescent microbeads provides a proxy for the rate of EOF.*

Taking into account the data in Figures 3.3 and 3.4, we constructed a qualitative map of ion concentration (Illustration 3.3a) and the corresponding EOF variations (Illustration 3.3b). Three distinct regions are defined in Illustration 3.3. Region A is characterized by bulk flow until a zone of rapid EOF acceleration is encountered just upstream of the BPE cathode (Illustration 3.3b, red), as evidenced by the elongation or streaking of the microbead fluorescence signals (Movie A.2, Appendix A). This rapid acceleration in EOF is a consequence of the concentration gradient at the boundary between the bulk Tris buffer and the IDZ (Illustration 3.3a).

Region B lies between the poles of the BPE and is more complicated than region A. In the lower portion of the channel, current passing through the BPE results in a decrease in EOF (Illustration 3.3b, green), compared to the rate of EOF within the IDZ in region A (Illustration 3.3b, red).[35] *This local variation in EOF results in the single vortex observed in Figure 3.2d and Movies A.1 and A.2 in Appendix A. However, the channel bifurcation, flow*

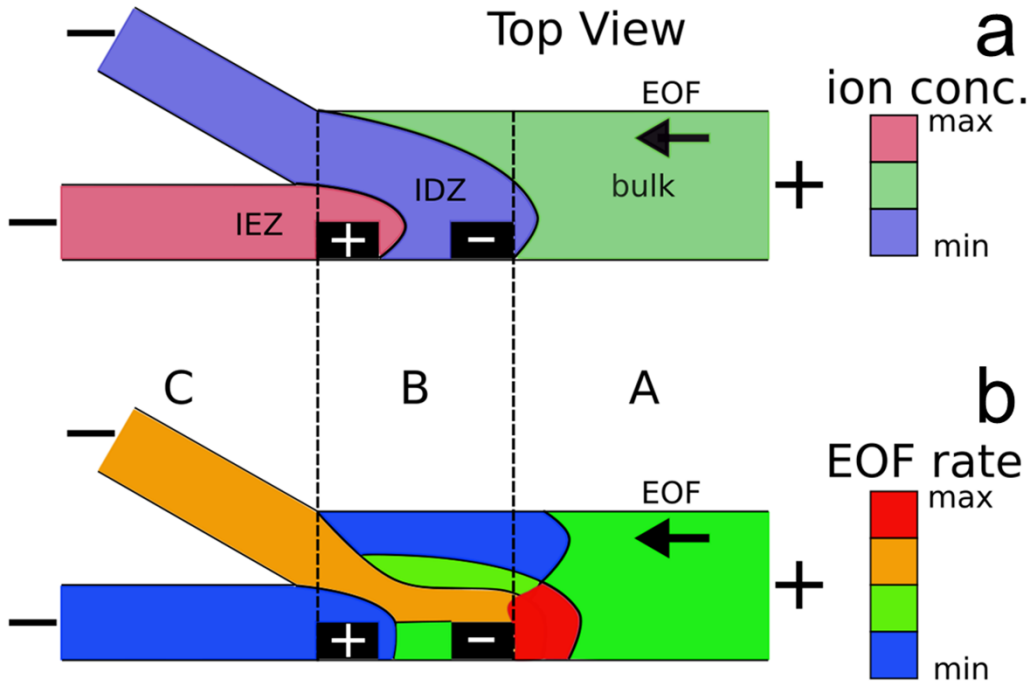

Illustration 3.3

displacement of the IDZ, and redirection of a significant portion of the current through the BPE complicate the local EOF between the poles of the BPE. Accordingly, advanced simulation studies, which will begin soon, are required to develop a comprehensive understanding of the processes in this region.

Region C is downstream of the BPE anode. The generation of H^+ at the BPE anode results in an increase in solution conductivity in the bottom channel leading to a local decrease in EOF (Illustration 3.3b, blue). In the top

channel, the decrease in solution conductivity during fICP, arising from flow displacement of the IDZ, results in a local increase in EOF (Illustration 3.3b, orange) compared to the bulk rate of EOF. This means there is a variation in the rate of EOF between the top and bottom channels. We propose this EOF gradient results in a pressure gradient near the channel bifurcation, which contributes to the continuous redirection and separation of microbeads into the top channel.[155,162]

3.5 Summary and conclusions

The key findings reported in this chapter are threefold. First, nearly 100% microbead redirection and separation may be achieved by fICP in a microelectrochemical device having a bifurcated channel. Second, the tracking of microbeads as they traverse the channel length permits visualization of local variations in EOF. Third, variations in solution conductivity in different regions of the channel lead to differences in EOF that exert a significant influence over microbead trajectory. These findings expand our fundamental understanding of fICP, thereby enabling its application to ion and particle redirection, separation, sorting, enrichment, and depletion. The results of these types of experiments, coupled with advanced simulations, will be reported in due course.

Chapter Four: Focusing, Sorting, and Separating Microplastics by Serial Faradaic Ion Concentration Polarization

4.1 Synopsis

In this chapter, we report continuous sorting of two microplastics in a trifurcated microfluidic channel using a new method called serial faradaic ion concentration polarization. Faradaic ion concentration polarization is an electrochemical method for forming ion depletion zones and their corresponding locally elevated electric fields in microchannels. By tuning the interplay between the forces of electromigration and convection during a faradaic ion concentration polarization experiment, it is possible to control the flow of charged objects in microfluidic channels. The key findings of this report are threefold. First, faradaic ion concentration polarization at two bipolar electrodes, configured in series and operated with a single power supply, yields two electric field gradients within a single microfluidic channel (i.e., serial faradaic ion concentration polarization). Second, complex flow variations that adversely impact separations during faradaic ion concentration polarization can be mitigated by minimizing convection by electroosmotic flow in favor of pressure-driven flow. Finally, serial faradaic ion concentration polarization within a trifurcated microchannel

is able to continuously and quantitatively focus, sort, and separate microplastics. These findings demonstrate that multiple local electric field gradients can be generated within a single microfluidic channel by simply placing metal wires at strategic locations. This approach opens a vast range of new possibilities for implementing membrane-free separations.

4.2 Introduction

In this chapter, we report focusing, sorting, and separating of charged microplastics using electrokinetic phenomena at bipolar electrodes (BPEs) operated in a series configuration. The results demonstrate that serial bipolar electrochemistry provides an experimentally simple approach to form and maintain multiple electric field gradients (EFGs) within a single microfluidic channel. Moreover, by tuning the orientation and dimensions of the BPEs, it is possible to simultaneously manipulate the flow of charged microplastics at multiple positions along the channel length. The results reported here illustrate the utility of serial bipolar electrochemistry for continuous separations generally and of microplastics specifically.

One of the most interesting approaches for controlling the motion of charged species within microchannels involves the use of ion depletion zones (IDZs) and their associated

electric fields.[17,25,48,163] *An IDZ refers to a region of solution containing fewer charge carriers, and thus exhibiting higher solution resistance, than the bulk. Consequently, when a voltage is applied across a microchannel containing an IDZ, a disproportionate amount of the voltage drops within the IDZ thereby yielding an EFG. Charged species experience enhanced electromigration along the EFG and, by tuning the rate of solution convection, their motion can be controlled within the microchannel.*

EFG focusing is a relatively simple method for controlling the motion of charged species.[13,14,16] *For example, consider the case of the negatively charged object shown in Illustration 4.1a. In this microfluidic experiment, the motion of the object is controlled by the interplay of two forces: convection and electromigration. When the object is at position A, the magnitude of the electric field is small, convection dominates electromigration, and the analyte moves from right to left. As it moves to the left, however, it encounters the IDZ and its associated locally enhanced electric field. Accordingly, at axial position B, the electric field strength is such that electromigration and convection are equal in magnitude but opposite in direction and therefore the net velocity of the analyte is zero. If the analyte were to diffuse to position C, the higher electric field*

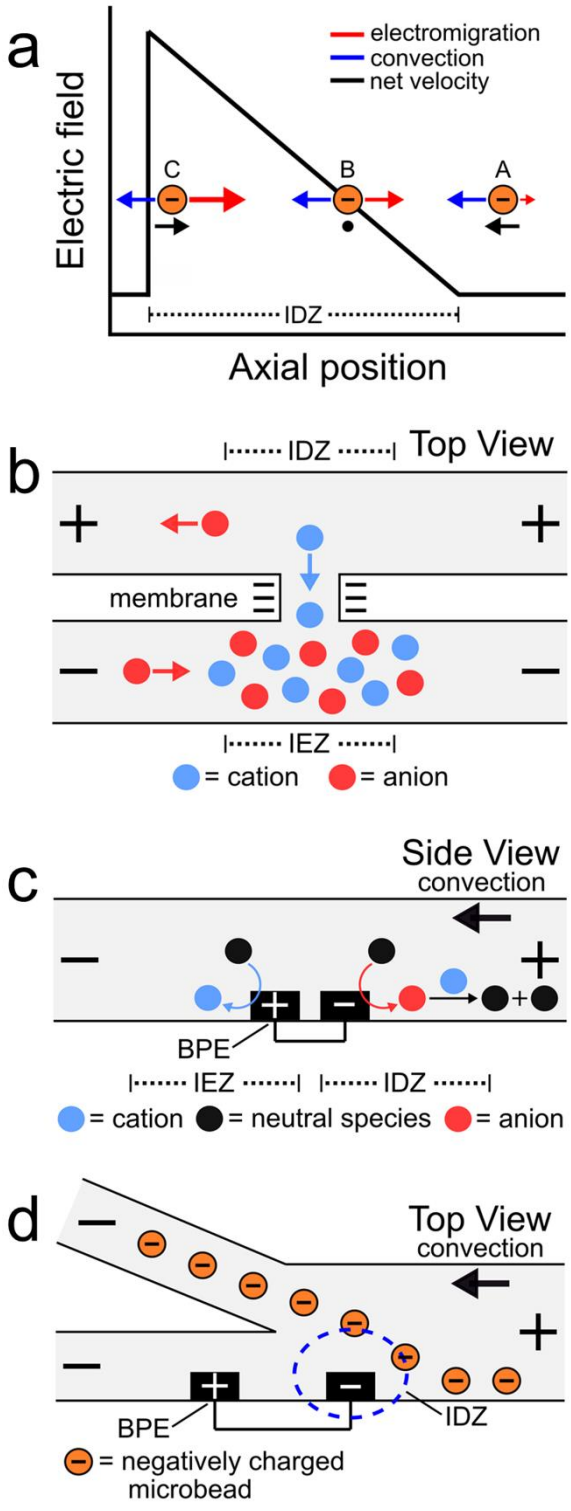

Illustration 4.1

would restore the object to position B. The net effect is that the object is focused at axial position B. In this way, EFGs have been used to enrich,[18,20,36,53,164,165] deplete,[54,143] and separate charged species.[70,134,144,166]

Some of the earliest reports describing EFG focusing in microfluidic systems relied on IDZs formed by ion concentration polarization (ICP).[17,18,20,48,167] ICP usually refers to the formation of concentration gradients near an ion-selective nanopore or membrane.[19] Illustration 4.1b depicts a cation-selective membrane separating two microfluidic channels. When a voltage of the indicated polarity is applied across the microfluidic channel network, the negatively charged membrane passes cations from the top channel to the bottom channel but rejects the passage of anions. To maintain electroneutrality throughout the system, anions migrate as indicated in the illustration. Accordingly, an IDZ forms near the membrane in the top channel and a region of enhanced ion concentration, termed an ion enrichment zone (IEZ), forms near the membrane in the bottom channel.

Several years ago we reported an electrochemical variant of ICP.[34,35] In this case, the IDZ forms via faradaic reactions proceeding at a BPE embedded within a microchannel containing a Tris buffer solution. This process, called faradaic ion concentration polarization

(fICP),[38] is shown in Illustration 4.1c. In this configuration, a BPE is patterned along the floor of a microfluidic channel. When a sufficient voltage is applied across the channel, faradaic water splitting proceeds at the ends of the BPE. Specifically, water reduction at the cathodic edge produces OH^- (red circle), which reacts with $TrisH^+$ (blue circle) present in solution (eqs 4.1 and 4.2), to produce neutral Tris. This neutralization reaction reduces the number of charge carriers in the vicinity of the cathodic pole of the BPE, thereby yielding an IDZ. To conserve charge, H^+ generation at the anodic edge of the BPE (eq 4.3) leads to an IEZ.[34]

$$\text{Cathode:} \quad 2\ H_2O + 2\ e^- \leftrightarrow 2\ OH^- + H_2 \qquad (4.1)$$

$$TrisH^+ + OH^- \leftrightarrow Tris + H_2O \qquad (4.2)$$

$$\text{Anode:} \quad 2\ H_2O \leftrightarrow 4\ H^+ + O_2 + 4\ e^- \qquad (4.3)$$

In 2018 we used fICP to continuously redirect and separate plastic microbeads within a bifurcated microchannel.[168] There were two main outcomes of this work. First, positioning the BPE, and thus the IDZ and EFG, across a portion of the channel width in the vicinity of the bifurcation enabled control over the direction of microbead flow (Illustration 4.1d). Second, the IDZ and IEZ led to local variations in the rate of electroosmotic flow (EOF) throughout the microchannel, and this also affected the trajectory of the microbeads.

In the present study, we used fICP to control the flow of two microplastics having different electrophoretic mobilities within a trifurcated microchannel. This was accomplished by configuring two BPEs in series and actuating them with a single power supply. This approach makes it possible to continuously focus, sort, and separate microplastics, and it represents a significant advance over our prior report because: (1) there are interesting, new challenges associated with implementing the complete and continuous separation of multiple objects (compared to steering one type of object in a particular direction) and (2) generating multiple local electric fields within a single channel by simply placing metal wires at strategic locations opens up a vast range of new possibilities for membrane-free separations.[169,170]

4.3 Experimental section

4.3.1 Chemicals

Polystyrene microbeads functionalized with surface carboxyl groups (diameter = 0.99 μm (μP1), 1.04 μm (μP2), and 0.20 μm (μP3)) were obtained from Bangs Laboratories, Inc. (Fishers, IN); FC04N, PC04N, and PC02N, respectively. BODIPY disulfonate fluorophore ($BODIPY^{2-}$) was obtained from Molecular Probes (Eugene, OR). Pluronic F108 was purchased from BASF (Florham Park, NJ). Tris-HCl buffer solution was

prepared by dissolving reagent-grade Trizma base (Sigma-Aldrich, St. Louis, MO) in deionized water (18.0 MΩ cm, Milli-Q Gradient System, MilliporeSigma, Burlington, MA) and then adjusting the solution pH to 8.1 using 1.0 M HCl (Fisher Scientific, Hampton, NH). Microfluidic channels were fabricated using poly(dimethylsiloxane) (PDMS) prepared from a silicone elastomer kit (Sylgard 184, Dow, Midland, MI).

4.3.2 Microfluidic device fabrication

Hybrid glass/PDMS microfluidic devices were fabricated using a previously reported procedure.[135] First, Pt microbands (10 nm Ti adhesion layer + 100 nm Pt, Kurt J. Lesker Company, Jefferson Hills, PA) were fabricated atop a glass slide using standard lift-off photo-patterning procedures. Second, 3 mm reservoirs were punched at the ends of a PDMS microfluidic channel (5 mm length, 200 µm width, 11.5 µm height). Third, the glass and PDMS were exposed to an O_2 plasma for 45 s (medium power, 60 W, PDC-32G, Harrick Scientific Products Inc., Ossining, NY) and then joined together. Fourth, the assembled device was heated in an oven at 65 °C for 5 min to ensure irreversible bonding. Trifurcated microfluidic channels were used in this study, and to ensure a uniform flow rate the width of each of the smaller channels was ~1/3 that of the main channel. The

microfluidic channel was positioned so that the Pt microbands spanned 20-25% of the main channel width.

4.3.3 Sorting experiments

Sorting experiments were performed as follows. First, equal heights of 10.0 mM Tris buffer solution (pH 8.1), containing either 1.0 µM BODIPY^{2-} and 1.5 pM µP1 or 150 fM µP2 and 190 pM µP3, were placed into the inlet and outlet reservoirs. To ensure that there was no pressure-driven flow (PDF) in the absence of a driving voltage, the motion of the plastic microbeads was monitored.[171] Second, a driving voltage was applied across the channel length using a power supply (PWS 4721, Tektronix, Beaverton, OR) connected to Pt electrodes located on the floor of each reservoir. Third, a BPE of the desired length was formed by connecting two Pt microbands by an external jumper wire. Finally, after sorting, the experiment was terminated by disconnecting the jumper wire from the Pt microbands and turning off the driving voltage. An electrometer (6517b, Keithley Instruments, Cleveland, OH), connected in series with the power supply, and a hand-held multimeter (AM-1118, Aktakom, Russia), connected in series with the BPE, were used to measure the current passed through the driving electrodes (i_{tot}) and the BPE (i_{BPE}), respectively.

4.3.4 Optical and fluorescence microscopy

The motion of microplastic particles and the $BODIPY^{2-}$ fluorophore during sorting experiments was visualized using an inverted fluorescence microscope (Eclipse TE 2000-U, Nikon, Japan) equipped with a CCD camera (Cascade 512, Photometrics, Tucson, AZ) controlled by V++ software (DigitalOptics Corporation, San Jose, CA). Image analysis was performed using ImageJ (National Institutes of Health, Bethesda, MD). Fluorescence measurements were performed with the fluorescence lamp (X-Cite 120Q, Excelitas Technologies Corp., Waltham, MA) on, while optical observations were performed with the lamp off.

4.3.5 Solution conductivity measurements

Solution conductivity measurements were obtained using a previously reported, home-built conductivity instrument.[136,137] Measurements were performed as follows. A function generator (Model 182A, Wavetek, San Diego, CA) was used to apply an ac sine wave (±0.30 V amplitude, 5 kHz frequency) to one Pt microband. The resulting current passed through solution to a detection microband patterned 30 μm (center-to-center) downstream, where it was amplified and converted back to a voltage by a transimpedance amplifier. The attenuation of the current passing through solution to the detection microband was related to solution

conductivity using a calibration curve (Appendix B). Conductivity measurements were carried out at 20 ± 2 °C.

4.3.6 Numerical simulations

Finite element simulations were carried out using the COMSOL Multiphysics version 5.4 software package (COMSOL Inc., Burlington, MA). Simulations were performed on a workstation (Precision T7500, Dell, Round Rock, TX) outfitted with 108 GB of RAM and dual Intel Xeon processors (2.40 GHz). All simulations were performed at steady state. A complete discussion of the theoretical background and details of the numerical simulations is provided in Appendix B.

4.4 Results and discussion

4.4.1 Sorting by electrophoretic mobility

The goal of this study is to continuously sort and separate two microplastics having different electrophoretic mobilities using fICP within a trifurcated microchannel. We begin, however, by controlling the motion of the BODIPY^{2-} fluorophore and a negatively charged microplastic (μP1) to develop a better understanding of processes fundamental to continuous sorting by fICP.

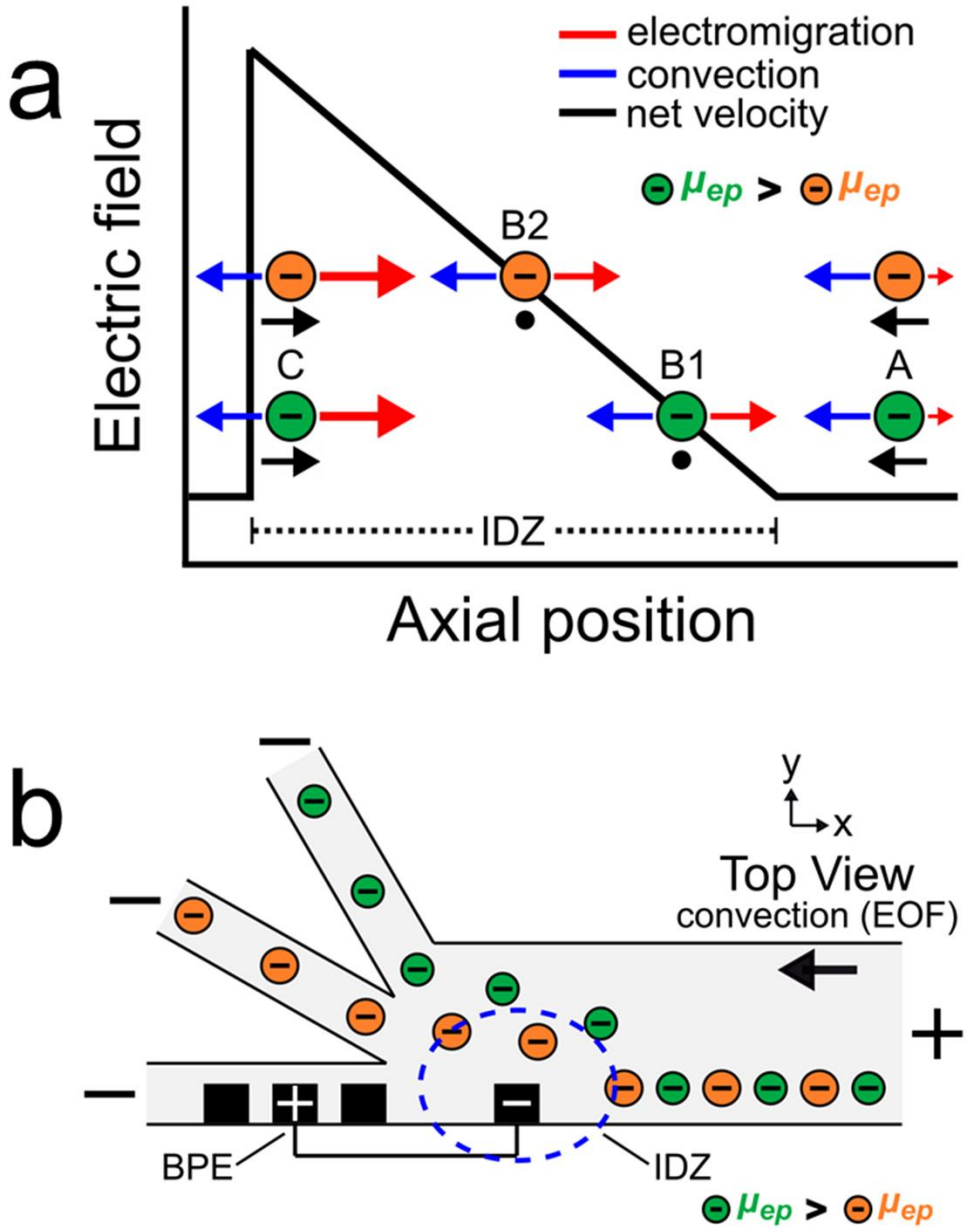

Illustration 4.2

Charged objects having different electrophoretic mobilities interact with EFGs in different ways.[13-15,134,172-174] *Consider, for example, EFG focusing of the two charged objects shown in Illustration 4.2a.*[37,70,144] *The*

interpretation of the motion of the charged objects in this illustration is essentially the same as that shown in Illustration 4.1a, except now there are two particles having different properties. The key point is that the object with the larger electrophoretic mobility (μ_{ep}, green) is focused at a position with a relatively low electric field (position B1), while the object with the smaller electrophoretic mobility (μ_{ep}, orange) is focused at a position having a relatively high electric field (position B2). Extrapolating from the concept embodied by this illustration, we thought it would be possible to continuously separate two charged objects having different electrophoretic mobilities.

Illustration 4.2b depicts the experimental system used to continuously sort two charged objects having different electrophoretic mobilities. It shows a BPE, formed from two microband electrodes,[36,144] positioned across a portion of the width of a trifurcated microchannel. When a sufficient driving voltage is applied across the channel length, an IDZ forms near the cathodic end of the BPE (blue dashed circle) due to fICP (eqs 4.1 and 4.2). The magnitude of the corresponding EFG is largest near the cathodic end of the BPE and decreases as a function of position across the channel width. The non-uniform EFG directs the trajectory of charged objects away from the BPE cathode and toward the upper sidewall of the microfluidic channel. Here, the

electric field is weak, convection dominates electromigration, and the objects flow downstream.[168]

If two charged objects interact with the EFG near the leading edge of the BPE in a similar way, their motion is controlled in a manner proportional to the magnitude of their electrophoretic mobility. Specifically, the object having the larger electrophoretic mobility (green) is repelled further away from the BPE cathode than the object having the smaller electrophoretic mobility (orange). Accordingly, by tuning the magnitude of electromigration and convection (by EOF) in the trifurcated channel, the flow of the green and orange objects can be directed into the top and middle outlet channels, respectively. Thus, the two objects are continuously sorted by their electrophoretic mobility and separated from the plastic-free solution flowing into the bottom outlet channel.

Actual sorting experiments were performed in a glass/PDMS microelectrochemical device having a trifurcated microchannel. The microchannel was positioned so that an array of microbands extended across 20-25% of the width of the main 200 µm-wide channel (Illustration 4.2b). A 750 µm-long BPE was formed near the trifurcation by connecting the two microbands shown in Illustration 4.2b with a jumper wire. The magnitude of the potential difference between the BPE ends and the solution (ΔE_{elec}) is approximately

proportional to the length of the BPE and the magnitude of the driving voltage.[66,68,69,145,175] *As mentioned earlier, the rate of PDF was set to zero prior to the experiment, and therefore solution convection was controlled only by EOF. Because the channel surfaces are negatively charged in the presence of Tris buffer (pH 8.1), application of a driving voltage having the polarity shown in Illustration 4.2b results in solution flow from right to left (in opposition to electromigration).*[148,176]

The sorting experiments were carried out as follows. First, equal heights of 10.0 mM Tris buffer solution (pH 8.1) containing 1.0 µM BODIPY^{2-} *(electrophoretic mobility = -3.4 µm cm/V s)*[34] *and 1.5 pM µP1 (electrophoretic mobility = -2.0 ± 0.5 µm cm/V s, see Appendix B for electrophoretic mobility measurement details) were placed into the inlet and outlet reservoirs. Second, a driving voltage of 25.0 V was applied across the channel length, resulting in EOF toward the negative driving electrodes (Illustration 4.2b). Third, the two microbands indicated in Illustration 4.2b were connected with a jumper wire to form a 750 µm-long BPE (*ΔE_{elec} *= ~3.8 V).*

Figure 4.1 is a pair of micrographs captured at steady state that display the location of µP1 and BODIPY^{2-} *in the trifurcated channel during a typical sorting experiment. Figure 4.1a is an optical micrograph showing that µP1 is*

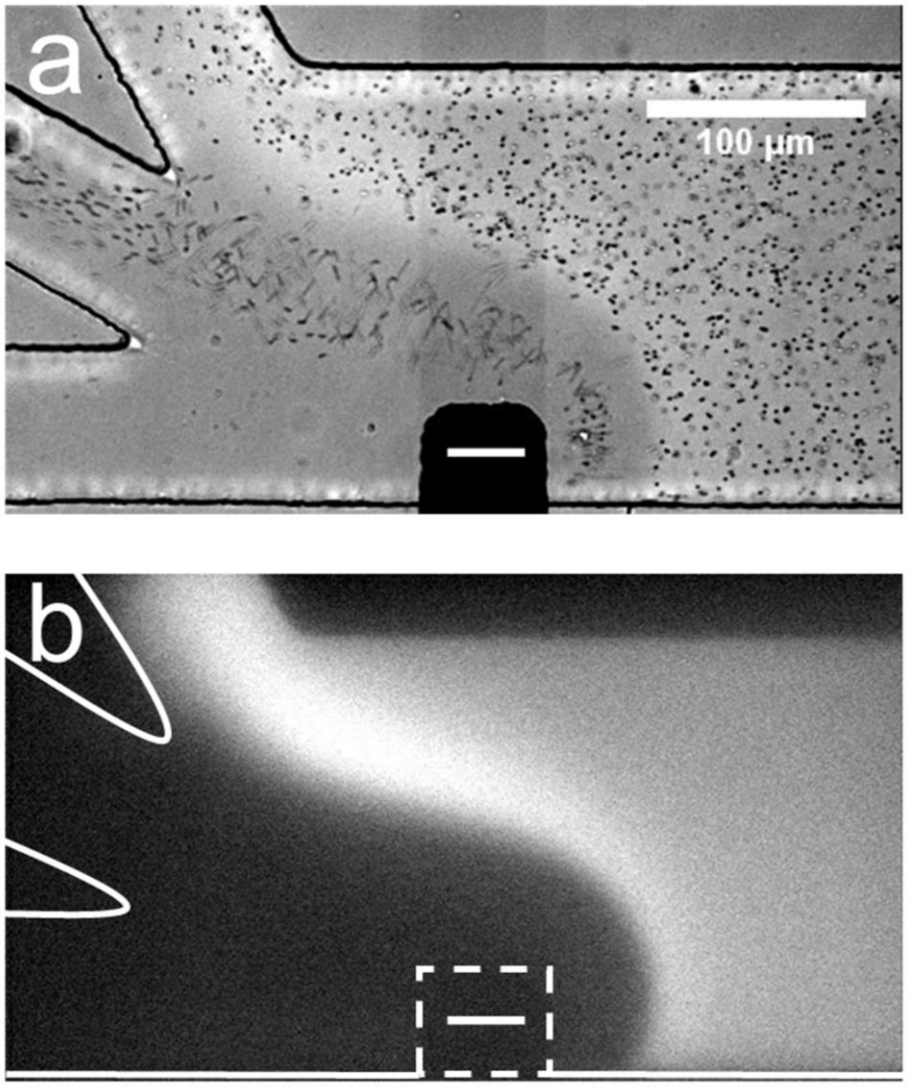

Figure 4.1

Sorting $BODIPY^{2-}$ and µP1 in a trifurcated microchannel. (a) Optical micrograph showing the location of µP1 during a sorting experiment. (b) Fluorescence micrograph showing the location of $BODIPY^{2-}$ during the same sorting experiment. The dashed white line in (b) indicates the location of the cathodic pole of the BPE, which is formed by connecting the two microwires shown in Illustration 4.2b. Solution contained 1.0 µM $BODIPY^{2-}$, 1.5 pM µP1, and 10.0 mM Tris buffer (pH 8.1). The driving voltage was 25.0 V and the BPE was 750 µm long. EOF was from right to left. Both micrographs were captured at steady state. The scale bar shown in (a) also applies to (b).

directed away from the bottom outlet channel and into the middle and top channels. Figure 4.1b is a fluorescence micrograph showing that BODIPY^{2-} is directed away from the bottom and middle outlet channels and into the top channel. A movie of the complete experiment is provided in Appendix B (Movie B.1).

The important point is that these results demonstrate that two charged objects can be continuously redirected and sorted along an EFG as depicted in Illustration 4.2b. In this case, BODIPY^{2-} has the larger electrophoretic mobility and is repelled further from the BPE than µP1 during fICP. Figure 4.1 also shows that sorting is imperfect. Specifically, all of the BODIPY^{2-} flowing past the cathodic pole of the BPE is directed into the top outlet channel, but µP1 is directed into both the middle and top outlet channel. The principal reason for some of µP1 being present in the upper outlet channel is that it does not encounter the strongest region of the EFG. That is, the magnitude of the EFG decreases as the distance from the BPE increases along the width of the microchannel. To address this issue, and thereby improve sorting efficiency, we thought it would be possible to focus BODIPY^{2-} and µP1 toward the lower sidewall of the main channel prior to their encounter with the strongest part of the EFG. This hypothesis is represented schematically in Figure 4.2a, discussed next.

4.4.2 Focusing and sorting by serial faradaic ion concentration polarization

So far we have shown that $BODIPY^{2-}$ and μP1 can be continuously redirected and sorted at a single BPE embedded within a trifurcated microchannel. However, only a fraction of the objects in solution interact with the highest EFG (in the vicinity of the BPE) in this configuration and, therefore, sorting is imperfect. Accordingly, to improve sorting efficiency, we designed a more sophisticated microelectrochemical device comprising two BPEs.

The diagram in Figure 4.2a is a top view of two BPEs (BPE1 and BPE2) positioned across a fraction of the width of a trifurcated channel. BPE1 is positioned near the upper sidewall of the channel upstream from the trifurcation, while BPE2 is positioned along the lower sidewall of the channel near the trifurcation. When a sufficient driving voltage is applied across the channel length, fICP (eqs 4.1 and 4.2) results in an IDZ near the cathodic pole of both BPE1 and BPE2 (blue dashed circles). Importantly, fICP at BPE1 continuously directs the flow of $BODIPY^{2-}$ and μP1 toward the lower sidewall of the channel. Accordingly, both objects encounter the strongest part of the EFG at BPE2 and both are more effectively redirected compared to when only a single BPE is present near the trifurcation.

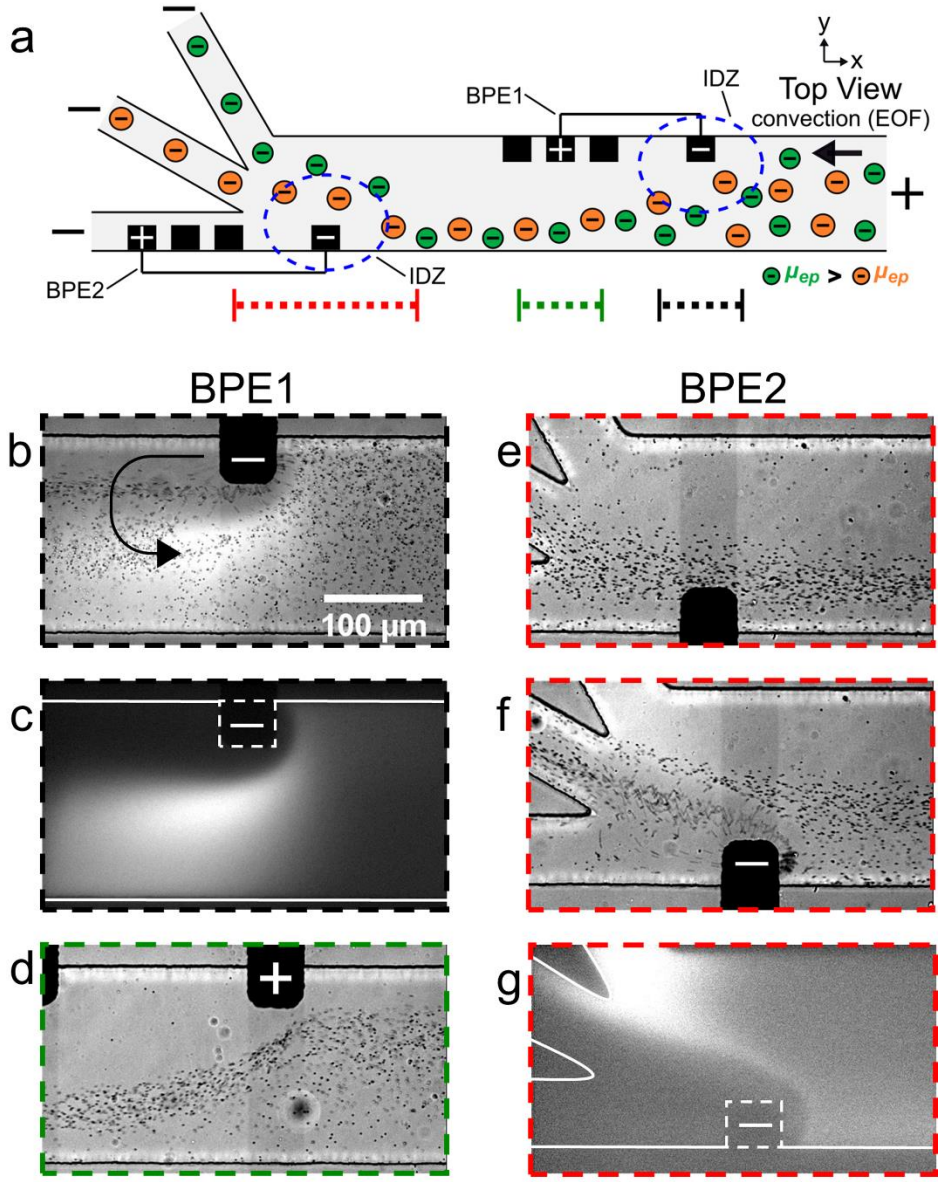

Figure 4.2

(a) Schematic illustration of the microfluidic configuration used for serial fICP experiments. For all frames except (e), both BPE1 and BPD2 were active. For frame (e), only BPE1 was active. (b-g) Series of optical and fluorescence micrographs showing the location of μP1 and $BODIPY^{2-}$ during serial fICP. With reference to the three dotted lines at the bottom of (a), the micrographs were captured along the portion of the channel length indicated by (b and c) the dotted black line; (d) the dotted green line; and (e-g) the

dotted red line. The curved black arrow in (b) indicates the location and the rotation direction (counterclockwise) of the vortex downstream of the cathodic pole of BPE1 (the vortex can be more easily visualized in Movie B.2 in Appendix B). The dashed white lines in (c) and (g) indicated the locations of the cathodic poles of BPE1 and BPE2, respectively. The solution contained 1.0 µM $BODIPY^{2-}$, 1.5 pM µP1, and 10.0 mM Tris buffer (pH 8.1). The driving voltage was 25.0 V. BPE1 was 750 µm long and BPE2 was 1000 µm long. EOF was from right to left. All micrographs were captured at steady state. The scale bar shown in (b) also applies to (c-g). Figure 4.2: continued.

The two-BPE focusing and sorting experiments were carried out as follows. First, equal heights of 10.0 mM Tris buffer solution (pH 8.1) containing 1.0 µM $BODIPY^{2-}$ and 1.5 pM µP1 were placed into the inlet and outlet reservoirs to ensure zero PDF. Second, a driving voltage of 25.0 V was applied across the channel length, resulting in EOF toward the negative driving electrodes. Third, two pairs of microband electrodes were connected with jumper wires to yield the two BPEs shown in Figure 4.2a. These BPEs extend across 20-25% of the width of the main 200 µm-wide channel, and the distance from the upstream edge of BPE1 to the upstream edge of BPE2 is 1460 µm. BPE1 is 750 µm long (ΔE_{elec} = ~3.8 V) and BPE2 is 1000 µm long (ΔE_{elec} = ~5.0 V).

The remaining frames in Figure 4.2 are a series of micrographs, captured at steady state, that reveal the location of $BODIPY^{2-}$ and µP1 along the channel length during a focusing and sorting experiment. Figure 4.2b is an optical micrograph captured along the portion of the channel

length indicated by the dotted black line at the bottom of Figure 4.2a. It shows that the presence of the cathodic pole of BPE1, and the associated fICP, changes the distribution of μP1 in the channel. Although it is difficult to see in this still image, there is also a single vortex (indicated by the curved black arrow in Figure 4.2b) that forms just downstream from the cathodic pole of BPE1. Both of these observations are more clearly visible in Movie B.2 (Appendix B). Figure 4.2c is a fluorescence micrograph captured at the same axial position as Figure 4.2b, and it shows that $BODIPY^{2-}$ is directed away from the cathodic pole of BPE1 during fICP. Figure 4.2d is an optical micrograph captured along the portion of the channel length indicated by the dotted green line in Figure 4.2a. It shows that μP1 is directed away from the anodic pole of BPE1 and toward the lower sidewall of the channel during fICP.

Taken together, Figures 4.2b-4.2d show that fICP at BPE1 significantly impacts the trajectory of $BODIPY^{2-}$ and μP1 as they traverse the channel length. While redirection near the cathodic edge of BPE1 results from the locally enhanced electric field in solution, the vortex shown in Figure 4.2b and the redirection in the vicinity of the BPE anode shown in Figure 4.2d are more complicated to explain. These latter two phenomena are related to formation of ionic concentration gradients in solution and will be discussed in

more detail later.[168] For now, however, the key point is that BPE1 focuses $BODIPY^{2-}$ and μP1 toward the lower sidewall of the channel upstream from BPE2 (Figures 4.2c and 4.2d).

Figure 4.2e is an optical micrograph captured along the portion of the channel length indicated by the dotted red line in Figure 4.2a. This micrograph was captured prior to connecting the microbands comprising BPE2 but with BPE1 active. It shows that μP1 is still focused in the lower half of the channel when it reaches the cathodic edge of BPE2.

Figure 4.2f is an optical micrograph captured at the same axial position as in Figure 4.2e, but with fICP proceeding at both BPE1 and BPE2 (i.e., serial fICP). It shows that the majority of μP1 is directed away from the cathodic pole of BPE2 and into the middle outlet channel. However, a portion of μP1 passes through the EFG formed near the cathodic pole of BPE2 and enters the bottom outlet channel. Figure 4.2g is a fluorescence micrograph captured at the same axial position as Figures 4.2e and 4.2f, and it shows that $BODIPY^{2-}$ is directed away from the cathodic pole of BPE2 and into the middle and top outlet channels.

Figures 4.2f and 4.2g confirm that the EFG near the cathodic pole of BPE2 sorts μP1 and $BODIPY^{2-}$ according to their electrophoretic mobility. Unfortunately, despite both species interacting with the strongest part of the EFG at

BPE2, sorting is still imperfect. The results shown in Figures 4.2b-4.2g demonstrate, however, that two BPEs, operated in series with a single power supply, can be used to form two IDZs and that the corresponding EFGs control the motion of charged species in a microchannel. This was a surprising finding because we thought that processes occurring at and near BPE1 might inhibit formation of a significant IDZ and EFG at BPE2. To better understand the distribution of solution species during serial fICP, as well as why sorting is incomplete, we performed in-situ solution conductivity measurements.

4.4.3 Solution conductivity measurements

Figure 4.3a is a simplified schematic illustration of the experimental configuration shown in Figure 4.2a. A table summarizing both experimental and simulated (discussed later) results from the solution conductivity measurements is also shown. The experimental measurements were carried out as described for Figure 4.2, except conductivity microbands (shown in red), positioned at least 1000 μm downstream from the trifurcation intersection, were used to measure the solution conductivity at steady state in each outlet channel. Conductivity measurements performed in each outlet channel with only the microbands comprising BPE1 connected (i.e., BPE1 "on") were assumed to represent,

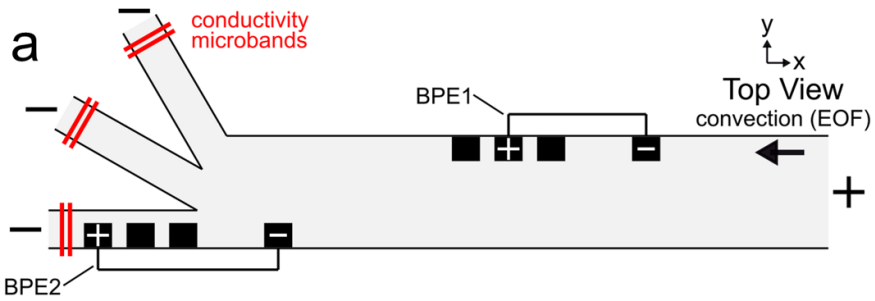

Experimental results

	Normalized solution conductivity with BPE1 "on"	Normalized solution conductivity with BPE1 and BPE2 "on"
Top outlet channel	1.27 ± 0.01	0.99 ± 0.02
Middle outlet channel	1.13 ± 0.02	0.22 ± 0.08
Bottom outlet channel	0.79 ± 0.01	2.03 ± 0.04

Simulated results

	Normalized solution conductivity with BPE1 "on"	Normalized solution conductivity with BPE1 and BPE2 "on"
Top outlet channel	1.15 ± 0.01	1.13 ± 0.01
Middle outlet channel	0.96 ± 0.01	0.77 ± 0.01
Bottom outlet channel	0.90 ± 0.01	1.1 ± 0.2

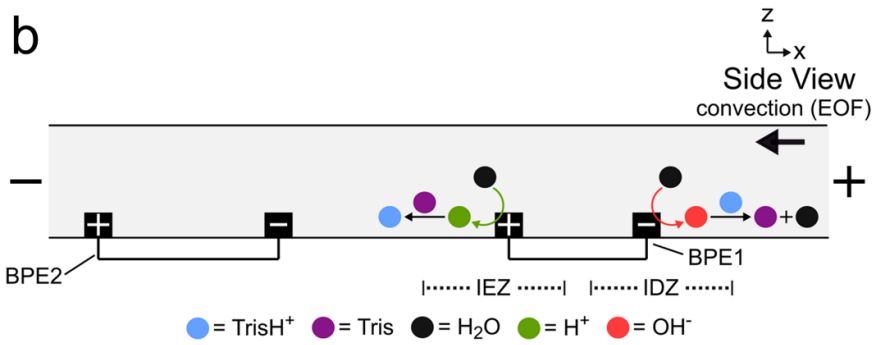

Figure 4.3

(a) Schematic illustration of the microfluidic configuration used to measure solution conductivity, and a table summarizing the results from direct, in-situ solution conductivity measurements (three replicates) and analogous numerical simulations. The conductivity measurements are normalized to the conductivity of the bulk solution. The solution contained 1.0 µM BODIPY^{2-}, 1.5 pM µP1, and 10.0 mM Tris buffer (pH 8.1). The driving voltage was 25.0 V. Both BPE1 (750 µm long) and BPE2 (1000 µm long) were connected for this experiment. EOF was from right to left. All measurements were performed at steady state. (b) Schematic illustration of the Tris buffer chemistry at BPE1 during serial fICP.

approximately, the conductivity of the solution between the downstream edge of BPE1 and the upstream edge of BPE2 during focusing and sorting experiments.[177-181] *Conductivity measurements performed with the microbands comprising both BPE1 and BPE2 connected (i.e., BPE1 and BPE2 "on") are characteristic of the conductivity of solution in each outlet channel during focusing and sorting experiments. The results in the table are normalized to the conductivity of the bulk solution (bulk = 1.00) and represent the average of three measurements.*

The tabulated experimental data in Figure 4.3a reveal two key findings. First, the three values shown in the first column of the table are fairly close to the normalized bulk conductivity of 1.00. This means that forming an IDZ and IEZ near the anodic and cathodic poles, respectively, of BPE1 does not greatly change the conductivity of solution downstream from BPE1. We believe this is related to Tris buffer chemistry. Specifically, just as OH^- *produced at the cathodic end of a BPE neutralizes* $TrisH^+$ *(eqs 4.1 and 4.2),* H^+ *produced at the anodic pole converts Tris to* $TrisH^+$ *(eqs 4.3 and 4.4).*[182] *In this way,* $TrisH^+$ *molecules neutralized near the cathodic pole of BPE1 are reionized in the vicinity of the anodic pole of the same BPE, as illustrated in Figure 4.3b. Regeneration of* $TrisH^+$ *acts to conserve the conductivity (and presumably the composition) of the*

solution upstream from BPE1 and BPE2 and is critical to the success of serial fICP.

$$Tris + H^{+} \leftrightarrow TrisH^{+} \qquad (4.4)$$

Second, the data presented in the second column show that solution conductivity is significantly different in each outlet channel during serial fICP experiments. Specifically, solution conductivity is increased in the bottom outlet channel, decreased in the middle outlet channel, and nearly unchanged in the top outlet channel vs. bulk solution. This is important because conductivity variations of the magnitudes measured with BPE1 and BPE2 "on" are known to yield non-uniform EOF within microfluidic channels.[25,26,43,50,140,159,160,162,168] *For the experiments discussed so far, where solution convection is controlled by EOF, local variations in the rate of EOF can impact the performance of focusing and sorting by serial fICP.*

To summarize, solution conductivity measurements performed with BPE1 "on", as well as with BPE1 and BPE2 "on", improve our understanding of the mechanism of serial fICP and reveal significant variation between the conductivity of solution in each outlet channel. To better understand how these local variations in solution conductivity impact the rate of solution convection throughout the microfluidic channel, we performed numerical simulations.

4.4.4 Numerical simulations

We used the finite element method to solve numerical simulations and gain additional insight into the experimental results of focusing and sorting by serial fICP. Steady-state simulations were performed using a two-dimensional (2D) model based on the xy-plane of the microelectrochemical device illustrated in Figure 4.2a.

A complete description of the theoretical background and simulation methods is provided in Appendix B. Briefly, however, solution convection was calculated using the Navier-Stokes equation. The electric double layer is considerably smaller than the channel dimensions (thin double layer approximation), and thus EOF was modeled as a slip condition imposed at the channel walls and formulated according to the Helmholtz-Smoluchowski equation.[35,183] *Mass transport was resolved by the Nernst-Planck equation and the electroneutrality condition. The electric field in solution was determined from the steady-state currents passed through the driving electrodes (i_{tot}) and the BPEs (i_{BPE1} and i_{BPE2}) as well as solution conductivity. The electrochemical reactions (eqs 4.1 and 4.3) at the BPEs were modeled as fluxes, and the Tris buffer chemistry (eqs 4.2 and 4.4) was modeled using reaction rate constants.*[35]

Figure 4.4a is a plot of the simulation domain. This asymmetric experimental system was approximated in 2D by

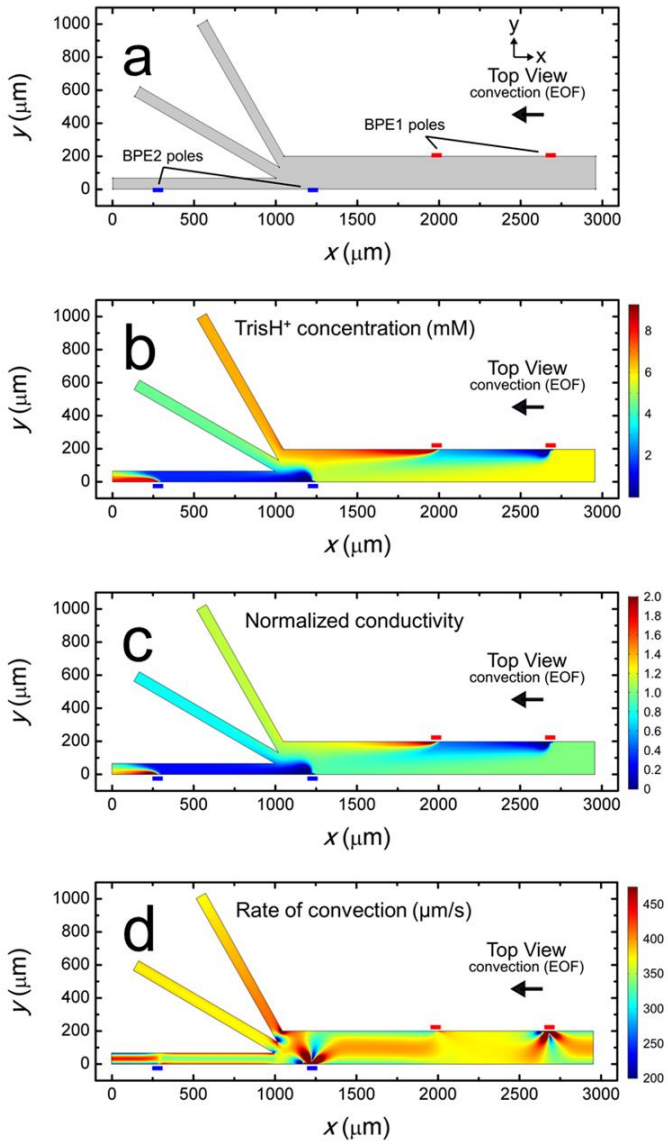

Figure 4.4

Steady-state simulation results for a solution containing 10.0 mM Tris buffer (pH 8.1), and with i_{tot} = 1.32 μA, i_{BPE1} = 0.60 μA, and i_{BPE2} = 0.74 μA (i.e., BPE1 and BPE2 "on"). (a) Plot of the 2D model domain. The red and blue rectangles indicate the positions of the poles of BPE1 and BPE2, respectively. (b) Distribution of TrisH⁺ along the channel length. (c) Plot of solution conductivity throughout the channel. Conductivity values are normalized to the conductivity of the bulk solution. (d) Plot of the rate of convection along the channel length during serial fICP.

positioning the BPEs along the channel sidewalls. The location of the poles of BPE1 and BPE2 are indicated by the small red and blue rectangles, respectively. The x- and y-axes refer to the channel length and width, respectively.

Figure 4.4b is a plot of the distribution of $TrisH^+$ during a focusing and sorting experiment (i.e., both BPEs "on"). It shows that the concentration of $TrisH^+$ decreases in the vicinity of the cathodic poles of each BPE but increases near their anodic poles. This finding is in accord with our understanding of Tris buffer chemistry (eqs 4.1-4.4). Furthermore, Figure 4.4b shows that the concentration of $TrisH^+$ near the leading edge of BPE2 (~5.3 mM at x = 1300 µm, y = 0-100 µm) is similar to that of the bulk solution upstream from BPE1 (5.8 mM at x = 2900 µm). This finding confirms that fICP at BPE1 does not significantly impact the concentration of $TrisH^+$ near the leading edge of BPE2.

Figure 4.4c is a plot of the solution conductivity normalized to the conductivity of bulk solution. The trends in this plot are nearly identical to those shown in Figure 4.4b for the concentration of $TrisH^+$. Specifically, the prominent features of this plot are IDZs and IEZs in the vicinity of the cathodic and anodic poles, respectively, of the BPEs. Additionally, the normalized solution conductivity just upstream from BPE2 (x = 1300 µm) is ~0.9

at the lower sidewall of the channel (y = 0 µm) and ~1.2 at the upper sidewall (y = 200 µm). Finally, the solution conductivity 1000 µm downstream from the trifurcation is increased in the bottom outlet channel, decreased in the middle outlet channel, and nearly unchanged in the top outlet channel vs. bulk solution. Importantly, the conclusions relating to Figure 4.4c, and those derived from the experimental conductivity measurements (Figure 4.3a), are nearly the same.

To better compare the results of the numerical simulations to the solution conductivity measurements in Figure 4.3a, we also performed simulations with only BPE1 "on" (Appendix B). The conductivity of the simulated solution at the left end of each outlet channel (1000 µm downstream from the trifurcation) in this case is shown in the first column of the lower part of the table in Figure 4.3a. Each value represents the average conductivity of solution across the width of the indicated channel and is normalized to the conductivity of bulk solution. These results are in reasonable agreement with the experimental results in the top part of the table. We conclude that the electrochemical (eqs 4.1 and 4.3) and chemical (eqs 4.2 and 4.4) reactions included in the numerical model appropriately describe fICP at a BPE.

Simulation results analogous to those discussed in the previous paragraph and related to those in Figure 4.4c (both BPEs "on") are shown in the second column of the lower part of the table in Figure 4.3a. The significant differences between the simulated and experimentally measured conductivities in this case are likely related to geometric effects. Specifically, in the experimental device, the BPE poles extend across 20-25% of the width of the 200 µm-wide main channel (as shown in Figure 4.2a), whereas in the simulations the BPEs are flush with the sidewalls. Therefore, in the experiments (but not in the simulations), a significant portion of the $TrisH^+$ neutralized near the cathodic pole of BPE2 flows downstream and enters the middle outlet channel. Thus, flow displacement of the IDZ leads to the measurement of a significant decrease in solution conductivity in the middle outlet channel.[168] *Likewise, the amount of H^+ generated at the anodic pole of BPE2 exceeds the amount of neutralized $TrisH^+$ in the bottom outlet channel, and thus a significant increase in solution conductivity is measured in the bottom outlet channel. Additional details are provided in the context of Figure B.3 in Appendix B.*

The rate of convection along the channel length is plotted in Figure 4.4d. It shows that the rate of convection varies significantly near the poles of the BPEs

and the channel trifurcation. The main finding extracted from Figure 4.4d is that serial fICP produces significant and complex flow variations within the microelectrochemical device when convection is controlled by EOF. Flow variations of the type shown in Figure 4.4d account for the experimentally observed microplastic vortexing near the cathodic pole of BPE1 (shown in Figure 4.2b) and microplastic redirection near the anodic pole of BPE1 (Figure 4.2d). Furthermore, it is likely that complex flow near the cathodic pole of BPE2 and the channel trifurcation limits the performance of sorting and focusing by serial fICP. More detailed information relating to Figure 4.4d is provided in Appendix B. To address the complexity of the flow, however, we developed a method for minimizing these effects. This is discussed next.

4.4.5 Focusing, sorting, and separating by serial faradaic ion concentration polarization

The effectiveness of serial fICP depends on convection via EOF. As we demonstrated in the previous section (Figure 4.4d), however, EOF is complex and varies along the channel length. To address this issue, we now turn our attention to suppressing EOF and controlling convection by PDF.[50,184]

Serial fICP experiments were performed in a microelectrochemical device identical to the one previously described in the context of Figure 4.2a. Following

fabrication, however, the surfaces of the microchannel were modified by flowing 10.0 mM Tris-HCl solution (pH 8.1) containing 5.0 µM of the non-ionic surfactant Pluronic F108 through the channel for 21 h by PDF.[37,39,40] *Pluronic treatment suppressed the rate of EOF within the microchannel by 49 ± 8% (three replicates) for at least 2 h following treatment.*[185]

Following treatment of the channel surfaces with Pluronic, sorting experiments were carried out as follows. First, different heights of 10.0 mM Tris buffer solution (pH 8.1) containing 150 fM µP2 (electrophoretic mobility = -2.4 ± 0.5 µm cm/V s) and 190 pM µP3 (electrophoretic mobility = -4 ± 1 µm cm/V s, see Appendix B for electrophoretic mobility measurement details) were placed into the inlet and outlet reservoirs resulting in PDF (32 ± 3 nL/min, seven replicates) toward the trifurcation. Second, a driving voltage of 25.0 V was applied across the channel length resulting in EOF toward the negative driving electrodes. Therefore, in this experiment, convection is by both EOF and PDF. Third, two pairs of microband electrodes were connected with jumper wires to yield a pair of BPEs configured as in Figure 4.2a. In this case, BPE1 and BPE2 are both 1000 µm long (ΔE_{elec} = ~5.0 V).

Figure 4.5 is a series of optical micrographs captured at steady state during serial fICP. Figure 4.5a was

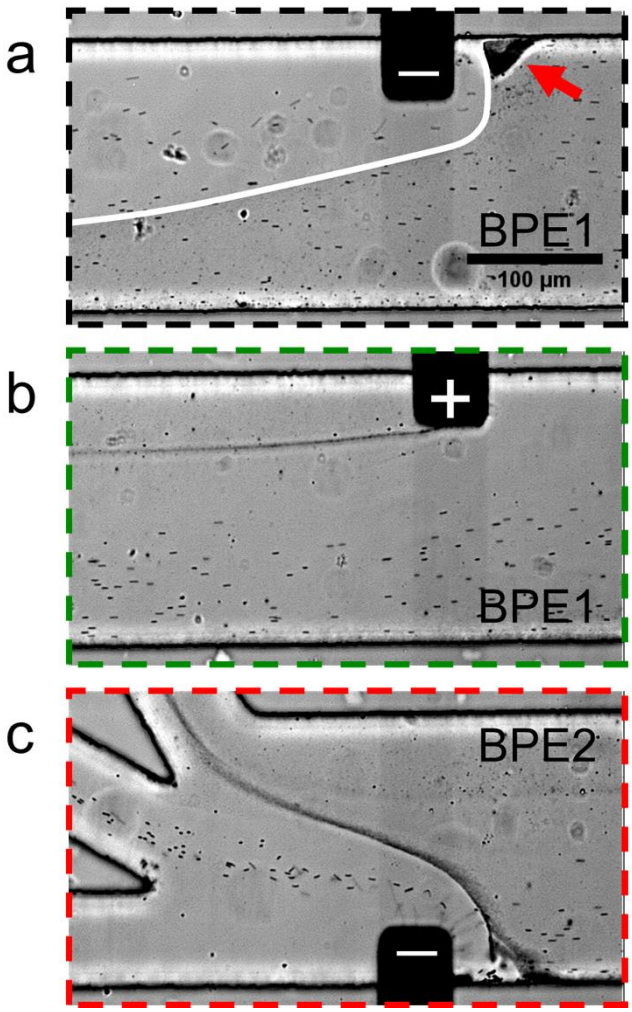

Figure 4.5

Series of micrographs showing the location of µP2 and µP3 during serial fICP (both BPE1 and BPE2 active and 1000 µm in length). Optical micrographs captured along the portion of the channel length indicated by (a) the dotted black line, (b) the dotted green line, and (c) the dotted red line at the bottom of Figure 4.2a. The white line in (a) indicates the approximate boundary between solution containing µP3 (below) and µP3-free solution (above). The red arrow in (a) indicates a region of the channel in which microplastics are retained. The solution contained 150 fM µP2, 190 pM µP3, and 10.0 mM Tris buffer (pH 8.1). The driving voltage was 25.0 V. PDF (32 ± 3 nL/min, seven replicates) and EOF were from right to left. All micrographs were captured at steady state. The scale bar shown in (a) also applies to (b) and (c).

captured along the portion of the channel length indicated by the dotted black line at the bottom of Figure 4.2a. It shows that the EFG in the vicinity of the cathodic pole of BPE1 directs μP2 and μP3 toward the lower sidewall of the channel. Note that μP3 is too small (0.20 μm) to be visualized as discrete particles, and therefore it appears as a slightly darker gray haze below the white line that has been added to this image. The red arrow in Figure 4.5a also indicates that some microplastics stack just upstream from the BPE1 cathode. At this location, the forces of electromigration and convection are equal in magnitude but opposite in direction, and thus the microplastics are focused here.

Figure 4.5b was captured along the portion of the channel length indicated by the dotted green line in Figure 4.2a. It shows that processes at the anodic pole of BPE1 have little to no impact on the flow of the majority of the microplastics. However, this micrograph shows a stream of μP3 downstream of the edge of the anodic pole. This is likely due to electrostatic interactions between the negatively charged microplastics and the positively charged anodic pole of BPE1.

Figure 4.5c is a micrograph captured along the portion of the channel length indicated by the dotted red line in Figure 4.2a. It shows that the IDZ and corresponding EFG

near the cathodic pole of BPE2 direct μP2 and μP3 into the middle and top outlet channels, respectively. Accordingly, the two microplastics are nearly quantitatively sorted according to their electrophoretic mobility, and they are completely separated from the solution flowing into the bottom outlet channel. A movie of the complete experiment is included in Appendix B (Movie B.3). The main point relating to Figure 4.5 is that by suppressing EOF and controlling convection primarily by PDF, the types of flow variations apparent in Figure 4.4d are minimized. This results in greatly enhanced separation efficiency of the two types of microplastics.

4.5 Summary and conclusions

In this chapter, we have reported three key findings. First, serial bipolar electrochemistry enables simultaneous formation of two IDZs, and their corresponding EFGs, within a single microfluidic channel and using just a single power supply. Second, complex flow variations that adversely impact separations during fICP can be mitigated by minimizing EOF in favor of PDF. Finally, serial fICP within a trifurcated microchannel results in continuous and quantitative focusing, sorting, and separating of microplastics. These results represent a significant advancement of our understanding of processes fundamental to

fICP and their application to continuous and precise control of the flow of multiple charged objects. In the future, we plan to develop alternative approaches to fICP that do not rely on buffer chemistry. Success in this endeavor will increase the types of solutions in which the motion of charged objects can be controlled by fICP. The results of these experiments will be reported in due course.

Chapter Five: Effect of Chloride Oxidation on Local Electric Fields in Microelectrochemical Systems[2]

5.1 Synopsis

We recently reported that electrochemical oxidation of Cl^- to neutral Cl_2 decreases solution conductivity, thereby yielding a local electric field gradient. Here, we report detailed experimental results and simulations indicating that the situation is more complex than we originally thought. The key new findings are twofold. First, once generated, Cl_2 rapidly reacts with water to form ionic species that increase, rather than decrease, solution conductivity near the anode. Second, the electrochemical potential gradient measured in the vicinity of the anode during Cl^- oxidation is dominated by differences in the chemical potential, rather than the electrical potential, of the solution. These findings clarify the electrochemical and chemical processes previously reported to enable desalination via faradaic Cl^- oxidation.

[2] *The work described here was previously published: Davies, C. D.; Johnson, S. E.; Crooks, R. M. Effect of chloride oxidation on local electric fields in microelectrochemical systems. ChemElectroChem* **2019**, *6*, 4867-4876. *CDD, SEJ, and RMC planned the experiments; CDD and SEJ performed the experiments; CDD performed the numerical simulations; CDD and SEJ analyzed the results; CDD wrote the article; CDD, SEJ, and RMC edited the article; and RMC supervised the research.*

5.2 Introduction

Several methods have recently been reported for manipulating the trajectory of ions in microfluidic devices,[186-190] and in some cases these methods have been applied to the desalination of salt water.[54,71,152,191,192] With regard to the latter, the approach that has received the most attention relies on the presence of an ion depletion zone (IDZ).[17] An IDZ is a region within a solution that has a lower ionic strength, and hence higher solution resistance, than the bulk. Accordingly, when a voltage is applied across a microfluidic device containing an IDZ, a disproportionate amount of the voltage is dropped in the IDZ and a local electric field gradient (EFG) forms in solution. Along the locally elevated electric field, ions experience enhanced electromigration, and, importantly, if convective forces also act on the ions, mass transport can be controlled in interesting ways.

EFG focusing is perhaps the simplest approach to manipulating ions along an EFG.[13,15,16] Consider a cation located at axial position *A* in Illustration 5.1a. Here, the local electric field is weak, convection dominates electromigration, and the cation moves from left to right. When the cation reaches position *B*, the magnitude of the electric field is such that electromigration balances convection and the cation experiences zero net force.

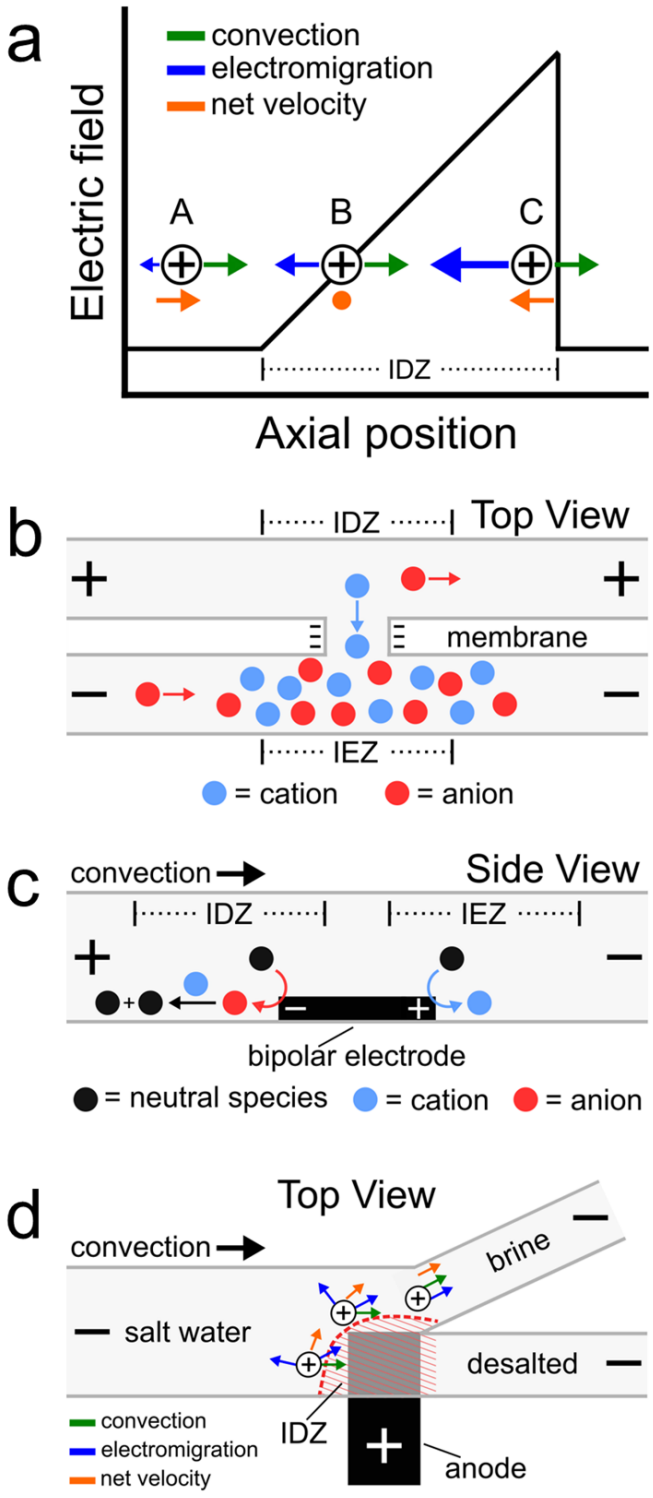

Illustration 5.1

However, if the ion were to diffuse to position C, electromigration would return the ion to position B. The net result is that, at steady state, all of the cations of interest within a channel are focused at position B. By tuning the magnitude of convection and electromigration, as well as the shape of the EFG within a channel, this approach has been used to focus,[38,193,194] deplete,[143] and separate ions.[54,71,195]

In an early example of microfluidic-based desalination, the IDZ was formed by taking advantage of an ion-selective membrane contained within a microfluidic system.[54] This type of device was configured as shown in Illustration 5.1b. Here, two microchannels are connected by the membrane. Due to the presence of excess negative charge, the membrane is permeable to cations but rejects the passage of anions. When a voltage is applied as shown in the illustration, cations migrate from the top channel to the bottom channel through the membrane, and to maintain charge neutrality anions migrate toward the anodes. Accordingly, an IDZ forms near the junction of the top channel and the membrane. A corresponding region of increased ionic strength, termed an ion enrichment zone (IEZ), forms in the bottom channel. Alternative approaches for forming an IDZ using selective membranes have also been reported.[18,196-198]

In 2008, we reported an electrochemical means for generating an IDZ.[34] In this approach (Illustration 5.1c), an IDZ forms in the vicinity of a bipolar electrode microfabricated within a fluidic channel.[66-68,145,199] When an appropriate electric field is applied across the bipolar electrode, it develops anodic and cathodic poles that can drive faradaic electrochemical processes. For example, a neutral water molecule can be reduced to form OH^- at the cathode (i.e., Illustration 5.1c, red circle). If a buffer cation, such as $TrisH^+$ (blue circle), is also present in solution, OH^- will neutralize it (eqs 5.1 and 5.2) resulting in a local IDZ. To conserve charge, the water oxidation reaction proceeds at the bipolar electrode anode (eq 5.3), and this leads to formation of an IEZ.

$$\text{Cathode:} \quad 2\ H_2O + 2\ e^- \leftrightarrow 2\ OH^- + H_2 \qquad (5.1)$$

$$TrisH^+ + OH^- \leftrightarrow Tris + H_2O \qquad (5.2)$$

$$\text{Anode:} \quad 2\ H_2O \leftrightarrow 4\ H^+ + O_2 + 4\ e^- \qquad (5.3)$$

This electrochemical approach represents a membrane-free and potential-selective method to form an IDZ, and therefore an EFG, adjacent to a mechanically robust electrode. We have shown that the resulting EFG can be used to concentrate ions by 500,000 fold,[38] separate and enrich ions having different mobilities,[39] and continuously redirect and separate microplastics into a secondary channel.[168]

In 2013, we applied the approach described in the previous two paragraphs to desalination.[71,72] *Illustration 5.1d is a representation of the device and the processes that we believed led to desalination. In the presence of salt water, application of a sufficient voltage between an anode positioned at the bifurcation of a Y-shaped channel, and cathodes located in the channel reservoirs, results in electrochemical oxidation of* Cl^- *at the anode (eq 5.4). Oxidation of charged* Cl^- *to neutral* Cl_2 *lowers the concentration of ions near the anode and leads to the formation of an IDZ and EFG. If convection and electromigration along the locally enhanced field are similar in magnitude, then ions are directed away from the anode and into the top channel.*[168] *However, neutral water molecules pass through the EFG unaffected. Thus, an EFG separates a salt water feed into brine and desalted water streams. To conserve charge and maintain electroneutrality, the water reduction reaction proceeds at cathodes located in the channel reservoirs (eq 5.1).*

$$2\ Cl^- \leftrightarrow Cl_2 + 2\ e^- \qquad (5.4)$$

Two experimental results led us to the foregoing interpretation. First, fluorescence measurements performed when the salt solution contained a charged fluorophore as an ionic tracer revealed a decrease in fluorescence intensity in the bottom (desalted) channel during desalination

experiments. Second, experiments intended to measure the electric potential profile in solution revealed a local potential gradient near the anode in the presence of Cl^- (but not in its absence). On the basis of the following four observations, therefore, we concluded that this microelectrochemical approach leads to desalination. First, the experiments discussed in the context of Illustration 5.1c operate exactly as described earlier and are analogous to the mechanism represented in Illustration 5.1d. Second, an ionic fluorescent tracer exhibited decreased fluorescence in the desalted microchannel. Third, an apparent EFG near the anode, which is necessary for forming an IDZ, was found to be present. Fourth, numerical simulations corroborated the experimental results.[73]

More recently, however, we reevaluated these findings and discovered that the electrochemical and chemical processes occurring in the microfluidic system represented in Illustration 5.1d are more complex and subtle than we originally believed. Specifically, and most importantly, we neglected to account for the fact that electrochemically generated Cl_2 undergoes a rapid reaction in water that yields ionic products.[200–203] *As we discuss in this chapter, these products quench the IDZ and, hence, the EFG.*

5.3 EXPERIMENTAL SECTION

5.3.1 Chemicals

Fluorescent (Dragon green; Ex. 480 nm, Em. 520 nm) polystyrene microbeads (fμB, nominally 1 μm in diameter), surface functionalized with carboxyl groups, were obtained from Bangs Laboratories (FC04F, Fishers, IN). Reagent-grade NaCl and Na_2SO_4 were obtained from Fisher Scientific (Hampton, NH). All solutions were prepared using deionized water (DI water, 18.0 MΩ cm, Milli-Q Gradient System, Millipore, Burlington, MA). The poly(dimethylsiloxane) kit (PDMS, Sylgard 184) was obtained from Dow Silicones Corp., Midland, MI.

5.3.2 Microfluidic device fabrication

Hybrid glass/PDMS microfluidic devices were prepared as previously reported.[71,135] First, Pt microwires (10 nm Ti adhesion layer + 100 nm Pt, Kurt J. Lesker, Jefferson Hills, PA) were patterned atop a glass slide using standard lift-off photo-patterning procedures. Second, a straight PDMS microchannel (5.0 mm long, 23 μm high, 117 μm wide) was fabricated by replica molding,[148] and then reservoirs (~3 mm diameter) were punched at either end of the microchannel. Third, the two halves of the device were exposed to an O_2 plasma for 45 s (medium power, 60 W, model PDC-32G, Harrick Scientific, Ithaca, NY). Fourth, the PDMS microchannel was

oriented such that the microbands extended across the width of the channel (Figure 5.1b). Finally, the device was cured at 65 °C for 5 min to promote irreversible bonding of the PDMS and glass.

5.3.3 Electrochemical experiments

Electrochemical experiments were performed as follows. First, a solution containing 50.0 mM NaCl and 13 fM fμB was flowed through the microchannel by pressure-driven flow (PDF) arising from a difference in solution heights in the channel reservoirs. As discussed later, the speed of fμB is used to calculate the flow rate of the solution. Next, a battery pack composed of two 1.5 V AA batteries (Duracell, Bethel, CT) was used to apply a 3.0 V bias between the Pt anode microband (50 μm long, 117 μm wide), located in the center of the microchannel, and Pt cathodes patterned on the floor of the reservoirs (Figure 5.1a). A hand-held digital multimeter (AM-1118, Aktakom, Russia), connected in series with the battery pack, was used to measure the current passed between the anode and the cathodes. As the experiment proceeded, electrochemical potential (ECP) measurements or solution conductivity measurements were performed to characterize the solution in the vicinity of the anode. These procedures were repeated with a Cl^--free control solution containing 50.0 mM Na_2SO_4 and 13 fM fμB.

5.3.4 Electrochemical potential measurements

The ECP profile near the anode was characterized using a scanning digital multimeter (Model 2700, Keithley Instruments, Cleveland, OH) in conjunction with a multiplexer module (Model 7701, Keithley) connected to Pt microbands 1-12 (Figure 5.1b).[36,71] The ECP difference between neighboring microbands was measured using the scanning digital multimeter operated in voltage mode. The measurement acquisition time was ~0.1 s and the voltage between each pair of microbands was measured every 2.0 s. The length of the measurement microbands is 15 μm and the center-to-center spacing is 30 μm, except for microbands 8 and 9. Those two microbands span the 50 μm-wide anode and thus have a center-to-center spacing of 95 μm. The data were recorded and processed using ExceLINX software (Tektronix, Beaverton, OR).

5.3.5 Solution conductivity measurements

The microbands used to determine the ECP profile were also used to measure solution conductivity. The procedure has been reported previously.[136,137,204,205] Briefly, a function generator (Model 182A, Wavetek, San Diego, CA) was used to apply an ac voltage (±0.30 V amplitude, 120 kHz frequency) to one Pt microband. The resulting current passed through solution to a detection microband patterned 30 μm (center-

to-center) downstream, where it was converted back to a voltage through a two-stage transimpedance amplifier. The attenuation of the current passing between the microbands was related to solution conductivity by a calibration curve (Appendix C). Conductivity measurements were obtained using microbands 1 and 2, 7 and 8, 9 and 10, and 15 and 16, as shown in Figure 5.2a. These measurements were carried out at 20 ± 2 °C.

5.3.6 Flow rate measurements

The rate of PDF was determined by optically tracking the motion of fμB along the channel length using an inverted microscope (Eclipse TE2000-U, Nikon, Japan) equipped with a CCD camera (Cascade 512B, Photometrics, Tucson, AZ) and V++ software (DigitalOptics Corporation, San Jose, CA). The data were processed using ImageJ (National Institutes of Health, Bethesda, MD). The experimentally determined flow rates for the NaCl and Na_2SO_4 experiments were 83 ± 7 nL/min (38 replicates) and 90 ± 13 nL/min (10 replicates), respectively.

5.3.7 Numerical simulations

Finite element simulations were carried out using the COMSOL Multiphysics version 5.4 software package. Simulations were performed using a Dell Precision workstation (Model T7500) equipped with two Intel Xeon processors (2.40 GHz) and 24 GB

of RAM. All simulations were performed at steady state. A complete discussion of the theoretical background and details of the numerical simulations is provided in Appendix C.

5.4 Results and discussion

5.4.1 Aqueous Cl_2 chemistry

As discussed in the Introduction, we previously reported forming an IDZ in a device similar to that shown in Illustration 5.1d by electrochemically oxidizing Cl^- to neutral Cl_2 (eq 5.4).[71] Recently, however, we realized that we did not take into account the instability of Cl_2 in aqueous solutions in formulating our conclusions. In this section, we discuss the relevant aqueous Cl_2 chemistry, and in subsequent sections explain the consequences of disregarding it in relation to formation of an IDZ and hence desalination.

In the microelectrochemical system used in the present study (Figure 5.1a), Cl_2 is electrogenerated from Cl^- at the anode. Subsequently, Cl_2 undergoes rapid hydrolysis to yield H^+, Cl^-, and HOCl (eq 5.5).[202,203] HOCl is a weak acid (pK_a = 7.5) and only partially dissociates (eq 5.6). Importantly, the products of these reactions are ionic, and therefore they should serve to counteract formation of the putative IDZ resulting from formation of Cl_2. In the

following sections, we will demonstrate that this is the case.

$$Cl_2 + H_2O \leftrightarrow H^+ + Cl^- + HOCl \quad (5.5)$$

$$HOCl \leftrightarrow H^+ + OCl^- \quad (5.6)$$

5.4.2 Electrochemical potential measurements

Figure 5.1a is a schematic illustration of the microfluidic system used in this study to evaluate the electrical properties of the solution in the vicinity of the anode. Briefly, the system consists of a straight microchannel fabricated from PDMS and attached to a glass slide modified with lithographically patterned Pt microwires. The microchannel is positioned atop the Pt microwires such that the Pt anode extends across the entire channel width. A battery pack is then used to apply a voltage between the anode and cathodes, which are located at the base of the channel reservoirs. In the presence of NaCl, application of a sufficient voltage drives Cl^- oxidation at the anode and water reduction at the cathodes (eqs 5.4 and 5.1, respectively). Oxidation of Cl^- to Cl_2 decreases the concentration of charge carriers near the anode, and we previously reported that this leads to formation of an IDZ and, hence, a local EFG.[71-73]

The electrochemical experiments discussed hereafter were performed in solutions containing 50.0 mM NaCl and 13

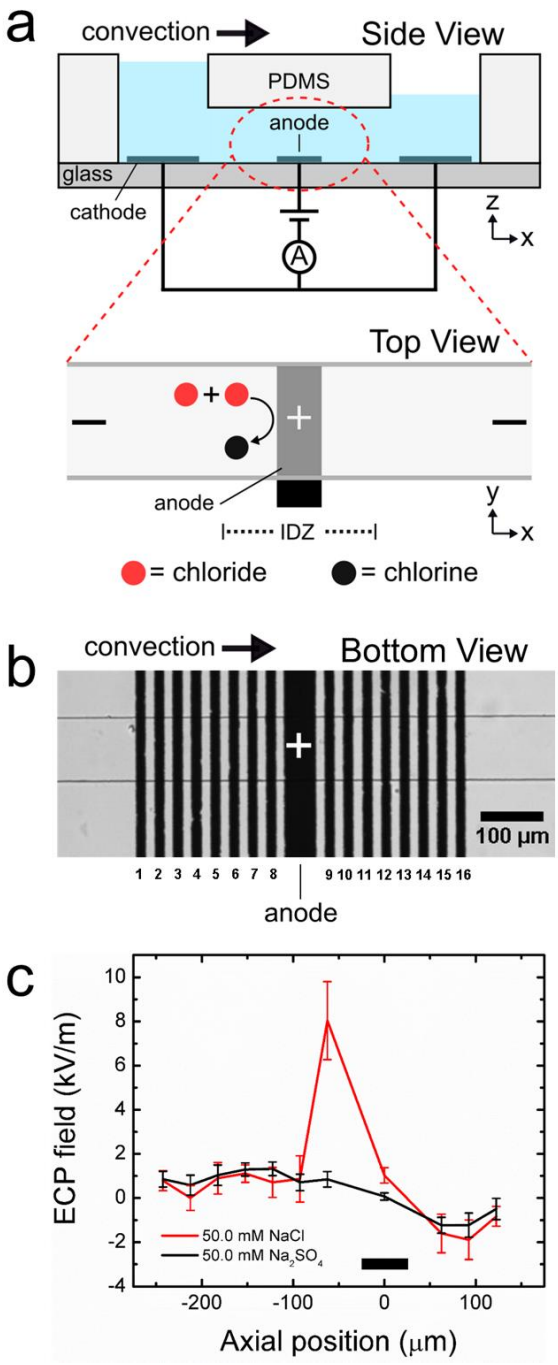

Figure 5.1

(a) Schematic illustration of the microfluidic configuration used for measuring the ECP field. The array of microbands used for mapping the ECP profile have been omitted for clarity. (b) Micrograph of the microfluidic channel

positioned atop the patterned Pt circuitry. The circuitry consists of a central anode microband flanked by an array of measurement microbands (microbands 1-16). (c) Line plot of the steady-state ECP field measured near the anode. The solutions contained either 50.0 mM NaCl or 50.0 mM Na_2SO_4. All solutions also contained 13 fM fμB for measuring the flow rate. The flow rate for experiments performed with 50.0 mM NaCl or 50.0 mM Na_2SO_4 was 83 ± 7 nL/min or 90 ± 13 nL/min, respectively. The applied voltage was 3.0 V. Each data point represents the average of at least nine independent experiments performed using three different microfluidic devices. Figure 5.1: continued.

fM fμB. The composition of the solution is important for three reasons. First, the rate of solution convection can be approximated by optically tracking the motion of fμB within the microfluidic system. Second, the concentration of NaCl is relatively low (compared, for example, to seawater: ~550 mM NaCl), so that a significant fraction of Cl^- can be oxidized to Cl_2 (i.e., a higher percentage of ion depletion) before gas bubbles form within the microfluidic channel and block solution flow (see Appendix C for details).[36,39] Third, the presence of Cl^- in solution suppresses electrochemical water oxidation, which is thermodynamically favored over Cl^- oxidation, due to the presence of an adsorbed layer of Cl^- atop the Pt anode.[206,207] Therefore, in the presence of 50.0 mM NaCl, we conclude that the contribution of water oxidation to the total current passed at the Pt anode is negligible (see Appendix C).

We previously reported that ECP measurements can be used to determine the EFG in and near an IDZ.[39] A

combination of experimental and computational findings validated this methodology.[40,142-144] *Accordingly, we used this approach to characterize the ECP of the solution within the microfluidic channel upon conversion of* Cl^- *to* Cl_2 *at the anode.*

Figure 5.1b is a micrograph of the system used to map the ECP profile near the anode. It consists of an array of Pt microbands patterned across the floor of a microfluidic channel. The central microband is the anode and the narrower microbands flanking the anode are the microbands used to measure the ECP profile. The spatial resolution of this measurement is determined by the center-to-center spacing between neighboring microbands, which in this case is 30 μm.

The ECP profile measurements were performed as follows. A solution containing 50.0 mM NaCl and 13 fM fμB was introduced to the microfluidic channel, and the heights of solution in the two reservoirs were adjusted so that the volumetric flow rate from left to right within the channel was 83 ± 7 nL/min. The flow rate was measured by tracking the speed of fμB. Following initiation of PDF, a scanning digital multimeter, operated in voltage mode, was used to sequentially measure the ECP difference between neighboring pairs of measurement microbands. Next, a battery pack was used to apply 3.0 V between the anode and the cathodes, as

shown in Figure 5.1a. An ammeter connected in series with the battery pack was used to monitor the current passed between the anode and cathodes. Finally, the battery pack was turned off and the ECP profile measurement ended. Three or more measurements were obtained using three independently fabricated microfluidic devices for a minimum of nine replicates. The microfluidic system was then rinsed with DI water and this procedure was repeated with a Cl^--free control solution containing 50.0 mM Na_2SO_4 and 13 fM fμB.

Figure 5.1c is a plot of the ECP field measured near the anode. The data are the averaged signal from 20 ECP measurements performed at steady state for each experiment, and they have been background-subtracted (see Appendix C). The black rectangle at the bottom of the plot indicates the axial position of the anode. Axial position 0 corresponds to the center of the anode, while negative and positive axial positions are upstream and downstream from the anode, respectively.

Application of 3.0 V in the presence of the 50.0 mM NaCl solution results in the formation and maintenance of a gradient in the ECP field near the anode (Figure 5.1c, red line). The most prominent feature is a sharp peak directly upstream of the anode having a magnitude of 8.0 ± 1.8 kV/m. Qualitatively, this result is consistent with previous measurements we have reported under similar conditions,[71]

but there are two significant differences. First, the magnitude of the measured ECP gradient is eightfold larger than previously reported.[71] Second, the position of the peak is just upstream from the anode rather than being directly above it. These differences are due to slight modifications to the experimental configuration in the present case. Note that the magnitude and location of the ECP gradient were optimal at a flow rate of ~85 nL/min. At slower flow rates, the peak broadened and drifted upstream during the measurement. At faster flow rates, little or no gradient was observed near the anode because rapid convection carried away the product of the anodic reaction.

These ECP profile measurements were repeated using a control solution containing 50.0 mM Na_2SO_4 and 13 fM fμB (Figure 5.1c, black). In the absence of Cl^-, application of 3.0 V results in water oxidation, eq 5.3 (recall that the presence of Cl^- prevents this reaction), and this results in formation of an IEZ rather than an IDZ.

In summary, ECP profile measurements indicate selective formation and maintenance of an EFG near the anode only during electrochemical Cl^- oxidation.

5.4.3 Solution conductivity measurements

The oxidation of charged Cl^- to neutral Cl_2 should reduce the conductivity of the solution in the vicinity of the

anode. To test this hypothesis, we carried out conductivity measurements at four different axial positions along the channel length. Figure 5.2a illustrates the microfluidic configuration used to characterize solution conductivity during electrochemical Cl^- oxidation. The system is composed of an array of microbands consisting of a central anode and 16 measurement microbands patterned across the floor of the channel. Measurements were performed using the four pairs of microbands outlined by dashed lines and centered at axial positions -242.5 µm (black), -62.5 µm (red), 62.5 µm (blue), and 242.5 µm (green). As previously mentioned, position 0 corresponds to the center of the anode and negative and positive positions are upstream and downstream from the anode, respectively. Note that the axial position of the pair of microbands outlined by the red dashed line corresponds to the location of the peak ECP gradient shown in Figure 5.1c.

The solution conductivity measurements were made as follows. First, a solution containing 50.0 mM NaCl and 13 fM fµB was pipetted into the microchannel reservoirs, and then the heights of solution in the reservoirs were adjusted until the flow rate was 83 ± 7 nL/min (as confirmed by microbead tracking). Second, the conductivity meter was connected to the pair of microbands outlined by the black dashed line in Figure 5.2a.[137,204] *Third, the initial*

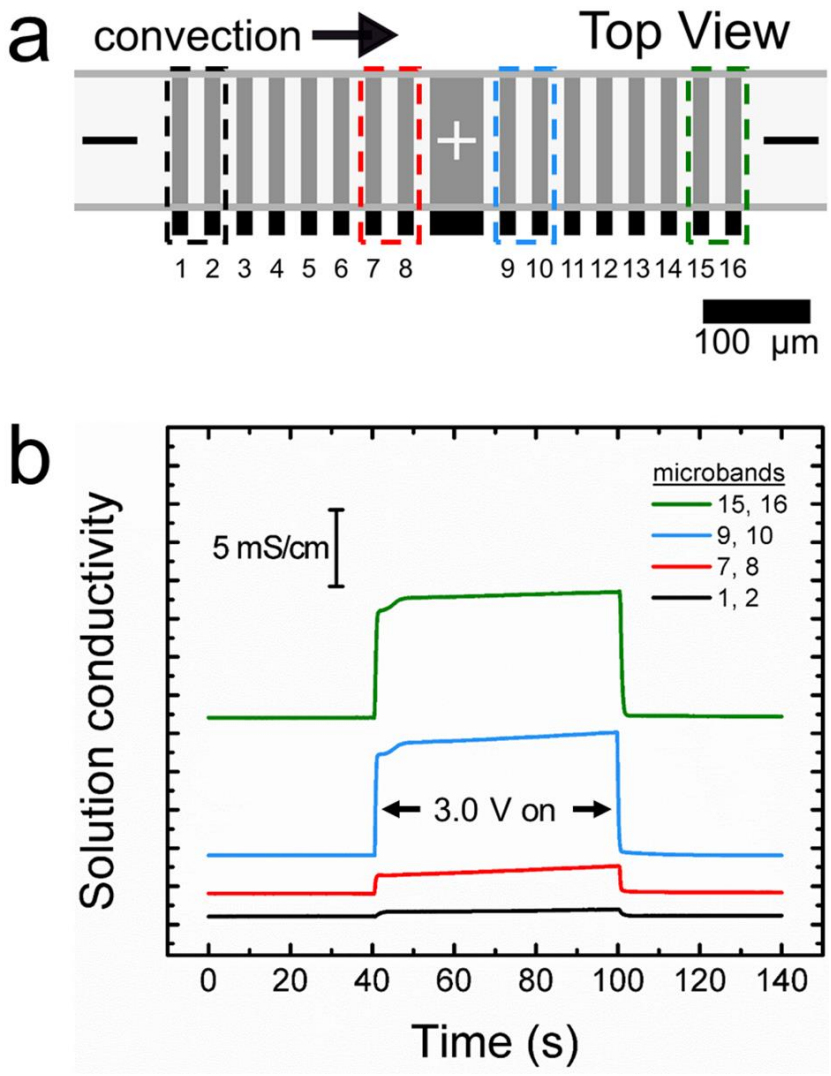

Figure 5.2

(a) Schematic illustration of the microfluidic configuration used for solution conductivity measurements. These measurements were obtained at four different axial positions using the microband pairs outlined by the dashed lines. (b) Representative plot of solution conductivity at four different axial positions as a function of time. The solution contained 50.0 mM NaCl and 13 fM fµB, and the flow rate was 83 ± 7 nL/min. At times 40-100 s, 3.0 V was applied between the anode and the cathodes. At earlier and later times, no voltage was applied. Note that data are offset along the y-axis for clarity. The colors of the dashed lines in (a) correspond to the colors of the lines in (b).

solution conductivity was measured for 40 s. Fourth, the battery pack was used to apply 3.0 V between the anode and the cathodes, and the conductivity was measured for an additional 60 s. Finally, the voltage was turned off, and the conductivity was measured for 40 s. These procedures were repeated using the measurement microbands outlined by the red, blue, and green dashed lines. Two or three replicate measurements were performed at each axial position for each of three independently fabricated microfluidic devices for a total of seven measurements. A calibration curve was then used to convert the voltage output from the conductivity meter to the solution conductivity (Appendix C).

Figure 5.2b is a representative plot of solution conductivity as a function of time at axial channel positions: -242.5 μm (black), -62.5 μm (red), 62.5 μm (blue), and 242.5 μm (green). The key finding is that the application of 3.0 V between the anode and the cathodes leads to an increase in solution conductivity at all positions, but particularly near the anode and also downstream. The average percentage increases in solution conductivity for seven total measurements per microband pair were: microbands 1 and 2: 1 ± 3%; microbands 7 and 8: 29 ± 5%; microbands 9 and 10: 98 ± 27%; and microbands 15 and 16: 100 ± 10%.

The foregoing results were surprising and stand in contrast to the findings of the aforementioned ECP profile measurements, which we interpreted to imply formation of an EFG and IDZ near the anode during electrochemical Cl^- oxidation (Figure 5.1). Specifically, if electrogenerated Cl_2 were stable in solution, a decrease in solution conductivity would be expected close to and downstream from the anode. Therefore, the observed increase indicates that Cl_2 must not be stable in solution. Indeed, this result is consistent with the earlier discussion in the context of eqs 5.5 and 5.6, and it suggests that Cl_2 undergoes a rapid following reaction to yield ionic species which, in turn, leads to an increase in solution conductivity.

Further analysis of Figure 5.2b reveals two additional trends. First, the magnitude of the change in solution conductivity decreases as a function of distance upstream from the anode, but it is nearly constant at axial positions downstream from the anode. This is the expected response because the majority of the ionic products flow downstream from the anode by convection and only a small fraction diffuses upstream. Second, solution conductivity measurements before and after application of 3.0 V are nearly identical. This confirms that an electrochemical process (Cl_2 generation) initiates formation of ions and

that there is no signal drift during the conductivity measurements.

5.4.4 Numerical simulations

We used finite element simulations to provide additional insight into the experimental findings. The simulations were performed at steady state using a two-dimensional (2D) model based on the xz-plane of the microelectrochemical device illustrated in Figure 5.1a.

A complete description of the theoretical background and numerical methods used for the simulations is provided in Appendix C. Briefly, however, solution convection was resolved by the Navier-Stokes equation, and mass transfer was determined by the Nernst-Planck equation and the electroneutrality condition. A previous report describes the absence of an extended space charge region within the microfluidic channel during electrochemical Cl^- oxidation and validates the imposed electroneutrality condition.[73] *The electric field in solution was determined from the steady-state current passed at the anode and the solution conductivity. The electrochemical reaction was modeled as a flux, and the chemical reaction of Cl_2 in solution (eq 5.5) was modeled using reaction rate constants. HOCl dissociation was not included in the model (eq 5.6), because*

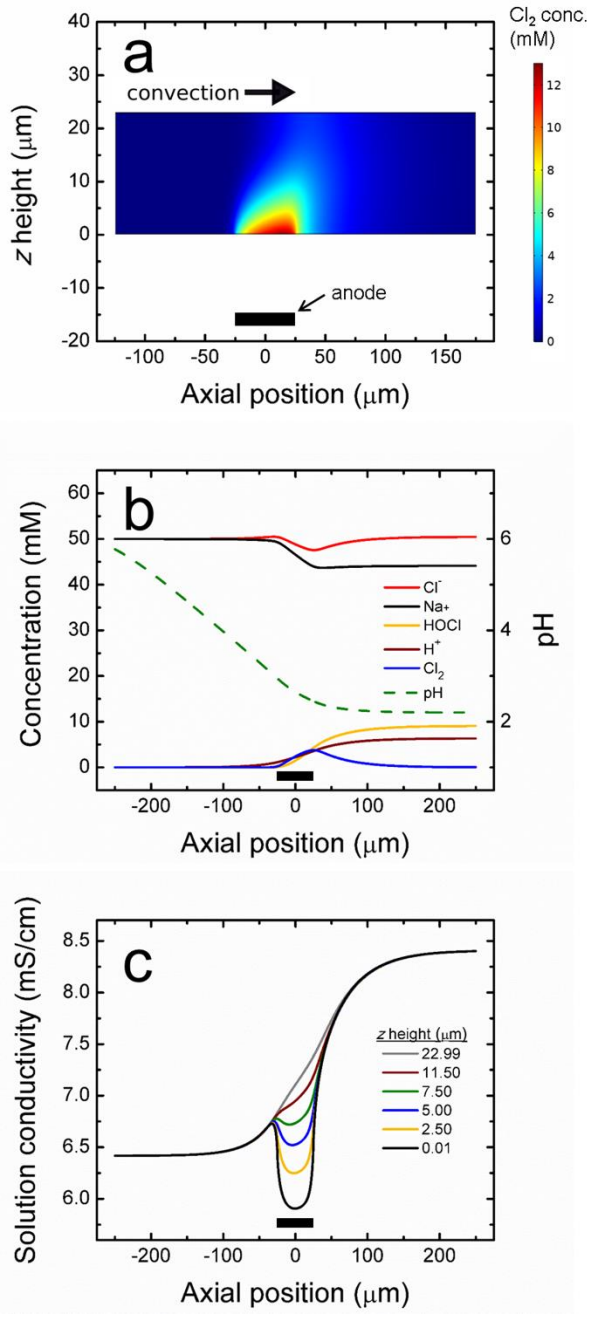

Figure 5.3

Simulation results obtained for a solution containing 50.0 mM NaCl, a flow rate of 83 nL/min, and a current due to Cl^- oxidation of 2.42 μA. (a) Distribution of Cl_2 near the anode. (b) Plot of the simulated concentration of solution species and pH near the anode during electrochemical Cl^-

oxidation. The data shown correspond to z = 11.50 µm (the midpoint of the channel). (c) Plot of the simulated solution conductivity as a function of axial channel position for different z heights. All simulations were performed at steady state with a 2D model based on the xz-plane of the microfluidic system shown in Figure 5.1a. The black rectangle at the bottom of each plot indicates the axial position of the anode. Axial position 0 corresponds to the center of the anode, while negative and positive axial positions are upstream and downstream from the anode, respectively. Figure 5.3: continued.

the pH of the resulting solution was more than two pH units lower than its pK_a.

Figure 5.3a is a planar plot of the simulated distribution of Cl_2 *near the anode. It shows a maximum concentration of* Cl_2 *(~12 mM) directly above the anode (axial positions ±25 µm) and little or no* Cl_2 *elsewhere in the channel. This result confirms that electrochemically generated* Cl_2 *does not persist in solution but instead rapidly reacts to form other species. Figure 5.3b shows line plots of the concentrations of solution species as a function of axial position along the channel length at its central z height (z = 11.50 µm). This plot illustrates that nearly all of the electrochemically generated* Cl_2 *undergoes rapid hydrolysis to form* H^+, Cl^-, *and HOCl. These results confirm that* Cl_2 *is not stable within the microfluidic system but rather rapidly hydrolyzes to form ionic species that counteract IDZ formation. The plot also reveals a decrease in solution pH near the anode. Interestingly, this*

change in pH extends quite far upstream from the anode, which must be a consequence of the very high mobility of H^+.

The conductivity of the simulated solution was also determined by numerical simulation (see Appendix C for details). This makes it possible to directly compare the results of numerical simulations to the experimental solution conductivity measurements. These results are shown in Figure 5.3c, which is a line plot of the simulated solution conductivity as a function of axial position for z heights ranging from z = 0.01 (close to the electrode) to z = 22.99 µm (near the top of the channel). The conductivity at the leftmost axial position is 6.4 mS/cm and corresponds to that of the bulk 50.0 mM NaCl solution. Moving left to right, the solution conductivity gradually increases as the anode is approached. This is due to the presence of highly mobile (and hence conductive) H^+ upstream of the anode, as shown in Figure 5.3b.

The conductivity of the solution in the immediate vicinity of the anode (axial positions ±25 µm) is more complex. At z heights ≤7.50 µm, a non-monotonic trend in solution conductivity is observed. Specifically, oxidation of Cl^- to Cl_2 at the anode reduces the number of ions in solution and decreases solution conductivity near the leading edge of the anode (axial position -25 µm). As discussed earlier, however, electrogenerated Cl_2 is not

stable in solution but reacts to yield ions (eq 5.5). This counteracts the slight IDZ formed by the transient presence of Cl_2 and, ultimately, results in an increase in solution conductivity near the trailing edge of the anode (axial position 25 μm).

Compared with the bulk solution conductivity (6.4 mS/cm), a slight IDZ, corresponding to a ~9% decrease in solution conductivity, occurs directly above the anode (z = 0.01 μm). However, the IDZ does not extend throughout the channel height or beyond the edges of the anode (this is shown most clearly in Figure 5.3a). In addition, the magnitude of ion depletion near the anode is significantly less than previously reported for EFG separations where, compared with the bulk solution, ion concentration decreased by more than 90% within the IDZ.[40,142]

At axial positions near the anode (±25 μm) and z heights >7.50 μm, the solution conductivity is higher than that of bulk solution. This is due to the rapid hydrolysis of Cl_2 to yield H^+ and Cl^-, and then diffusion of these ionic products toward the top of the channel. Finally, at axial positions downstream from the anode (25 to 250 μm), the solution conductivity continues to increase until nearly all of the electrogenerated Cl_2 is consumed by hydrolysis. At axial positions >200 μm, the solution conductivity approaches a limiting value of 8.4 mS/cm. Note that the

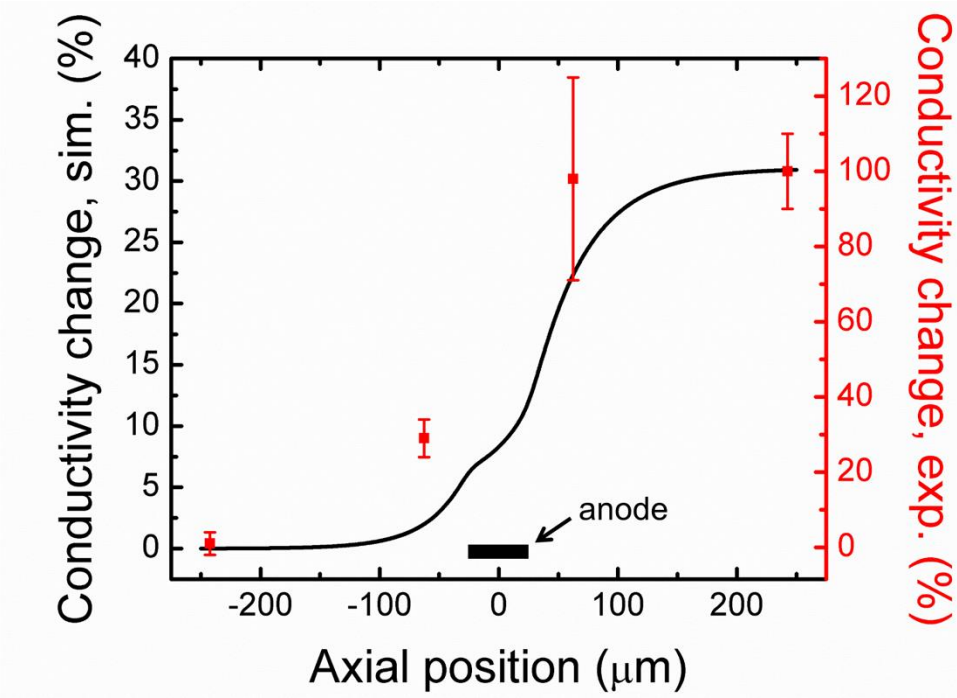

Figure 5.4

Plot of the simulated (black line) and experimentally measured (red points) percentage change in solution conductivity near the anode during electrochemical Cl^- oxidation. The simulated data correspond to z = 11.50 μm (the midpoint of the channel). The left (black) and right (red) vertical axes correspond to the simulated and measured data, respectively.

conductivity of the solution upstream (axial positions -125 to -25 μm) and downstream (axial positions 50 to 175 μm) from the anode is nearly identical at all z heights. This indicates rapid diffusion of solution species throughout the height of the microfluidic channel.

Figure 5.4 is a plot that compares the simulated solution conductivity at the central z height (z = 11.50 μm, black line) to the previously discussed experimental results (red points). Here, we plotted the percentage change from

the bulk solution conductivity as a function of axial position along the channel length. This plot illustrates that there is qualitative agreement between the simulated and experimental results. Specifically, a small increase in solution conductivity occurs directly upstream from the anode during Cl^- oxidation, while a larger increase occurs downstream from the anode. This comparison confirms that Cl^- oxidation followed by rapid Cl_2 hydrolysis increases the conductivity of solution near the anode.

Figure 5.4 also reveals an obvious difference between the magnitudes of the simulated and measured changes in solution conductivity in the vicinity of the anode. For example, at axial position 242.5 μm, the measured change in solution conductivity is about threefold larger than the simulated result (note that the black and red scales are different in Figure 5.4). This is a consequence of a shift in the open circuit potential of the Pt measurement microbands during electrochemical Cl^- oxidation (see Appendix C). A large shift in the open circuit potential of a Pt microband can significantly alter the Pt double-layer capacitance and result in a large discrepancy between the measured and theoretical solution conductivity.[208,209]

Finally, we compared the simulated electric potential field to the previously discussed experimental ECP measurements (Figure 5.1c). Figure 5.5a is a line plot of

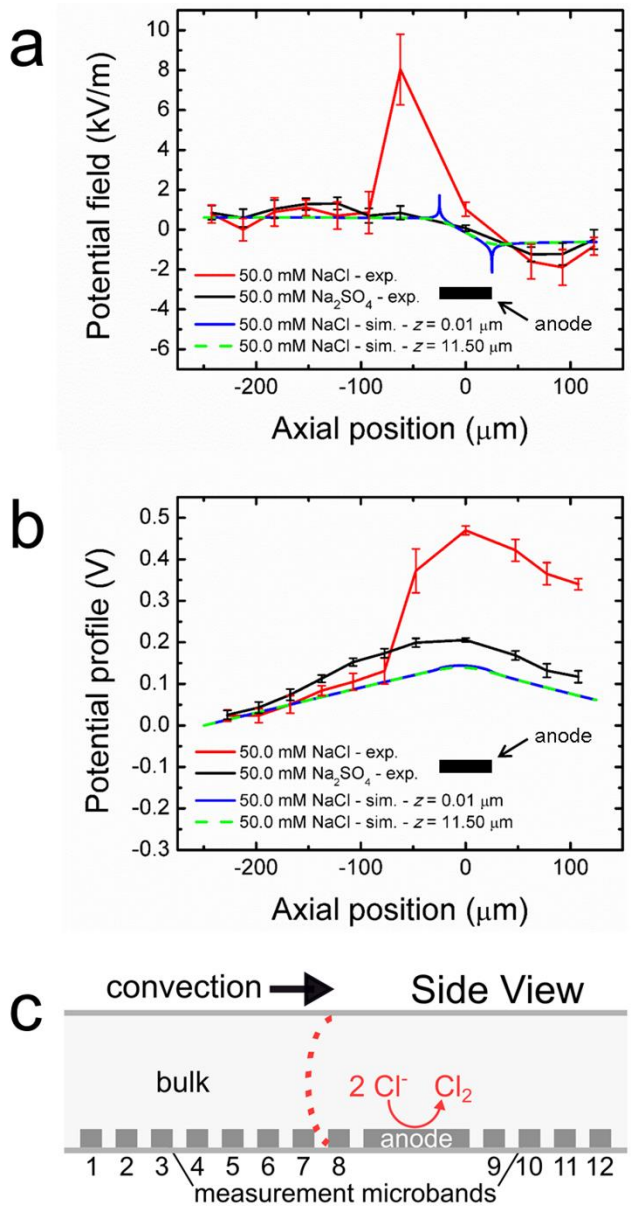

Figure 5.5

(a) Plot of the simulated electric potential field for z = 0.01 and z = 11.50 μm as a function of axial position along the channel length. The experimentally measured ECP field data from Figure 5.1c are overlaid onto the simulations (see legend). (b) Potential profiles used to determine the potential fields shown in (a). (c) Schematic illustration of the microfluidic system showing a difference in the chemical potential of the solution between microbands 7 and 8 (dashed red line) during electrochemical Cl^- oxidation.

the simulated electric potential field as a function of axial position for z = 0.01 and 11.50 µm. These two plots are overlaid with the experimental ECP results. It is important to note that the simulated fields describe only the electric potential of the solution, while the experimental results include both the electric and chemical potentials of the solution. Accordingly, the y-axis is simply labeled as the potential field.

The electric potential field simulated for z = 0.01 µm (blue line) reveals a gradient at the edges of the anode having a peak amplitude of ~2 kV/m. However, there is no gradient in the electric potential field simulated for z = 11.50 µm (dashed green line). These findings are in agreement with the simulated solution conductivity near the anode for z = 0.01 and 11.50 µm (Figure 5.3c) and confirm the absence of a large EFG at distances more than a few microns away from the edges of the anode.

We also plotted the simulated and measured potential profiles used to calculate the results shown in Figure 5.5a (Figure 5.5b). Interpretation of Figure 5.5b is fundamentally similar to that of Figure 5.5a, but it emphasizes the origin of the large ECP gradient measured in the presence of 50.0 mM NaCl solution (red line). As previously mentioned, the simulated potential profiles describe the electric potential of the solution, while the

ECP profiles include both the electric and chemical potential of solution. Therefore, we believe that deviations between the experimentally measured ECP profiles (red and black lines) and the simulated electric potential profiles (blue line and dashed green line) arise from a shift in the chemical potential of the solution in the vicinity of the anode during electrochemical reaction.

Specifically, in the presence of the 50.0 mM Na_2SO_4 solution, water oxidation at the anode forms a concentration gradient of H^+ and O_2 in solution. As the ratio of oxidized to reduced species in solution varies, the chemical potential of solution shifts as predicted by the Nernst equation.[210] In the presence of 50.0 mM NaCl solution, Cl^- oxidation forms a concentration gradient and generates new chemical species (Cl_2, HOCl, etc.) in solution. In this case, more than one redox process can define the chemical potential of the solution and a mixed potential develops.[210-212] Open circuit potential measurements confirm the change in the chemical potential of solution in the vicinity of the anode during electrochemical water or Cl^- oxidation (see Appendix C for details).

Figure 5.5c is a schematic of the microfluidic system illustrating how electrochemical Cl^- oxidation could lead to the measurement of the ECP gradient observed in the presence of 50.0 mM NaCl (Figure 5.5a, red line). Electrochemical

Cl^- oxidation alters the composition (and hence chemical potential) of solution in the vicinity of the anode and downstream of it. Therefore, a boundary forms between the bulk solution (left side of the plot) and the solution just upstream of the anode (dashed red line), which is influenced by processes occurring at the anode. Specifically, the solution near microbands 1-7 is nominally identical, and therefore there is no chemical potential difference between the microbands. This means that the ECP profile measured using microbands 1-7 reflects, principally, the electric field in solution (not the chemical potential). The same explanation holds for microbands 8-12. However, microbands 7 and 8 interact with solutions containing different chemical species, and therefore a mixed potential develops between them (dashed red line in Figure 5.5c). Accordingly, the ECP measured between microbands 7 and 8 includes both the electric and chemical potential of the solution in this region of the microchannel.

5.5 SUMMARY AND CONCLUSIONS

We previously reported that electrochemical oxidation of Cl^- to neutral Cl_2 results in an IDZ and EFG that could be used for desalination. These conclusions were founded on our interpretation of two experimental results. First, experiments intended to measure the electric potential

profile in solution revealed a local potential gradient near the anode during Cl^- oxidation. Second, fluorescence measurements performed when the salt solution contained a charged fluorophore as an ionic tracer revealed a decrease in fluorescence intensity in the desalted channel during desalination experiments.

Here, however, we have presented experimental and computational results showing that the previously reported electrochemical and chemical processes are more complex and subtle than we originally realized. Specifically, there are two key findings from this work. First, once generated, Cl_2 rapidly reacts in water to produce H^+, Cl^-, and HOCl, and this results in formation of an IEZ rather than an IDZ near the anode. Second, the ECP gradient measured during electrochemical Cl^- oxidation is caused by a shift in the chemical potential, rather than the electric potential, of the solution in the vicinity of the anode. It is now apparent that the previously reported decrease in fluorescence intensity during Cl^- oxidation was likely due to fluorescence quenching and not to desalination.[213]

We conclude that electrochemical Cl^- oxidation does not form a significant IDZ or EFG in solution that can be used for saltwater desalination. Furthermore, these findings demonstrate that undesired (or unknown) electrochemical and chemical processes can prevent formation of an IDZ and EFG

in other electrochemical systems. To address this issue, we are currently developing a new approach to form an IDZ in solution that utilizes ion insertion processes. We will report the results of these experiments in due course.

Chapter Six: Conclusions and Outlook

This dissertation reports recent advancements toward continuous chemical separations by faradaic ion concentration polarization (fICP) in microelectrochemical devices. In fICP experiments, electrochemical processes yield ion depletion zones (IDZs) and associated electric field gradients (EFGs) useful for controlling the motion of charged objects in solution. In the studies presented in Chapters 3 and 4, fICP results from electrochemical water splitting and Tris buffer chemistry. By tuning the rate of solution convection as well as the magnitude, shape, and number of EFGs in a single microfluidic channel, we demonstrate that fICP enables the complete and continuous separation of up to two charged objects having different properties. Accordingly, these studies improve our understanding of the processes fundamental to directing the flow of charged objects by fICP.

In an effort to expand fICP to Tris-free solutions, such as seawater, we also investigated the formation of IDZs by electrochemical oxidation of Cl^- to neutral Cl_2. The results of this study are presented in Chapter 5. The key finding is that electrochemical Cl^- oxidation does not yield an IDZ in solution. Rather, Cl_2 rapidly reacts in water to form ionic species that produce an ion enrichment zone (IEZ). This finding demonstrates that unintended

electrochemical and chemical processes can prevent the formation of IDZs and their associated EFGs in microelectrochemical devices.

Based on the findings reported in this dissertation, we conclude that fICP is a viable strategy to continuously direct the flow of charged objects in microfluidic channels. However, it is also apparent that the formation of IDZs by the oxidation or reduction of solution species in buffer-free solutions is limited by undesired (or unknown) electrochemical and chemical processes. Therefore, the successful application of fICP to important chemical separations relies on developing new electrochemical approaches to form IDZs and their associated EFGs in the solutions of interest.

To this end, we recently began to explore the formation of IDZs by ion insertion processes at conventional battery materials. Compared to the oxidation or reduction of solution species, we think that there are four important advantages of using ion insertion processes to form IDZs. First, ion insertion is associated with a distinct redox potential and lattice geometry, enabling precise control of insertion processes and high selectivity for ion insertion. Second, ion insertion depends on the redox processes of the insertion material and not solution species, and thus reduces or eliminates undesired electrochemical and chemical

processes. Third, electrochemically inactive species (K^+, Na^+, Ca^{2+}, etc.) can be targeted to form an IDZ. Fourth, insertion processes yield IDZs, which are useful for EFG-based separations, but they also lead to energy stored in the electrochemical potential of the ion-inserting electrodes. This energy can subsequently be recovered, thereby reducing the net energy required for separations. For these reasons, our group is actively investigating fICP at ion insertion materials. The results from these experiments are not discussed in this dissertation and will be reported in due course.

At this moment, it is too early to predict the impact of fICP on the many important chemical separations performed daily on an industrial scale. However, it is increasingly evident that the development of energy-efficient techniques for chemical separations is essential to a sustainable and prosperous future. Accordingly, herein we present the results of three fundamental studies that open up the possibility to investigate the energy efficiency of fICP. Finally, we believe that the results from these studies represent a significant contribution to the growing and promising field of electrochemical separations—a field that has the potential to redefine the landscape of chemical separations.

Appendices

APPENDIX A

A.1 Conductivity calibration curves for Tris buffer

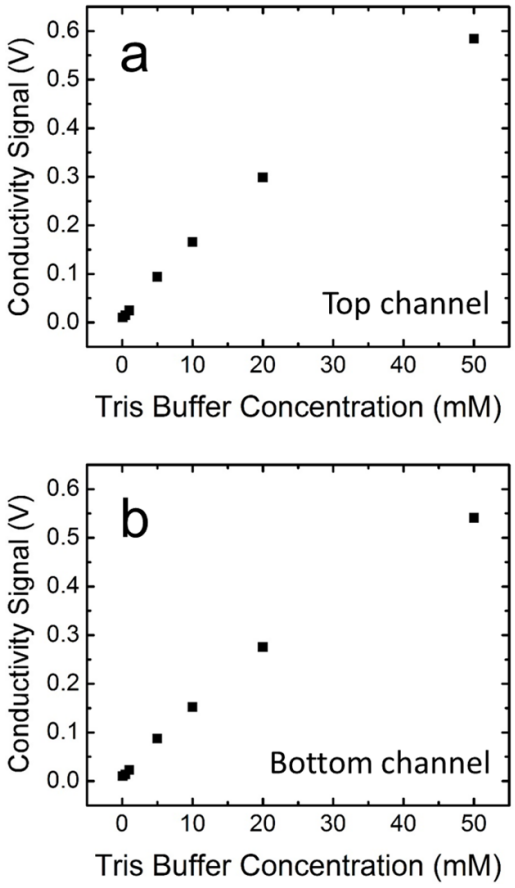

Figure A.1

Calibration curves for Tris buffer solutions (pH = 8.1) with the Pt conductivity bands in (a) the top channel of a bifurcated channel and (b) the bottom channel. These measurements were performed as follows. Tris buffer of the indicated concentrations was placed in the channel reservoirs, and then conductivity measurements were collected in the top channel (Figure 3.3a). The channel was then rinsed three times with deionized water (DI water), filled with the next higher concentration of Tris buffer, and another set of conductivity measurements made. These procedures were repeated using the conductivity bands in the bottom channel.

A.2 Measurements of i_{BPE} and i_{tot} during fICP

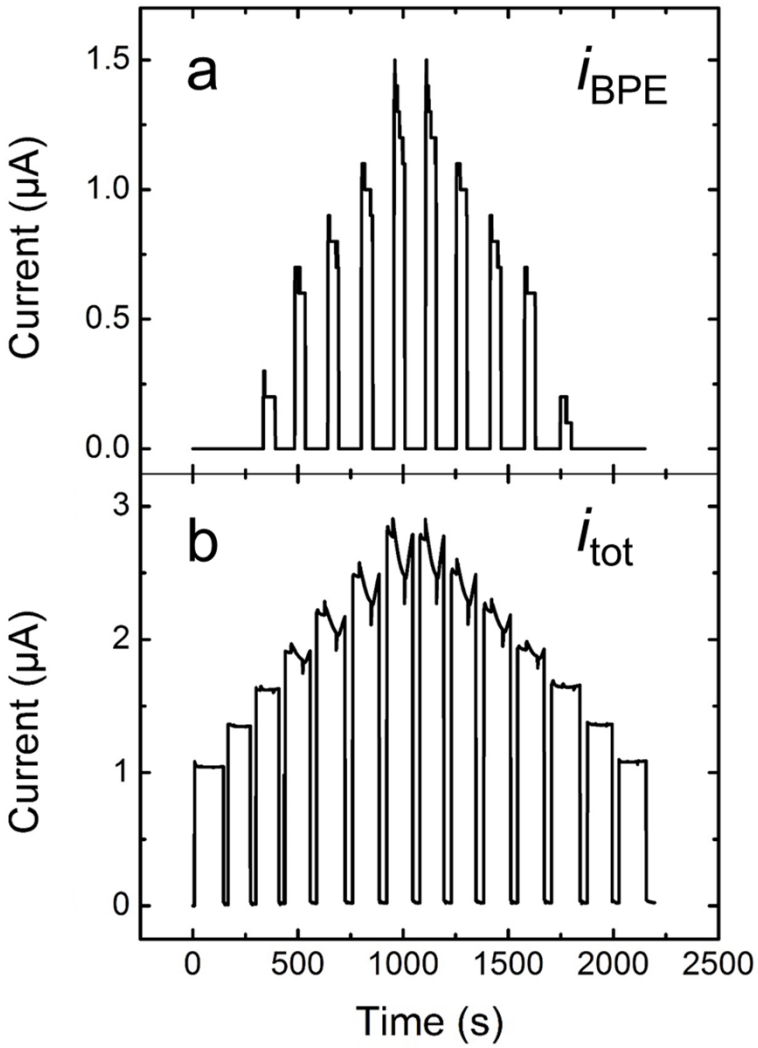

Figure A.2

Simultaneous current measurements for (a) i_{BPE} (the current passed through the bipolar electrode, BPE) and (b) i_{tot} (the total current passed through the driving electrodes). The experiment was performed as follows. First, equal heights of solution containing 3.0 pM μB and 10.0 mM Tris buffer (pH 8.1) were placed in the reservoirs of a straight microchannel, resulting in zero pressure-driven flow (PDF). Second, i_{BPE} and i_{tot} were measured simultaneously. Third, a driving voltage (E_{tot} = 20.0 V) was applied across the channel length, resulting in electroosmotic flow (EOF) toward the negative driving electrode. Fourth, two

microbands were connected to form a 580 µm-long BPE and resulted in faradaic ion concentration polarization (fICP). Fifth, the microbands comprising the BPE were disconnected, which stopped fICP. Finally, these procedures were repeated with E_{tot} increasing by 5.0 V per run (E_{tot} = 20.0, 25.0, 30.0, 35.0, 40.0, 45.0, 50.0 V; 0-1050 s). These procedures were repeated with E_{tot} decreasing by 5.0 V per run starting at 50.0 V (E_{tot} = 50.0, 45.0, 40.0, 35.0, 30.0, 25.0, 20.0 V; 1050-2200 s). i_{BPE} and i_{tot} were measured using ammeters placed in series with the respective circuits.[36] Data from a bench-top multimeter (2700 Series, Keithley) were recorded using LabVIEW software (National Instruments, Austin, TX) and data from a hand-held multimeter (VA 18B) were recorded using PC-Link software.

Buffer neutralization at the BPE cathode results in formation of an ion depletion zone (IDZ). This region of increased solution resistance alters the linear electric field along the channel length. At E_{tot} = 35.0-50.0 V, a decrease in i_{tot} is observed when faradaic processes occur at the BPE. We believe that formation of an IDZ increases the total channel resistance, resulting in a non-uniform electric field gradient (EFG). This may lead to a decrease in the magnitude of the potential difference between the ends of the BPE and solution (ΔE_{elec}) during IDZ formation. Figure A.2: continued.

A.3 Description for movies

A.3.1 Movie A.1

Movie A.1 shows the manipulation of non-fluorescent polystyrene microbeads (μB) during fICP using Tris buffer (from Tris-HCl) in a straight channel. Movie A.1 was collected as follows. First, equal heights of solution containing 3.0 pM μB and 10.0 mM Tris (pH = 8.1) were added to each reservoir resulting in zero PDF. Second, the video begins with solution moving right to left in the channel by EOF ($Æ_{tot}$ = 30.0 V). Third, the microbands comprising the BPE shown in Figure 3.2a were connected and fICP commenced. Fourth, the field of view moves downstream of the BPE before returning to the original field of view. Finally, the BPE microbands were disconnected, fICP stopped, and the microbead flow rate returned to its original value.

A.3.2 Movie A.2

Movie A.2 shows the manipulation of fluorescent polystyrene microbeads (fμB) during fICP using Tris buffer (from Tris-HCl) in a bifurcated channel. Movie A.2 was collected as follows. First, equal heights of solution containing 56 fM fμB and 10.0 mM Tris buffer (pH = 8.1) were added to each reservoir resulting in zero PDF. Second, the video begins with solution moving right to left in the channel by EOF ($Æ_{tot}$ = 35.0 V). Third, the microbands comprising the red

BPE configuration (Figure 3.3a) were connected and fICP commenced. Fourth, the microbands comprising the BPE were disconnected and the microbead flow rate returned to its original value. Fifth, the microbands comprising the green BPE configuration (Figure 3.3a) were connected and fICP began again.

A.3.3 Movie A.3

Movie A.3 shows the motion of µB during fICP using Tris buffer derived from Tris-H_2SO_4 in a bifurcated channel. Movie A.3 was collected as follows. First, equal heights of solution containing 3.0 pM µB and 10.0 mM Tris-H_2SO_4 (pH = 8.0) were added to each reservoir resulting in zero PDF. Second, the video begins with solution moving right to left in the channel by EOF with E_{tot} = 35.0 V. Third, the microbands comprising the red BPE configuration (Figure 3.3a) were connected and fICP commenced. Fourth, the microbands comprising the BPE were disconnected and solution flow returned to its original value. Fifth, the microbands comprising the green BPE configuration (Figure 3.3a) were connected and fICP began again.

In previous experiments, we have shown that oxidation of Cl^- at the BPE anode contributes to formation of the IDZ.[71,72] To test the importance of Cl^- in the present case, the buffer obtained from Tris-HCl was replaced with Cl^--free

Tris-H_2SO_4. The results for the two buffers were the same, indicating that Cl^- does not play an important role in the experiments reported here.

APPENDIX B

B.1 Solution conductivity calibration curve

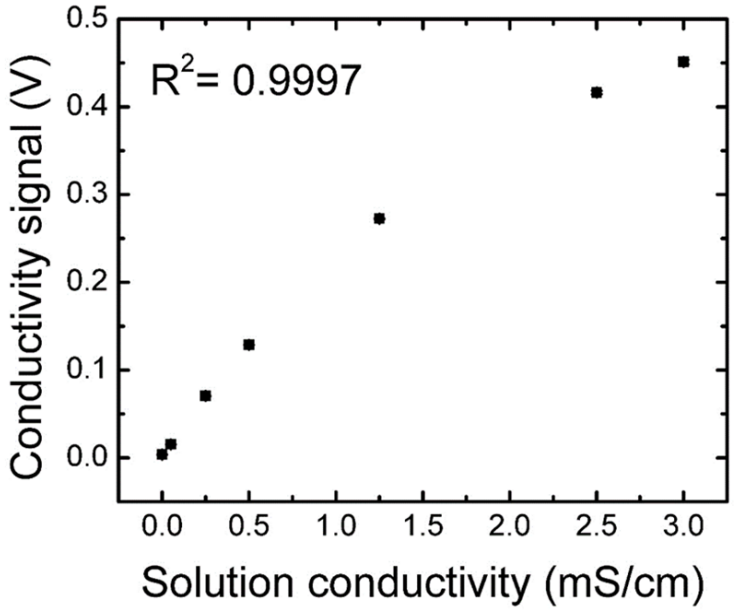

Figure B.1

Calibration curve used to correlate the measured conductivity signal (V) to solution conductivity (mS/cm). This is a representative calibration curve that was obtained using the conductivity microbands located in the top outlet channel (Figure 4.3a). Similar calibration curves were obtained for the conductivity microbands located in the middle and bottom outlet channels. The calibration curves were generated as follows. First, solutions having the following conductivities were prepared from conductivity standard solutions: 0.05, 0.25, 0.50, 1.25, 2.50, and 3.00 mS/cm (NaCl conductivity standards, RICCA Chemical Company, Arlington, TX). Second, the solutions were flowed through the microfluidic channel by pressure-driven flow (PDF). Third, solution conductivity measurements were performed. Each data point represents the average of 100 measurements. The y error bars are smaller than the data points and thus are not apparent. The calibration curves deviate from linearity at high conductivities due to changes in the capacitance of the micron-scale Pt microbands.[208] Accordingly, the data were fit with second-order polynomial regressions. The average of the coefficients of determination (R^2) for the calibration curves is 0.9996 ± 0.0003 (six replicates).

B.2 Electrophoretic mobility measurements

The electrophoretic mobilities of μP1, μP2, and μP3 were quantified by dynamic light scattering as follows. First, microplastic solutions were prepared by 100-fold dilution of the microplastic stock solutions in 10.0 mM Tris-HCl (pH 8.1). Second, the solutions were placed into a disposable folded capillary cell (Malvern Instruments, UK). Third, the cell was inserted into a Zetasizer Nano ZS (Malvern Instruments) and the electrophoretic mobility of the microplastics was measured. The reported electrophoretic mobility for each microplastic is the average of three measurements.

B.3 Numerical simulations

Finite element simulations were carried out using the COMSOL Multiphysics version 5.4 software package. Simulations were performed using a Dell Precision workstation (Model T7500) equipped with two Intel Xeon processors (2.40 GHz) and 108 GB of RAM. All simulations were performed at steady state.

Simulations were performed using a two-dimensional (2D) model based on the xy-plane of the microfluidic system shown in Figure 4.2a. The main channel was 200.0 μm wide and each outlet channel was 66.7 μm wide. The middle and top outlet channels were orientated at angles of 30° and 60°, respectively, from the bottom outlet channel. The bipolar

electrode (BPE) poles were 50.0 µm wide and located flush with the channel sidewalls. To capture the impact of serial faradaic ion concentration polarization (fICP) on the distribution of solution species within the channel, we modeled 250.0 µm upstream of the leading edge of BPE1 and 250.0 µm downstream of the trailing edge of BPE2. The length of BPE1 was 750.0 µm, the length of BPE2 was 1000.0 µm, and the gap between the BPEs was 710.0 µm. Accordingly, the length of the channel modeled was 2960.0 µm (250.0 µm + 1000.0 µm + 710.0 µm + 750.0 µm + 250.0 µm). The modeling domain is shown in Figure 4.4a.

Solution convection within the 2D model was simulated using the "Creeping Flow" interface in COMSOL Multiphysics. This interface solves the Navier-Stokes equation for incompressible flow of a viscous fluid (eqs B.1 and B.2).

$$\rho(u \cdot \nabla)u = \nabla \cdot [-pI + \mu(\nabla u + (\nabla u)^T)] + f_v \qquad (B.1)$$

$$\rho \nabla \times u = 0 \qquad (B.2)$$

Here, ρ is the density of the solution, u is the velocity vector of the solution, μ is its dynamic viscosity, p is pressure, I is the identity matrix, T is temperature, and f_v is the volume force vector.

The right boundary of the model was taken to be the inlet and the left ends of the three secondary channels were taken to be the outlets. The inlet and outlets were modeled as pressure boundaries (p = 0) and the channel sidewalls

(remaining boundaries) were modeled as an electroosmotic velocity formulated according to the Helmholtz-Smoluchowski equation and calculated using the simulated local electric field. The zeta potential of the channel sidewalls was taken to be -50 mV.[35]

Mass transport within the model was simulated with the "Nernst-Planck" interface. This interface solves the Nernst-Planck equation with the electroneutrality condition to simulate the flux of species by convection, diffusion, and electromigration (eqs B.3-B.7).

$$\nabla \cdot J_i + u \cdot \nabla c_i = R_i \qquad (B.3)$$

$$\nabla \cdot i = F \sum_i z_i R_i \qquad (B.4)$$

$$\sum_i z_i c_i = 0 \qquad (B.5)$$

$$J_i = -D_i \nabla c_i - z_i \mu_{ep,i} F c_i \nabla \varphi \qquad (B.6)$$

$$i = F \sum_i z_i (-D_i \nabla c_i - z_i \mu_{ep,i} F c_i \nabla \varphi) \qquad (B.7)$$

Here, J_i is flux, c_i is concentration, R_i is the rate of reaction, z_i is the charge, D_i is the diffusion coefficient, and $\mu_{ep,i}$ is the electrophoretic mobility, all for species i. F is the Faraday. φ is the electric potential. The inlet was taken to have an inflow of 10.0 mM Tris-HCl buffer at pH 8.1. The concentrations of $TrisH^+$, Tris, and Cl^- were determined from the pKa of Tris buffer at 20 °C (pKa = 8.24, calculated using the Debye-Hückel model).[214,215] *The concentrations of H^+ and OH^- were determined from the pH.*

The inlet was taken to have a steady-state current density of 573.91 A/m^2 (1.32 µA / (11.5 µm · 200.0 µm)) and the potential of the outlet boundaries was 0 V. The poles of BPE1 and BPE2 were taken to have current densities of 266.67 A/m^2 (0.60 µA / (45.0 µm · 50.0 µm)) and 328.89 A/m^2 (0.74 µA / (45.0 µm · 50.0 µm)), respectively. The value of the current densities at the cathodic poles of the BPEs was negative and the value of the current densities at the anodic poles of the BPEs was positive. The local current density across each BPE pole was assumed to be governed by a linear dependence on the axial position.[40] Specifically, the current density was 0 at the interior edge of each pole (x = 300, 1200, 2010, and 2660 µm) and had a maxima at the exterior edge of each pole (x = 250, 1250, 1960, and 2710 µm). Water electrolysis (eqs 4.1 and 4.3) was modeled by fluxes at the poles of the BPEs and proceeded with 100% faradaic efficiency.[35] The production of H_2 and O_2 by water reduction and oxidation, respectively, was not accounted for in the model.

Following electrochemical water electrolysis, Tris buffer chemistry was simulated (eqs 4.2 and 4.4). TrisH$^+$ neutralization (i.e., Tris formation) was simulated using a reaction rate equation (eq B.8).

$$R_{Tris} = -\left(k_{f,neut} c_{Tris}\right) + \left(k_{b,neut} c_{TrisH^+} c_{OH^-}\right) + \left(k_{f,neut} c_{TrisH^+}\right) - \left(k_{b,neut} c_{Tris} c_{H^+}\right) \quad (B.8)$$

Here, R_{Tris} is the rate of Tris formation. The previously reported reaction rate constants for Tris buffer neutralization were assumed to also describe Tris buffer reionization.[35] Accordingly, $k_{f,neut}$ and $k_{b,neut}$ are the forward and backward reaction rate constants, respectively, for both Tris buffer neutralization and reionization. Therefore, $R_{Tris} = -R_{TrisH^+}$.

The effect of Tris buffer chemistry on H^+ was simulated using a second reaction rate equation (eq B.9).

$$R_{H^+} = \left(k_{f,hydro} c_{H_2O}\right) - \left(k_{b,hydro} c_{H^+} c_{OH^-}\right) + \left(k_{f,neut} c_{TrisH^+}\right) - \left(k_{b,neut} c_{Tris} c_{H^+}\right) \quad (B.9)$$

Here, R_{H^+} is the rate of H^+ formation and $k_{f,hydro}$ and $k_{b,hydro}$ are the forward and backward reaction rate constants, respectively, for water self-ionization.[35] The concentration of water (55.5 M) was taken to be constant throughout the modeling domain.

The effect of Tris buffer chemistry on OH^- was simulated using a third reaction rate equation (eq B.10).

$$R_{OH^-} = \left(k_{f,hydro} c_{H_2O}\right) - \left(k_{b,hydro} c_{H^+} c_{OH^-}\right) + \left(k_{f,neut} c_{Tris}\right) - \left(k_{b,neut} c_{TrisH^+} c_{OH^-}\right) \quad (B.10)$$

Here, R_{OH^-} is the rate of OH^- formation.

Solution conductivity (κ) was calculated from the simulated distribution of solution species using eq B.11.

$$\kappa = \sum_i c_i \mu_{ep,i} (z_i F)^2 \quad (B.11)$$

A user-controlled mesh was used to solve the multiphysics model. A relaxed mesh (maximum element size = 6.92 µm, minimum element size = 0.0207 µm) optimized for fluid dynamics was used throughout the majority of the modeled domain, while a more dense mesh (maximum element size = 1.50 µm, minimum element size = 0.0207 µm) was employed near the BPE poles to enable accurate modeling of water electrolysis and the rapid Tris buffer chemistry. The quality of the mesh was confirmed by a mesh refinement study.

A parametric sweep of the magnitude of the currents passed through the BPEs was used to solve the model. The model was solved iteratively from $i_{BPE1} = i_{BPE2} = 0$ *µA to* $i_{BPE1} = 0.60$ *µA and* $i_{BPE2} = 0.74$ *µA using a current step of 0.01 µA. The solution for each iteration was used to define the initial conditions for the next iteration.*

Complete details for the parameters, geometry dimensions, and interface settings are available within the accompanying COMSOL Multiphysics report (COMSOL Report 1).

B.4 Normalized conductivity with BPE1 "on"

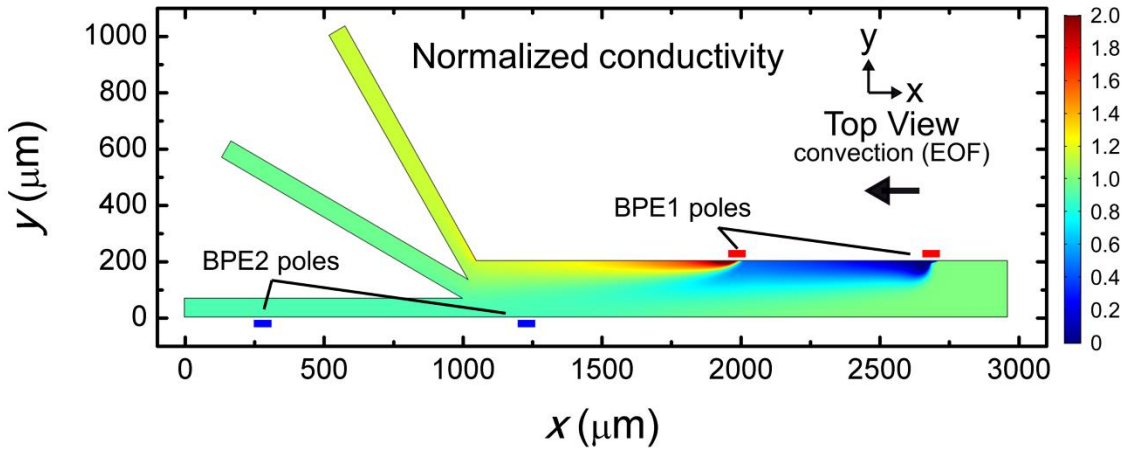

Figure B.2

Steady-state simulation results for a solution containing 10.0 mM Tris buffer (pH 8.1), and with i_{tot} = 1.32 μA and i_{BPE1} = 0.60 μA. Plot of solution conductivity throughout the channel. Conductivity values are normalized to the conductivity of bulk solution. The range of the color scale bar is truncated for emphasis. The red and blue rectangles indicate the position of the poles of BPE1 and BPE2, respectively.

B.5 Tris concentration with BPE1 and BPE2 "on"

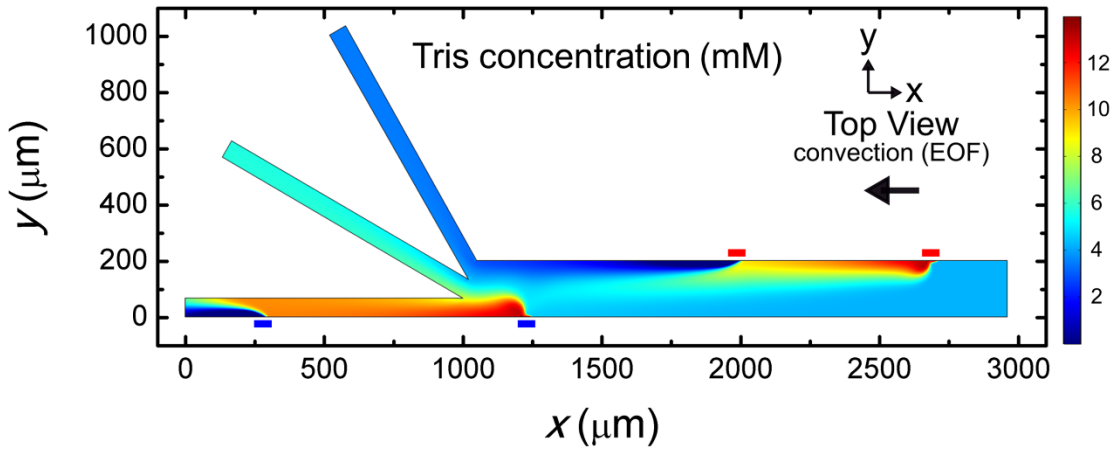

Figure B.3

Steady-state simulation results for a solution containing 10.0 mM Tris buffer (pH 8.1), and with i_{tot} = 1.32 μA, i_{BPE1} = 0.60 μA, and i_{BPE2} = 0.74 μA. Distribution of Tris along the channel length. The red and blue rectangles indicate the position of the poles of BPE1 and BPE2, respectively. The BPE poles in the 2D model are positioned flush with the channel sidewalls. Accordingly, the majority of $TrisH^+$ neutralized near the cathodic pole of BPE2 does not diffuse beyond y = 67 μm and enter the middle outlet channel. Thus, most Tris formed near the cathodic pole of BPE2 flows downstream and enters the bottom outlet channel. Here, it is reionized by H^+ generation at the anodic edge of BPE2.

B.6 Simulated rate of convection

The simulated result shown in Figure 4.4d is consistent with the following explanation. Connecting the microbands that comprise BPE1 with a jumper wire shunts ~46% of i_{tot} through BPE1 (i_{BPE1}) and forms an ion depletion zone (IDZ) and ion enrichment zone (IEZ) in solution by fICP (shown most clearly in Figure 4.3b and Figure 4.4c). The resulting electric field gradient near the leading edge of the cathodic pole of BPE1 (x = 2710-2800 µm) increases the local rate of convection by electroosmotic flow (EOF) and, because the solution is incompressible, creates a pressure gradient along the channel length. This produces a PDF from right to left, as shown by the parabolic flow profile at x = 2900 µm.

Shunting a large percentage of i_{tot} through BPE1 decreases the magnitude of the current passed in solution between the poles of BPE1.[35,36] Therefore, solution flow in this region of the channel (x = 2100-2500 µm) is controlled by relatively weak EOF and pressure gradients. The current through BPE1 is converted to ionic current at the anodic pole of BPE1. The presence of an IEZ along the upper sidewall downstream of BPE1 (Figure 4.4c) leads to a weak electric field in solution and a corresponding slow flow rate along the upper sidewall (x = 1500-1960 µm). Therefore, the majority of solution continues downstream

through a restricted region of the channel width (y = 30-150 μm) at an elevated flow rate.

The explanation for the observed rates of convection near the cathodic pole of BPE2 (x = 1000-1250 μm) is similar to that provided for convection near the cathodic pole of BPE1. However, in this case, the presence of the channel trifurcation increases the complexity of flow in this region. Although ~56% of i'_{tot} passes through BPE2 (i'_{BPE2}), the majority of the remaining ~44% passes to the negative driving electrodes located in the outlet reservoirs through the top and middle outlet channels. Because the magnitude of current is inversely proportional to solution resistance, the current density, and thus the rate of EOF, at the entrances to the top and middle outlet channels is largest along the upper sidewalls of each channel (y = 200 μm and 133 μm, respectively). However, downstream from the entrances to the top and middle outlet channels, the conductivities of the solutions (see Figure 4.4c), and thus the rates of EOF, are nearly uniform across the channel widths.

The rate of convection in the bottom outlet channel is influenced by the presence of BPE2. Specifically, shunting a large portion of i'_{tot} through BPE2 decreases the magnitude of the current passed in solution between the poles of BPE2. Therefore, solution flow in this region of the bottom outlet

channel (x = 300-1000 µm) is controlled by relatively weak EOF and pressure gradients. However, the return of i_{BPE2} to solution at the anodic end of BPE2 results in an increase in the rate of convection downstream (x = 0-250 µm), despite the presence of an IEZ in solution. This is due to the elevated current density in this portion of the microchannel.

B.7 Description for Movies

B.7.1 Movie B.1

Movie B.1 shows the manipulation of $BODIPY^{2-}$ and µP1 during a fICP experiment using Tris buffer in a trifurcated channel. Movie B.1 was collected as follows. First, equal heights of solution containing 1.0 µM $BODIPY^{2-}$, 1.5 pM µP1, and 10.0 mM Tris buffer (pH 8.1) were added to each reservoir resulting in zero PDF. Second, the video begins with solution moving right to left in the channel by EOF (driving voltage = 25.0 V). Third, the microbands comprising the BPE (Illustration 4.2b) were connected and fICP commenced. Finally, the BPE microbands were disconnected, fICP stopped, and the microplastic flow rate returned to its original value.

B.7.2 Movie B.2

Movie B.2 shows the manipulation of $BODIPY^{2-}$ and µP1 during a serial fICP experiment using Tris buffer in a trifurcated channel. Movie B.2 was collected as follows. First, equal heights of solution containing 1.0 µM $BODIPY^{2-}$, 1.5 pM µP1, and 10.0 mM Tris buffer (pH 8.1) were added to each reservoir resulting in zero PDF. Second, the video begins with solution moving right to left in the channel by EOF (driving voltage = 25.0 V). Third, the microbands comprising BPE1 (Figure 4.2a) were connected and fICP commenced. Fourth, the field of view moved upstream from the channel trifurcation to the anodic pole of BPE1, then to the cathodic pole of BPE1, and then back to the channel trifurcation. Fifth, the microbands comprising BPE2 (Figure 4.2a) were connected and serial fICP commenced. Finally, the microbands comprising the two BPEs were disconnected, serial fICP stopped, and the microplastic flow rate returned to its original value.

B.7.3 Movie B.3

Movie B.3 shows the manipulation of µP2 and µP3 during a serial fICP experiment using Tris buffer in a trifurcated channel. Movie B.3 was collected as follows. First, different heights of solution containing 150 fM µP2, 190 pM µP3, and 10.0 mM Tris buffer (pH 8.1) were added to the

inlet and outlet reservoirs resulting in PDF from right to left (32 ± 3 nL/min, seven replicates). Second, the video begins with solution moving right to left in the channel by PDF. Third, the driving voltage (25.0 V) was applied across the channel length resulting in EOF from right to left. Fourth, the microbands comprising BPE2 (Figure 4.2a) were connected and fICP commenced. Fifth, the microbands comprising BPE1 (Figure 4.2a) were connected and serial fICP commenced. Sixth, the field of view moved upstream from the channel trifurcation to the cathodic pole of BPE1, then to the anodic pole of BPE1, and then back to the channel trifurcation. Finally, the microbands comprising the two BPEs were disconnected, serial fICP stopped, and the microplastic flow rate returned to its original value.

APPENDIX C

C.1 Solution conductivity calibration curve

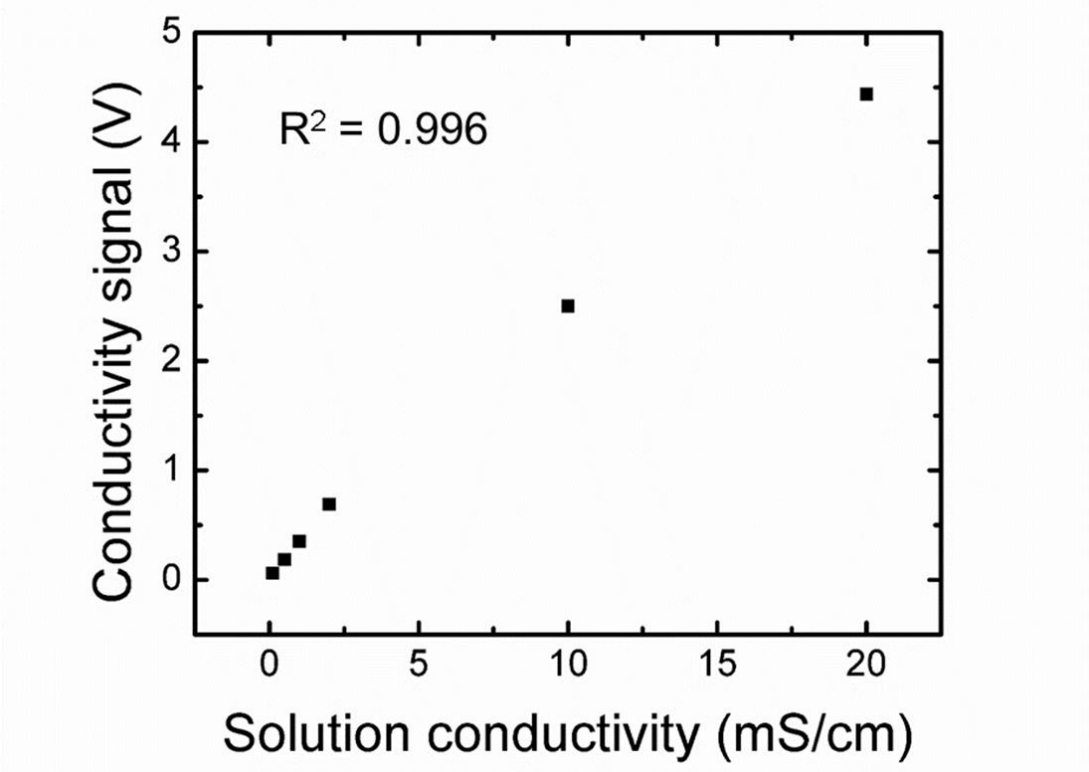

Figure C.1

Calibration curve used to correlate the measured conductivity signal (V) to solution conductivity (mS/cm). This is a typical calibration curve that was obtained using microbands 7 and 8 (Figure 5.2). Similar calibration curves were obtained for each of the three other highlighted pairs of microbands shown in Figure 5.2. The calibration curves were generated as follows. First, solutions having the following conductivities were prepared from conductivity standard solutions: 0.10, 0.50, 1.0, 2.0, 10.0, and 20.0 mS/cm (NaCl conductivity standards, RICCA Chemical Company, Arlington, TX). Second, the solutions were flowed through the microfluidic channel by pressure-driven flow (PDF). Third, solution conductivity measurements were performed. Typical coefficients of determination (R^2) for the calibration curves prepared using microbands 1 and 2, 7 and 8, 9 and 10, and 15 and 16 on three devices were 0.994 ± 0.003, 0.996 ± 0.003, 0.997 ± 0.002, and 0.994 ± 0.006, respectively.

C.2 Percentage of Cl^- oxidized at the Pt anode

The percentage of Cl^- oxidized at the Pt anode was determined by comparing the charge passed at the anode (Q_{passed}) to the maximum possible charge, which was taken as the total charge required to oxidize all of the Cl^- flowing past the anode ($Q_{present}$). We assumed that Cl^- oxidation proceeded at the Pt anode with 100% faradaic efficiency. A duration of 50 s was considered for the calculation of Q_{passed} and $Q_{present}$.

The amount of charge passed at the Pt anode during Cl^- oxidation was calculated using eq C.1, where i is current and t is time.

$$Q_{passed} = i \times t \qquad (C.1)$$

The steady-state current measured during electrochemical experiments (Figure 5.1b) was 2.42 ± 0.20 µA (36 replicates), which yields Q_{passed} = 1.21 x 10^{-4} C.

The value of $Q_{present}$ was calculated using eq C.2, where n is the number of electrons in the reaction (n = 1 e^-/Cl^-), F is the Faraday (96,485 C/mol), and N is the amount of Cl^- in moles.

$$Q_{present} = n \times F \times N \qquad (C.2)$$

The volume of solution flowing past the anode during a 50 s period is determined by multiplying the volumetric flow rate (83 nL/min or 1.38 x 10-12 m^3/s) by 50 s (= 6.9 x 10-11 m^3 or 6.9 x 10-8 L). Multiplying the volume of solution

flowing past the anode during a 50 s period by the concentration of the solution (0.050 M) provides the total number of moles of Cl^- passing the anode (3.45×10^{-9} moles of Cl^-). Using eq C.2, $Q_{present} = 3.33 \times 10^{-4}$ C. Hence $Q_{passed}/Q_{present} = 0.36$. In other words, 36% of the Cl^- potentially available to the anode is oxidized.

C.3 Cyclic voltammetry in NaCl solutions

Cyclic voltammetry was performed in the microelectrochemical device to verify the suppression of water oxidation at the Pt anode in the presence of a 50.0 mM NaCl solution. The experiment was carried out as follows. First, a solution containing 50.0 mM NaCl was flowed through the microelectrochemical device by PDF. Second, a potentiostat (760b, CH Instruments, Inc., Austin, TX) was used to apply a voltage between the Pt anode and the Pt cathodes located in the reservoirs in a two-electrode configuration (Figure 5.1a). The scan rate was 0.10 V/s. These procedures were repeated in the presence of 500.0 mM NaCl solution.

Figure C.2 shows that the shape of the voltammetric wave and the onset potential for electrochemical Cl^- oxidation are the same for experiments performed in the presence of 50.0 or 500.0 mM NaCl. However, the magnitude of the current passed at 1.5 V (vs. Pt) is larger in the case of 500.0 mM NaCl solution than 50.0 mM NaCl. This is

the expected result because the solution conductivity and concentration of the electrochemically active Cl^- species are higher for the 500.0 mM NaCl solution. In addition, because the NaCl solutions do not contain supporting electrolyte, electromigration contributes to the flux of Cl^- to the anode and the magnitude of the measured current response continues to increase as the applied voltage increases. We conclude from these results that electrochemical Cl^- oxidation is the primary reaction proceeding at the anode in the presence of 50.0 or 500.0 mM NaCl solution.[207]

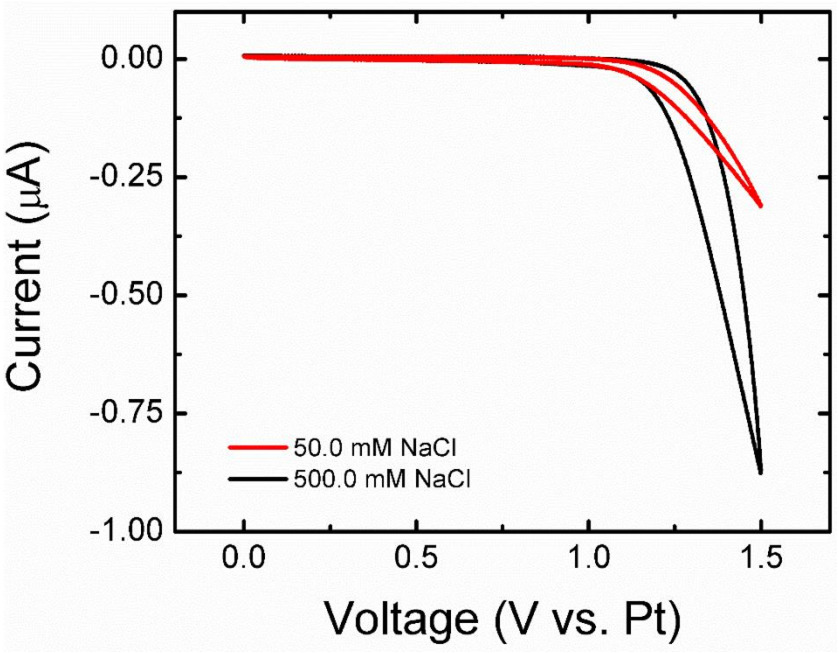

Figure C.2

Cyclic voltammetry performed in the microelectrochemical device in the presence of 50.0 mM or 500.0 mM NaCl solutions. The potentiostat was configured as a two-electrode cell and a voltage was applied between the Pt anode and the Pt cathodes as shown in Figure 5.1a. The scan rate was 0.10 V/s.

C.4 Electrochemical potential background subtraction

A small but measurable electrochemical potential (ECP) was present between neighboring pairs of microbands (Figure 5.1b) in the absence of an applied electric field or electrochemical reaction at the anode. This background ECP arises from slight differences in the properties of the individual microbands. Accordingly, it was measured and then subtracted from the ECP signal measured at steady state during application of 3.0 V between the anode and the cathodes for each experiment.

The details of the background correction process were as follows. Prior to application of 3.0 V between the anode and the cathodes, 10 background ECP measurements were performed for each pair of measurement microbands for 20 s. Next, the ECP was measured in the presence of 3.0 V, as discussed in Chapter 5. Finally, the average background ECP for each unique pair of measurement electrodes was subtracted from the average steady-state signal for the corresponding unique pair of measurement microbands with 3.0 V applied.

C.5 Numerical simulations

Finite element simulations were carried out using the COMSOL Multiphysics version 5.4 software package. Simulations were performed using a Dell Precision workstation (Model T7500)

equipped with two Intel Xeon processors (2.40 GHz) and 24 GB of RAM. All simulations were performed at steady state.

Simulations were performed using a two-dimensional (2D) model based on the xz-plane of the microfluidic system shown in Figure 5.1a. The modeled microfluidic channel was 23.0 µm high, and the anode was 50.0 µm wide and located along the channel floor. To capture the impact of electrochemical Cl^- oxidation on the distribution of solution species within the channel, we modeled 2475.0 µm upstream from the leading edge of the anode and 2475.0 µm downstream from the trailing edge of the anode. Accordingly, the length of the channel modeled was 5000.0 µm (2475.0 µm + 50.0 µm + 2475.0 µm).

The solution convection profile within the 2D model was simulated using the "Laminar Flow" interface in COMSOL Multiphysics. This interface solves the Navier-Stokes equation for incompressible flow of a viscous fluid (eqs C.3 and C.4).

$$\rho(u \cdot \nabla)u = \nabla \cdot [-pI + \mu(\nabla u + (\nabla u)^T)] + f_v \qquad (C.3)$$

$$\rho\nabla \times u = 0 \qquad (C.4)$$

Here, ρ is the density of the solution, u is the velocity vector of the solution, μ is its dynamic viscosity, p is pressure, I is the identity matrix, T is temperature, and f_v is the volume force vector.

The left boundary of the model was taken to be the laminar inflow with an average solution velocity of 514

μm/s. The right side of the model was a pressure boundary ($p = 0$) and the channel sidewalls (top and bottom boundaries) were modeled as no-slip boundaries.

The contribution of electroosmotic flow (EOF) to solution convection was approximated to be <6% of the total rate of solution convection and thus EOF was not included in the model.[40,156]

Mass transport within the model was simulated with the "Nernst-Planck" interface. This interface solves the Nernst-Planck equation with the electroneutrality condition to simulate the flux of species by convection, diffusion, and electromigration (eqs C.5-C.9).

$$\nabla \cdot J_i + u \cdot \nabla c_i = R_i \qquad (C.5)$$

$$\nabla \cdot i = F \sum_i z_i R_i \qquad (C.6)$$

$$\sum_i z_i c_i = 0 \qquad (C.7)$$

$$J_i = -D_i \nabla c_i - z_i \mu_{ep,i} F c_i \nabla \varphi \qquad (C.8)$$

$$i = F \sum_i z_i (-D_i \nabla c_i - z_i \mu_{ep,i} F c_i \nabla \varphi) \qquad (C.9)$$

Here, J_i is flux, c_i is concentration, R_i is the rate of reaction, z_i is the charge, D_i is the diffusion coefficient, and $\mu_{ep,i}$ is the electrophoretic mobility, all for species i. F is the Faraday. φ is the electric potential. The inlet was taken to have an inflow of 50.0 mM NaCl and the anode was taken to have a steady-state current of 2.42 μA. The potential of the inlet and outlet boundaries was 0 V. Cl^-

oxidation was modeled as a flux and proceeded at the anode with 100% faradaic efficiency.

Following electrochemical Cl_2 generation, aqueous Cl_2 chemistry was simulated (eqs 5.5 and 5.6). Cl_2 hydrolysis was simulated using a reaction rate equation (eq C.10).

$$R_{Cl_2} = -\left(k_{f,chloro}\alpha c_{Cl_2}\right) + \left(k_{b,chloro}\alpha c_{Cl^-}\alpha c_{H^+}\alpha c_{HOCl}\right) \qquad (C.10)$$

Here, R_{Cl_2} is the rate of Cl_2 hydrolysis, $k_{f,chloro}$ and $k_{b,chloro}$ are the forward and backward reaction rate constants,[202] respectively, and α is the activity coefficient. The Davies equation was used to calculate the activity coefficient for a NaCl solution having an ionic strength of 0.050 M. The activity coefficient was considered to be constant throughout the 2D model. Accordingly, $R_{Cl^-} = R_{H^+} = R_{HOCl} = -R_{Cl_2}$.

Solution conductivity (κ) was calculated from the distribution of solution species using eq C.11.

$$\kappa = \sum_i c_i \mu_{ep,i} (z_i F)^2 \qquad (C.11)$$

A user-controlled mesh was used to solve the multiphysics model. A relaxed mesh (maximum element size = 1.42, minimum element size = 0.0203) optimized for fluid dynamics was used throughout the majority of the modeled domain, while a more dense mesh (maximum and minimum element size = 0.005) was employed near the anode to enable accurate modeling of Cl_2 generation and rapid Cl_2 hydrolysis. The

quality of the mesh was confirmed by a mesh refinement study.

Finally, a study was performed to determine the sensitivity of simulated results to changes in the value of key parameters. Specifically, the model was solved for a ±10% change in the value of channel height ($h_{channel}$), channel width ($w_{channel}$), flow rate (v), anode length (l_{anode}), steady-state current (i_{ss}), initial concentration of NaCl ($cNaCl_0$), and α. Each parameter was varied independently. The results for each model were compared with the original model described fully in the accompanying COMSOL Multiphysics report (COMSOL Report 2). Numerical solution of the concentration of Na^+ (cNa), Cl^- (cCl), Cl_2 (cCl2), HOCl (cHOCl), and H^+ (cH), the electric potential (φ), and κ along the channel length at the central z height (z = 11.50 µm) were analyzed. A summary of the results is provided in Table C.1.

Table C.1

Percent change in the minimum value of cNa and cCl, and the maximum value of cCl2, cHOCl, cH, φ, and κ as a function of a ±10% change in the value of $h_{channel}$, $w_{channel}$, v, l_{anode}, i_{ss}, α, or $cNaCl_0$. The results of numerical simulation were analyzed along the channel length at the central z height (z = 11.50 μm). Changes in value of >6% are in red.

	cCl min	cNa min	cCl2 max	cHOCl max	cH max	φ max	κ max
-10% $h_{channel}$	-0.3%	-1.1%	5.2%	11.1%	8.0%	10.1%	1.8%
+10% $h_{channel}$	0.1%	0.7%	-2.5%	-9.1%	-6.8%	-8.3%	-1.5%
-10% $w_{channel}$	-0.7%	-1.4%	11.1%	11.1%	8.0%	10.1%	1.8%
+10% $w_{channel}$	0.6%	1.2%	-9.1%	-9.1%	-6.8%	-8.4%	-1.5%
-10% v	-0.2%	-1.4%	4.8%	11.2%	8.1%	-1.4%	1.8%
+10% v	0.2%	1.1%	-4.5%	-9.2%	-6.9%	1.1%	-1.6%
-10% l_{anode}	-0.2%	0.0%	3.7%	0.0%	0.0%	-0.4%	0.0%
+10% l_{anode}	0.2%	0.0%	-3.6%	0.0%	0.0%	0.4%	0.0%
-10% i_{ss}	0.6%	1.3%	-9.9%	-9.9%	-7.5%	-9.2%	-1.7%
+10% i_{ss}	-0.7%	-1.3%	9.9%	9.9%	7.1%	9.1%	1.6%
-10% α	-0.5%	-0.1%	7.5%	-0.1%	0.0%	0.4%	0.0%
+10% α	0.5%	0.1%	-6.7%	0.0%	0.0%	-0.3%	0.0%
-10% $cNaCl_0$	-10.7%	-11.3%	0.0%	0.0%	-2.8%	10.1%	-8.4%
+10% $cNaCl_0$	10.7%	11.3%	0.0%	0.0%	2.5%	-8.4%	8.3%

The key finding from Table C.1 is that a 10% change in the value of any single parameter leads to, at most, an ~11% change in the value of the simulated result. We conclude from this study that the accuracy of the numerical simulation is sufficient to identify trends in the change in concentration of solution species and the associated electric potential profile and solution conductivity.

Complete details for the parameters, geometry dimensions, and interface settings are available within the accompanying COMSOL Multiphysics report (COMSOL Report 2).

C.6 Open circuit potential measurements

The open circuit potential (OCP) of a Pt microband was measured in a macroscale Teflon cell while electrochemical reaction proceeded at a second Pt microband located nearby (Figure C.3).[211,216] *OCP measurements were performed as follows. First, a Teflon electrochemical cell containing the previously described photo-patterned Pt circuitry (Figure 5.1b), was assembled as shown in Figure C.3a. Second, the cell was filled with 1.0 mL of 50.0 mM NaCl solution. Third, a potentiostat (650c, CH Instruments, Inc., Austin, TX) connected between the Pt microband working electrode (WE), a Pt wire counter electrode (CE), and a leakless Ag/AgCl reference electrode (RE) was used to monitor the OCP of the WE (microband 8, Figure 5.1b). Fourth, a battery pack was used to apply 2.0 V between the Pt microband anode and a Pt wire cathode. Current passed through the circuit was measured using a hand-held multimeter connected in series. Fifth, triplicate measurements were performed. These procedures were repeated in the presence of Cl^--free control solution containing 50.0 mM Na_2SO_4.*

Figure C.3b is a representative plot of the OCP of the microband WE as a function of time in the presence of 50.0 mM NaCl or Na_2SO_4 solution. This plot reveals three distinct OCP regimes. First, prior to application of 2.0 V

between the anode and the cathode (0-100 s), the OCP of the Pt WE in bulk solution is measured. Second, application of 2.0 V (100-200 s) between the anode and the cathode results in electrochemical reaction(s) that alters the concentration of solution near the WE and shifts the OCP of the WE to more positive potentials. Specifically, application of 2.0 V between the anode and the cathode in the presence of 50.0 mM NaCl or Na_2SO_4 results in an OCP shift of +0.716 ± 0.006 V or +0.301 ± 0.017 V, respectively. Third, following application of 2.0 V between the anode and the cathode (200-300 s), the OCP of the WE drifts back toward the initial value measured in bulk solution.

The key finding from Figure C.3b is that electrochemical reaction(s) proceeding at the nearby anode shifts the OCP of the WE. An explanation for this result is as follows. In the case of 50.0 mM NaCl solution, Cl^- oxidation followed by rapid Cl_2 hydrolysis results in the production of strong oxidizing species (Cl_2 and HOCl) and H^+ near the anode and Pt microband WE (eqs 5.4-5.6).[203] These reactions change the ratio of oxidized to reduced species near the WE and, as predicted by the Nernst equation, shift the OCP of the WE.[210,217] In addition, a mixed potential arising from two or more half-reactions proceeding at the Pt WE can develop and further shift the measured OCP.[212,218] Accordingly, the chemical potential of solution near the WE

increases and the measured OCP shifts to more positive potentials.[219]

In the case of 50.0 mM Na_2SO_4, water oxidation results in the production of O_2 and H^+ near the anode and Pt microband WE (eq 5.3). These reactions change the ratio of oxidized to reduced species local to the WE, and again, as predicted by the Nernst equation, shift the OCP of the WE.[210,217] *Thus, production of O_2 and H^+ increases the chemical potential of solution near the WE and a moderate increase in the OCP of the WE is measured.*[219] *Importantly, electrochemical reactions proceeding at the anode shift the OCP of the nearby Pt WE.*

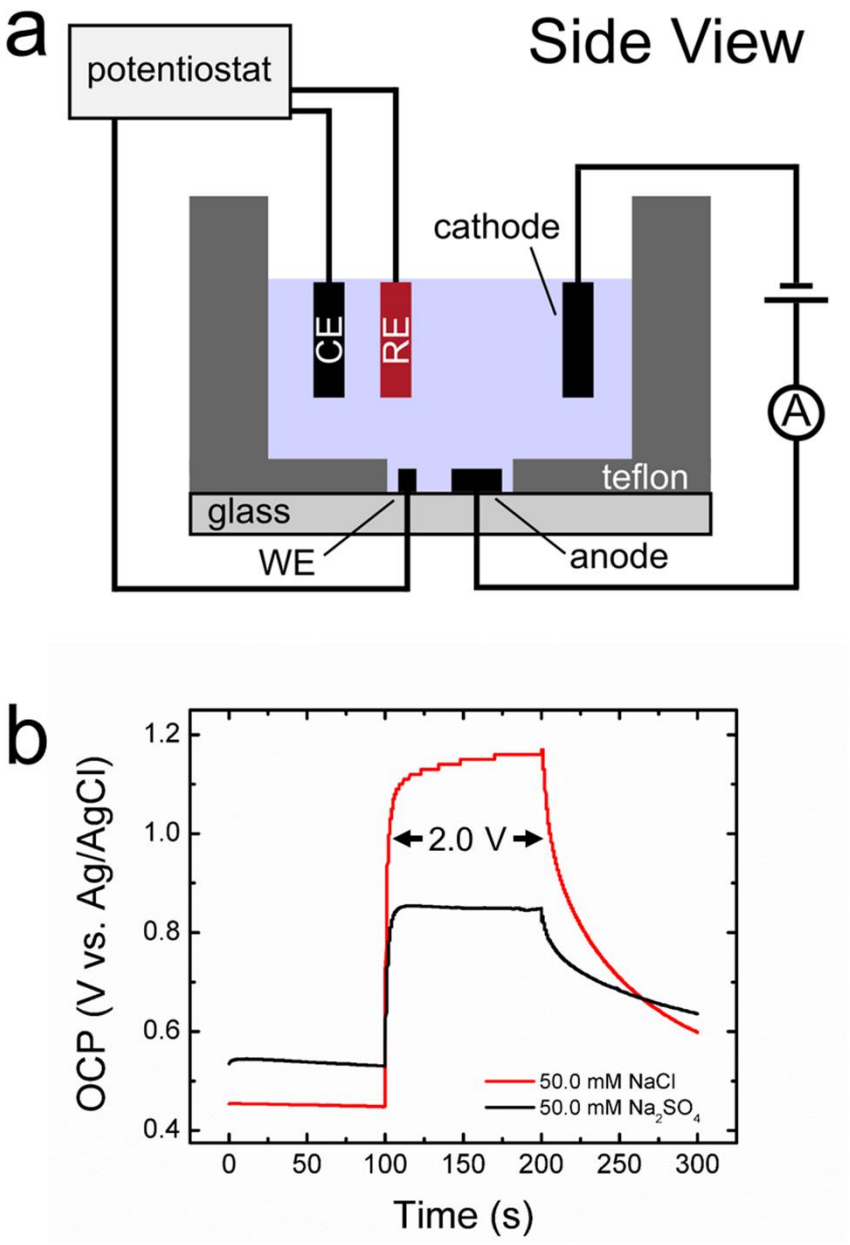

Figure C.3

(a) Schematic illustration of the macroscale cell used to perform OCP measurements. (b) Representative plot of the OCP of the WE as a function of time in the presence of 50.0 mM NaCl or Na_2SO_4 solution. A battery pack was used to apply 2.0 V between the anode and the cathode from 100-200 s. For 50.0 mM NaCl, this results in oxidation of Cl^- at the anode (eq 5.4). For 50.0 mM Na_2SO_4, it results in oxidation of water (eq 5.3).

Glossary

2D	Two-dimensional
$BODIPY^{2-}$	BODIPY disulfonate fluorophore
BPE	Bipolar electrode
BPE1	Bipolar electrode one
BPE2	Bipolar electrode two
cCl	Simulated concentration for Cl^-
cCl2	Simulated concentration for Cl_2
CE	Counter electrode
cH	Simulated concentration for H^+
cHOCl	Simulated concentration for HOCl
c_i	Concentration for species i
cNa	Simulated concentration for Na^+
$cNaCl_0$	Initial concentration for NaCl
D_i	Diffusion coefficient for species i
DI water	Deionized water
ECP	Electrochemical potential
EFG	Electric field gradient
EOF	Electroosmotic flow
E_{tot}	Driving voltage
F	Faraday
fICP	Faradaic ion concentration polarization
f_v	Volume force vector
fμB	Fluorescent polystyrene microbead
$h_{channel}$	Channel height

i	Current
I	Identity matrix
i_{BPE}	Current passed through bipolar electrode
i_{BPE1}	Current passed through bipolar electrode one
i_{BPE2}	Current passed through bipolar electrode two
ICP	Ion concentration polarization
IDZ	Ion depletion zone
IEZ	Ion enrichment zone
i_{ss}	Steady-state current
i_{tot}	Current passed through driving electrodes
J_i	Flux for species i
$k_{b,chloro}$	Backward reaction rate for Cl_2 hydrolysis
$k_{b,hydro}$	Backward reaction rate for water self-ionization
$k_{b,neut}$	Backward reaction rate for $TrisH^+$ neutralization
$k_{f,chloro}$	Forward reaction rate for Cl_2 hydrolysis
$k_{f,hydro}$	Forward reaction rate for water self-ionization
$k_{f,neut}$	Forward reaction rate for $TrisH^+$ neutralization
l_{anode}	Anode length
$l_{channel}$	Channel length
l_{elec}	Bipolar electrode length
n	Number of e^-

N	Number of moles
OCP	Open circuit potential
p	Pressure
PDF	Pressure-driven flow
PDMS	Poly(dimethylsiloxane)
Q_{passed}	Charge passed at the anode
$Q_{present}$	Total charge present in solution passing by the anode
R^2	Coefficient of determination
RAM	Random-access memory
R_{Cl^-}	Rate of reaction for Cl^-
R_{Cl_2}	Rate of reaction for Cl_2
RE	Reference electrode
R_{H^+}	Rate of reaction for H^+
R_{HOCl}	Rate of reaction for HOCl
R_i	Rate of reaction for species i
R_{OH^-}	Rate of reaction for OH^-
R_{Tris}	Rate of reaction for Tris
R_{TrisH^+}	Rate of reaction for $TrisH^+$
t	Time
T	Temperature
Tris	Tris(hydroxymethyl)aminomethane
u	Velocity vector
V	Flow rate
$w_{channel}$	Channel width

WE	*Working electrode*
z_i	*Charge for species i*
α	*Activity coefficient*
ΔE_{elec}	*Potential difference between the bipolar electrode ends and solution*
κ	*Solution conductivity*
μ	*Dynamic viscosity*
µB	*Non-fluorescent polystyrene microbead*
μ_{ep}	*Electrophoretic mobility*
$\mu_{ep,i}$	*Electrophoretic mobility for species i*
µP1	*Microplastic particle (diameter = 0.99 µm)*
µP2	*Microplastic particle (diameter = 1.04 µm)*
µP3	*Microplastic particle (diameter = 0.20 µm)*
ρ	*Density*
φ	*Electric potential*

References

(1) Sholl, D. S.; Lively, R. P. Seven chemical separations to change the world. *Nature* **2016**, *532*, 435-437.

(2) U.S. Department of Energy. Materials for separation technologies: Energy and emission reduction opportunities. United States, 2005.

(3) Humphrey, J. L.; Keller, G. E. Separation process technology. McGraw-Hill, 1997.

(4) Nath, K. Membrane separation processes, 2nd ed.; PHI Learning Private Limited: Delhi, 2017.

(5) Visvanathan, C.; Ben Aim, R.; Parameshwaran, K. Membrane separation bioreactors for wastewater treatment. *Crit. Rev. Env. Sci. Tec.* **2000**, *30*, 1-48.

(6) Takht Ravanchi, M.; Kaghazchi, T.; Kargari, A. Application of membrane separation processes in petrochemical industry: A review. *Desalination* **2009**, *235*, 199-244.

(7) Werber, J. R.; Deshmukh, A.; Elimelech, M. The critical need for increased selectivity, not increased water permeability, for desalination membranes. *Environ. Sci. Technol. Lett.* **2016**, *3*, 112-120.

(8) Werber, J. R.; Osuji, C. O.; Elimelech, M. Materials

for next-generation desalination and water purification membranes. Nat. Rev. Mater. **2016**, *1*, 16018.

(9) *Shannon, M. A.; Bohn, P. W.; Elimelech, M.; Georgiadis, J. G.; Mariñas, B. J.; Mayes, A. M. Science and technology for water purification in the coming decades. Nature* **2008**, *452*, 301-310.

(10) *Logan, B. E.; Elimelech, M. Membrane-based processes for sustainable power generation using water. Nature* **2012**, *488*, 313-319.

(11) *Elimelech, M.; Phillip, W. A. The future of seawater desalination: Energy, technology, and the environment. Science* **2011**, *333*, 712-717.

(12) *Geise, G. M.; Park, H. B.; Sagle, A. C.; Freeman, B. D.; McGrath, J. E. Water permeability and water/salt selectivity tradeoff in polymers for desalination. J. Membr. Sci.* **2011**, *369*, 130-138.

(13) *Koegler, W. S.; Ivory, C. F. Field gradient focusing: A novel method for protein separation. Biotechnol. Prog.* **1996**, *12*, 822-836.

(14) *Koegler, W. S.; Ivory, C. F. Focusing proteins in an electric field gradient. J. Chromatogr. A* **1996**, *726*, 229-236.

(15) *Shackman, J. G.; Ross, D. Counter-flow gradient*

electrofocusing. Electrophoresis **2007**, *28*, 556-571.

(16) *Kelly, R. T.; Woolley, A. T. Electric field gradient focusing. J. Sep. Sci.* **2005**, *28*, 1985-1993.

(17) *Li, M.; Anand, R. K. Recent advancements in ion concentration polarization. Analyst* **2016**, *141*, 3496-3510.

(18) *Dai, J.; Ito, T.; Sun, L.; Crooks, R. M. Electrokinetic trapping and concentration enrichment of DNA in a microfluidic channel. J. Am. Chem. Soc.* **2003**, *125*, 13026-13027.

(19) *Pu, Q.; Yun, J.; Temkin, H.; Liu, S. Ion-enrichment and ion-depletion effect of nanochannel structures. Nano Lett.* **2004**, *4*, 1099-1103.

(20) *Wang, Y.-C.; Stevens, A. L.; Han, J. Million-fold preconcentration of proteins and peptides by nanofluidic filter. Anal. Chem.* **2005**, *77*, 4293-4299.

(21) *Greenlee, R. D.; Ivory, C. F. Protein focusing in a conductivity gradient. Biotechnol. Prog.* **1998**, *14*, 300-309.

(22) *Hoeman, K. W.; Lange, J. J.; Roman, G. T.; Higgins, D. A.; Culbertson, C. T. Electrokinetic trapping using titania nanoporous membranes fabricated using sol-gel chemistry on microfluidic devices. Electrophoresis* **2009**, *30*, 3160-3167.

(23) *Mani, A.; Zangle, T. A.; Santiago, J. G. On the propagation of concentration polarization from microchannel-nanochannel interfaces part I: Analytical model and characteristic analysis. Langmuir* **2009**, *25*, 3898-3908.

(24) *Zangle, T. A.; Mani, A.; Santiago, J. G. On the propagation of concentration polarization from microchannel-nanochannel interfaces part II: Numerical and experimental study. Langmuir* **2009**, *25*, 3909-3916.

(25) *Kim, S. J.; Song, Y.-A.; Han, J. Nanofluidic concentration devices for biomolecules utilizing ion concentration polarization: Theory, fabrication, and applications. Chem. Soc. Rev.* **2010**, *39*, 912-922.

(26) *Kim, S. J.; Wang, Y.-C.; Lee, J. H.; Jang, H.; Han, J. Concentration polarization and nonlinear electrokinetic flow near a nanofluidic channel. Phys. Rev. Lett.* **2007**, *99*, 044501.

(27) *Ismagilov, R. F.; Ng, J. M. K.; Kenis, P. J. A.; Whitesides, G. M. Microfluidic arrays of fluid-fluid diffusional contacts as detection elements and combinatorial tools. Anal. Chem.* **2001**, *73*, 5207-5213.

(28) *Chueh, B.; Huh, D.; Kyrtsos, C. R.; Houssin, T.; Futai, N.; Takayama, S. Leakage-free bonding of*

porous membranes into layered microfluidic array systems. Anal. Chem. **2007**, *79*, 3504–3508.

(29) *Warkiani, M. E.; Wicaksana, F.; Fane, A. G.; Gong, H.-Q. Investigation of membrane fouling at the microscale using isopore filters. Microfluid. Nanofluidics* **2015**, *19*, 307–315.

(30) *Meng, F.; Chae, S.-R.; Drews, A.; Kraume, M.; Shin, H.-S.; Yang, F. Recent advances in membrane bioreactors (MBRs): Membrane fouling and membrane material. Water Res.* **2009**, *43*, 1489–1512.

(31) *Guo, W.; Ngo, H.-H.; Li, J. A mini-review on membrane fouling. Bioresour. Technol.* **2012**, *122*, 27–34.

(32) *Jiang, S.; Li, Y.; Ladewig, B. P. A review of reverse osmosis membrane fouling and control strategies. Sci. Total Environ.* **2017**, *595*, 567–583.

(33) *Han, S. I.; Kyoung, Y. Y.; Lee, J.; Kim, C.; Lee, K.; Lee, T. H.; Kim, H.; Yoon, D. S.; Hwang, K. S.; Kwak, R.; Lee, J. H. High-ionic-strength pre-concentration via ion concentration polarization for blood-based biofluids. Sens. Actuators B Chem.* **2018**, *268*, 485–493.

(34) *Dhopeshwarkar, R.; Hlushkou, D.; Nguyen, M.; Tallarek, U.; Crooks, R. M. Electrokinetics in microfluidic channels containing a floating*

electrode. J. Am. Chem. Soc. **2008**, *130*, 10480-10481.

(35) *Hlushkou, D.; Perdue, R. K.; Dhopeshwarkar, R.; Crooks, R. M.; Tallarek, U. Electric field gradient focusing in microchannels with embedded bipolar electrode. Lab Chip* **2009**, *9*, 1903-1913.

(36) *Perdue, R. K.; Laws, D. R.; Hlushkou, D.; Tallarek, U.; Crooks, R. M. Bipolar electrode focusing: The effect of current and electric field on concentration enrichment. Anal. Chem.* **2009**, *81*, 10149-10155.

(37) *Laws, D. R.; Hlushkou, D.; Perdue, R. K.; Tallarek, U.; Crooks, R. M. Bipolar electrode focusing: Simultaneous concentration enrichment and separation in a microfluidic channel containing a bipolar electrode. Anal. Chem.* **2009**, *81*, 8923-8929.

(38) *Anand, R. K.; Sheridan, E.; Knust, K. N.; Crooks, R. M. Bipolar electrode focusing: Faradaic ion concentration polarization. Anal. Chem.* **2011**, *83*, 2351-2358.

(39) *Anand, R. K.; Sheridan, E.; Hlushkou, D.; Tallarek, U.; Crooks, R. M. Bipolar electrode focusing: Tuning the electric field gradient. Lab Chip* **2011**, *11*, 518-527.

(40) *Sheridan, E.; Hlushkou, D.; Anand, R. K.; Laws, D. R.; Tallarek, U.; Crooks, R. M. Label-free*

electrochemical monitoring of concentration enrichment during bipolar electrode focusing. Anal. Chem. **2011**, *83*, 6746–6753.

(41) *Kwak, R.; Kim, S. J.; Han, J. Continuous-flow biomolecule and cell concentrator by ion concentration polarization. Anal. Chem.* **2011**, *83*, 7348–7355.

(42) *Kim, S. M.; Burns, M. A.; Hasselbrink, E. F. Electrokinetic protein preconcentration using a simple glass/poly(dimethylsiloxane) microfluidic chip. Anal. Chem.* **2006**, *78*, 4779–4785.

(43) *Huang, K.-D.; Yang, R.-J. Formation of ionic depletion/enrichment zones in a hybrid micro-/nano-channel. Microfluid. Nanofluidics* **2008**, *5*, 631–638.

(44) *Plecis, A.; Nanteuil, C.; Haghiri-Gosnet, A.-M.; Chen, Y. Electropreconcentration with charge-selective nanochannels. Anal. Chem.* **2008**, *80*, 9542–9550.

(45) *Ouyang, W.; Ye, X.; Li, Z.; Han, J. Deciphering ion concentration polarization-based electrokinetic molecular concentration at the micro-nanofluidic interface: Theoretical limits and scaling laws. Nanoscale* **2018**, *10*, 15187–15194.

(46) *Chatterjee, A. N.; Cannon, D. M.; Gatimu, E. N.;*

Sweedler, J. V; Aluru, N. R.; Bohn, P. W. Modeling and simulation of ionic currents in three-dimensional microfluidic devices with nanofluidic interconnects. J. Nanopart. Res. **2005**, *7*, 507–516.

(47) *Strickland, D. G.; Suss, M. E.; Zangle, T. A.; Santiago, J. G. Evidence shows concentration polarization and its propagation can be key factors determining electroosmotic pump performance. Sens. Actuators B Chem.* **2010**, *143*, 795–798.

(48) *Zangle, T. A.; Mani, A.; Santiago, J. G. Theory and experiments of concentration polarization and ion focusing at microchannel and nanochannel interfaces. Chem. Soc. Rev.* **2010**, *39*, 1014–1035.

(49) *Jin, X.; Joseph, S.; Gatimu, E. N.; Bohn, P. W.; Aluru, N. R. Induced electrokinetic transport in micro-nanofluidic interconnect devices. Langmuir* **2007**, *23*, 13209–13222.

(50) *Qiu, B.; Gong, L.; Li, Z.; Han, J. Electrokinetic flow in the U-shaped micro-nanochannels. Theor. App. Mech. Lett.* **2019**, *9*, 36–42.

(51) *Jia, M.; Kim, T. Multiphysics simulation of ion concentration polarization induced by nanoporous membranes in dual channel devices. Anal. Chem.* **2014**, *86*, 7360–7367.

(52) Ouyang, W.; Li, Z.; Han, J. Pressure-modulated selective electrokinetic trapping for direct enrichment, purification, and detection of nucleic acids in human serum. *Anal. Chem.* **2018**, *90*, 11366–11375.

(53) Han, S. I.; Hwang, K. S.; Kwak, R.; Lee, J. H. Microfluidic paper-based biomolecule preconcentrator based on ion concentration polarization. *Lab Chip* **2016**, *16*, 2219–2227.

(54) Kim, S. J.; Ko, S. H.; Kang, K. H.; Han, J. Direct seawater desalination by ion concentration polarization. *Nat. Nanotechnol.* **2010**, *5*, 297–301.

(55) Li, J.; Chen, D.; Ye, J.; Zhang, L.; Zhou, T.; Zhou, Y. Direct numerical simulation of seawater desalination based on ion concentration polarization. *Micromachines* **2019**, *10*, 562.

(56) Choi, S.; Kim, B.; Nayar, K. G.; Yoon, J.; Al-Hammadi, S.; Lienhard V, J. H.; Han, J.; Al-Anzi, B. Techno-economic analysis of ion concentration polarization desalination for high salinity desalination applications. *Water Res.* **2019**, *155*, 162–174.

(57) Deng, D.; Aouad, W.; Braff, W. A.; Schlumpberger, S.; Suss, M. E.; Bazant, M. Z. Water purification by

shock electrodialysis: Deionization, filtration, separation, and disinfection. Desalination **2015**, *357*, 77–83.

(58) *MacDonald, B. D.; Gong, M. M.; Zhang, P.; Sinton, D. Out-of-plane ion concentration polarization for scalable water desalination. Lab Chip* **2014**, *14*, 681–685.

(59) *Gong, L.; Ouyang, W.; Li, Z.; Han, J. Direct numerical simulation of continuous lithium extraction from high* Mg^{2+}/Li^{+} *ratio brines using microfluidic channels with ion concentration polarization. J. Membr. Sci.* **2018**, *556*, 34–41.

(60) *abu-Rjal, R.; Chinaryan, V.; Bazant, M. Z.; Rubinstein, I.; Zaltzman, B. Effect of concentration polarization on permselectivity. Phys. Rev. E* **2014**, *89*, 012302.

(61) *Yeh, L.-H.; Zhang, M.; Qian, S.; Hsu, J.-P.; Tseng, S. Ion concentration polarization in polyelectrolyte-modified nanopores. J. Phys. Chem. C* **2012**, *116*, 8672–8677.

(62) *Yeh, L.-H.; Hughes, C.; Zeng, Z.; Qian, S. Tuning ion transport and selectivity by a salt gradient in a charged nanopore. Anal. Chem.* **2014**, *86*, 2681–2686.

(63) *Holtzel, A.; Tallarek, U. Ionic conductance of*

nanopores in microscale analysis systems: Where microfluidics meets nanofluidics. J. Sep. Sci. **2007**, *30*, 1398–1419.

(64) *Tang, C. Y.; She, Q.; Lay, W. C. L.; Wang, R.; Fane, A. G. Coupled effects of internal concentration polarization and fouling on flux behavior of forward osmosis membranes during humic acid filtration. J. Membr. Sci.* **2010**, *354*, 123–133.

(65) *Jain, T.; Guerrero, R. J. S.; Aguilar, C. A.; Karnik, R. Integration of solid-state nanopores in microfluidic networks via transfer printing of suspended membranes. Anal. Chem.* **2013**, *85*, 3871–3878.

(66) *Fosdick, S. E.; Knust, K. N.; Scida, K.; Crooks, R. M. Bipolar electrochemistry. Angew. Chem. Int. Ed.* **2013**, *52*, 10438–10456.

(67) *Loget, G.; Kuhn, A. Shaping and exploring the micro- and nanoworld using bipolar electrochemistry. Anal. Bioanal. Chem.* **2011**, *400*, 1691–1704.

(68) *Koefoed, L.; Pedersen, S. U.; Daasbjerg, K. Bipolar electrochemistry – A wireless approach for electrode reactions. Curr. Opin. Electrochem.* **2017**, *2*, 13–17.

(69) *Mavré, F.; Anand, R. K.; Laws, D. R.; Chow, K.-F.; Chang, B.-Y.; Crooks, J. A.; Crooks, R. M. Bipolar electrodes: A useful tool for concentration,*

separation, and detection of analytes in microelectrochemical systems. Anal. Chem. **2010**, *82, 8766-8774.*

(70) *Scida, K.; Sheridan, E.; Crooks, R. M. Electrochemically-gated delivery of analyte bands in microfluidic devices using bipolar electrodes. Lab Chip* **2013**, *13, 2292-2299.*

(71) *Knust, K. N.; Hlushkou, D.; Anand, R. K.; Tallarek, U.; Crooks, R. M. Electrochemically mediated seawater desalination. Angew. Chem. Int. Ed.* **2013**, *52, 8107-8110.*

(72) *Knust, K. N.; Hlushkou, D.; Tallarek, U.; Crooks, R. M. Electrochemical desalination for a sustainable water future. ChemElectroChem* **2014**, *1, 850-857.*

(73) *Hlushkou, D.; Knust, K. N.; Crooks, R. M.; Tallarek, U. Numerical simulation of electrochemical desalination. J. Phys. Condens. Matter* **2016**, *28, 194001.*

(74) *American Chemical Society National Historic Chemical Landmarks. Bakelite: The world`s first synthetic plastic. http://www.acs.org/content/acs/en/education/whatischemistry/landmarks/bakelite.html (accessed Apr 13, 2020).*

(75) Thompson, R. C.; Swan, S. H.; Moore, C. J.; vom Saal, F. S. Our plastic age. *Phil. Trans. R. Soc. B* **2009**, *364*, 1973–1976.

(76) Andrady, A. L.; Neal, M. A. Applications and societal benefits of plastics. *Phil. Trans. R. Soc. B* **2009**, *364*, 1977–1984.

(77) Jayasinghe, R.; Mushtaq, U.; Smythe, T. A.; Baillie, C. The garbage crisis: A global challenge for engineers. Morgan & Claypool Publishers, 2013; Vol. 7.

(78) Rochman, C. M.; Browne, M. A.; Halpern, B. S.; Hentschel, B. T.; Hoh, E.; Karapanagioti, H. K.; Rios-Mendoza, L. M.; Takada, H.; Teh, S.; Thompson, R. C. Classify plastic waste as hazardous. *Nature* **2013**, *494*, 169–171.

(79) Jambeck, J. R.; Geyer, R.; Wilcox, C.; Siegler, T. R.; Perryman, M.; Andrady, A.; Narayan, R.; Law, K. L. Plastic waste inputs from land into the ocean. *Science* **2015**, *347*, 768–771.

(80) Vegter, A. C.; Barletta, M.; Beck, C.; Borrero, J.; Burton, H.; Campbell, M. L.; Costa, M. F.; Eriksen, M.; Eriksson, C.; Estrades, A.; Gilardi, K. V. K.; Hardesty, B. D.; Ivar do Sul, J. A.; Lavers, J. L.; Lazar, B.; Lebreton, L.; Nichols, W. J.; Ribic, C.

A.; Ryan, P. G.; Schuyler, Q. A.; Smith, S. D. A.; Takada, H.; Townsend, K. A.; Wabnitz, C. C. C.; Wilcox, C.; Young, L. C.; Hamann, M. Global research priorities to mitigate plastic pollution impacts on marine wildlife. *Endanger. Species Res.* **2014**, *25*, 225-247.

(81) Eriksen, M.; Lebreton, L. C. M.; Carson, H. S.; Thiel, M.; Moore, C. J.; Borerro, J. C.; Galgani, F.; Ryan, P. G.; Reisser, J. Plastic pollution in the world`s oceans: More than 5 trillion plastic pieces weighing over 250,000 tons afloat at sea. *PLoS One* **2014**, *9*, e111913.

(82) Lechner, A.; Keckeis, H.; Lumesberger-Loisl, F.; Zens, B.; Krusch, R.; Tritthart, M.; Glas, M.; Schludermann, E. The Danube so colourful: A potpourri of plastic litter outnumbers fish larvae in Europe`s second largest river. *Environ. Pollut.* **2014**, *188*, 177-181.

(83) Free, C. M.; Jensen, O. P.; Mason, S. A.; Eriksen, M.; Williamson, N. J.; Boldgiv, B. High-levels of microplastic pollution in a large, remote, mountain lake. *Mar. Pollut. Bull.* **2014**, *85*, 156-163.

(84) Dris, R.; Gasperi, J.; Rocher, V.; Saad, M.; Renault, N.; Tassin, B. Microplastic contamination in an urban

area: A case study in Greater Paris. Environ. Chem. **2015**, *12*, 592–599.

(85) *Talsness, C. E.; Andrade, A. J. M.; Kuriyama, S. N.; Taylor, J. A.; vom Saal, F. S. Components of plastic: Experimental studies in animals and relevance for human health. Phil. Trans. R. Soc. B* **2009**, *364*, 2079–2096.

(86) *Lebreton, L.; Andrady, A. Future scenarios of global plastic waste generation and disposal. Palgrave Commun.* **2019**, *5*, 6.

(87) *Halden, R. U. Plastics and health risks. Annu. Rev. Public Health* **2010**, *31*, 179–194.

(88) *Hopewell, J.; Dvorak, R.; Kosior, E. Plastics recycling: Challenges and opportunities. Phil. Trans. R. Soc. B* **2009**, *364*, 2115–2126.

(89) *Thompson, R. C.; Olsen, Y.; Mitchell, R. P.; Davis, A.; Rowland, S. J.; John, A. W. G.; McGonigle, D.; Russell, A. E. Lost at sea: Where is all the plastic? Science* **2004**, *304*, 838.

(90) *Microplastics in drinking-water. Geneva: World Health Organization; 2019. Licencee: CCBY-NC-SA 3.0 IGO.*

(91) *A Scientific Perspective on Microplastics in Nature and Society. Berlin: Science Advice for Policy by European Academies; 2019.*

https://doi.org/10.26356/microplastics

(92) *Rochman, C. M. Microplastics research—From sink to source. Science* **2018**, *360*, 28–29.

(93) *Sharma, S.; Chatterjee, S. Microplastic pollution, a threat to marine ecosystem and human health: A short review. Environ. Sci. Pollut. Res.* **2017**, *24*, 21530–21547.

(94) *Gasperi, J.; Wright, S. L.; Dris, R.; Collard, F.; Mandin, C.; Guerrouache, M.; Langlois, V.; Kelly, F. J.; Tassin, B. Microplastics in air: Are we breathing it in? Curr. Opin. Environ. Sci. Heal.* **2018**, *1*, 1–5.

(95) *Chen, G.; Feng, Q.; Wang, J. Mini-review of microplastics in the atmosphere and their risks to humans. Sci. Total Environ.* **2020**, *703*, 135504.

(96) *Schwabl, P.; Köppel, S.; Königshofer, P.; Bucsics, T.; Trauner, M.; Reiberger, T.; Liebmann, B. Detection of various microplastics in human stool: A prospective case series. Ann. Intern. Med.* **2019**, *171*, 453–457.

(97) *Wright, S. L.; Kelly, F. J. Plastic and human health: A micro issue? Environ. Sci. Technol.* **2017**, *51*, 6634–6647.

(98) *Chang, C. The immune effects of naturally occurring and synthetic nanoparticles. J. Autoimmun.* **2010**, *34*,

J234–J246.

(99) *Valavanidis, A.; Vlachogianni, T.; Fiotakis, K.; Loridas, S. Pulmonary oxidative stress, inflammation and cancer: Respirable particulate matter, fibrous dusts and ozone as major causes of lung carcinogenesis through reactive oxygen species mechanisms. Int. J. Environ. Res. Public Health* **2013**, *10*, 3886–3907.

(100) *von Moos, N.; Burkhardt-Holm, P.; Köhler, A. Uptake and effects of microplastics on cells and tissue of the blue mussel Mytilus edulis L. after an experimental exposure. Environ. Sci. Technol.* **2012**, *46*, 11327–11335.

(101) *Browne, M. A.; Dissanayake, A.; Galloway, T. S.; Lowe, D. M.; Thompson, R. C. Ingested microscopic plastic translocates to the circulatory system of the mussel, Mytilus edulis (L.). Environ. Sci. Technol.* **2008**, *42*, 5026–5031.

(102) *Mattsson, K.; Johnson, E. V; Malmendal, A.; Linse, S.; Hansson, L.-A.; Cedervall, T. Brain damage and behavioural disorders in fish induced by plastic nanoparticles delivered through the food chain. Sci. Rep.* **2017**, *7*, 11452.

(103) *Deng, Y.; Zhang, Y.; Lemos, B.; Ren, H. Tissue*

accumulation of microplastics in mice and biomarker responses suggest widespread health risks of exposure. Sci. Rep. **2017**, *7*, 46687.

(104) *Alimi, O. S.; Farner Budarz, J.; Hernandez, L. M.; Tufenkji, N. Microplastics and nanoplastics in aquatic environments: Aggregation, deposition, and enhanced contaminant transport. Environ. Sci. Technol.* **2018**, *52*, 1704-1724.

(105) *Turner, A.; Holmes, L. A. Adsorption of trace metals by microplastic pellets in fresh water. Environ. Chem.* **2015**, *12*, 600-610.

(106) *Cole, M.; Lindeque, P.; Halsband, C.; Galloway, T. S. Microplastics as contaminants in the marine environment: A review. Mar. Pollut. Bull.* **2011**, *62*, 2588-2597.

(107) *Campanale, C.; Massarelli, C.; Savino, I.; Locaputo, V.; Uricchio, V. F. A detailed review study on potential effects of microplastics and additives of concern on human health. Int. J. Environ. Res. Public Health* **2020**, *17*, 1212.

(108) *Luo, H.; Li, Y.; Zhao, Y.; Xiang, Y.; He, D.; Pan, X. Effects of accelerated aging on characteristics, leaching, and toxicity of commercial lead chromate pigmented microplastics. Environ. Pollut.* **2020**, *257*,

113475.

(109) *Andrady, A. L. The plastic in microplastics: A review. Mar. Pollut. Bull.* **2017**, *119*, 12–22.

(110) *Kwon, J.-H.; Chang, S.; Hong, S. H.; Shim, W. J. Microplastics as a vector of hydrophobic contaminants: Importance of hydrophobic additives. Integr. Environ. Assess. Manag.* **2017**, *13*, 494–499.

(111) *Nobre, C. R.; Santana, M. F. M.; Maluf, A.; Cortez, F. S.; Cesar, A.; Pereira, C. D. S.; Turra, A. Assessment of microplastic toxicity to embryonic development of the sea urchin Lytechinus variegatus (Echinodermata: Echinoidea). Mar. Pollut. Bull.* **2015**, *92*, 99–104.

(112) *Andrady, A. L. Microplastics in the marine environment. Mar. Pollut. Bull.* **2011**, *62*, 1596–1605.

(113) *Rummel, C. D.; Jahnke, A.; Gorokhova, E.; Kühnel, D.; Schmitt-Jansen, M. Impacts of biofilm formation on the fate and potential effects of microplastic in the aquatic environment. Environ. Sci. Technol. Lett.* **2017**, *4*, 258–267.

(114) *Miao, L.; Wang, P.; Hou, J.; Yao, Y.; Liu, Z.; Liu, S.; Li, T. Distinct community structure and microbial functions of biofilms colonizing microplastics. Sci. Total Environ.* **2019**, *650*, 2395–2402.

(115) Abraham, W.-R. Controlling biofilms of gram-positive pathogenic bacteria. *Current Med. Chem.* **2006**, *13*, 1509–1524.

(116) Bakir, A.; Rowland, S. J.; Thompson, R. C. Enhanced desorption of persistent organic pollutants from microplastics under simulated physiological conditions. *Environ. Pollut.* **2014**, *185*, 16–23.

(117) Koelmans, A. A.; Besseling, E.; Foekema, E.; Kooi, M.; Mintenig, S.; Ossendorp, B. C.; Redondo-Hasselerharm, P. E.; Verschoor, A.; van Wezel, A. P.; Scheffer, M. Risks of plastic debris: Unravelling fact, opinion, perception, and belief. *Environ. Sci. Technol.* **2017**, *51*, 11513–11519.

(118) Koelmans, A. A.; Mohamed Nor, N. H.; Hermsen, E.; Kooi, M.; Mintenig, S. M.; De France, J. Microplastics in freshwaters and drinking water: Critical review and assessment of data quality. *Water Res.* **2019**, *155*, 410–422.

(119) Prata, J. C.; da Costa, J. P.; Duarte, A. C.; Rocha-Santos, T. Methods for sampling and detection of microplastics in water and sediment: A critical review. *TrAC Trends Anal. Chem.* **2019**, *110*, 150–159.

(120) Lusher, A. L.; Burke, A.; O`Connor, I.; Officer, R. Microplastic pollution in the Northeast Atlantic

Ocean: Validated and opportunistic sampling. Mar. Pollut. Bull. **2014**, *88*, 325–333.

(121) *Löder, M. G. J.; Gerdts, G. Methodology used for the detection and identification of microplastics—A critical appraisal. In Marine Anthropogenic Litter; Bergmann, M., Gutow, L., Klages, M., Eds.; Springer International Publishing: Cham, 2015; pp 201–227.*

(122) *Law, K. L.; Thompson, R. C. Microplastics in the seas. Science* **2014**, *345*, 144–145.

(123) *Koelmans, A. A.; Besseling, E.; Shim, W. J. Nanoplastics in the aquatic environment. Critical Review. In Marine Anthropogenic Litter; Bergmann, M., Gutow, L., Klages, M., Eds.; Springer International Publishing: Cham, 2015; pp 325–340.*

(124) *Strungaru, S.-A.; Jijie, R.; Nicoara, M.; Plavan, G.; Faggio, C. Micro- (nano) plastics in freshwater ecosystems: Abundance, toxicological impact and quantification methodology. TrAC Trends Anal. Chem.* **2019**, *110*, 116–128.

(125) *Wagner, S.; Reemtsma, T. Things we know and don`t know about nanoplastic in the environment. Nat. Nanotechnol.* **2019**, *14*, 300–301.

(126) *Nguyen, B.; Claveau-Mallet, D.; Hernandez, L. M.; Xu, E. G.; Farner, J. M.; Tufenkji, N. Separation and*

analysis of microplastics and nanoplastics in complex environmental samples. Acc. Chem. Res. **2019**, *52*, 858-866.

(127) *Felsing, S.; Kochleus, C.; Buchinger, S.; Brennholt, N.; Stock, F.; Reifferscheid, G. A new approach in separating microplastics from environmental samples based on their electrostatic behavior. Environ. Pollut.* **2018**, *234*, 20-28.

(128) *Wu, J.; Jiang, R.; Lin, W.; Ouyang, G. Effect of salinity and humic acid on the aggregation and toxicity of polystyrene nanoplastics with different functional groups and charges. Environ. Pollut.* **2019**, *245*, 836-843.

(129) *Li, Y.; Wang, X.; Fu, W.; Xia, X.; Liu, C.; Min, J.; Zhang, W.; Crittenden, J. C. Interactions between nano/micro plastics and suspended sediment in water: Implications on aggregation and settling. Water Res.* **2019**, *161*, 486-495.

(130) *Deshiikan, S. R.; Eschenazi, E.; Papadopoulos, K. D. Transport of colloids through porous beds in the presence of natural organic matter. Colloids Surf. A Physicochem. Eng. Asp.* **1998**, *145*, 93-100.

(131) *Oriekhova, O.; Stoll, S. Heteroaggregation of nanoplastic particles in the presence of inorganic*

colloids and natural organic matter. Environ. Sci. Nano **2018**, *5*, 792–799.

(132) *Amirbahman, A.; Olson, T. M. The role of surface conformations in the deposition kinetics of humic matter-coated colloids in porous media. Colloids Surf. A Physicochem. Eng. Asp.* **1995**, *95*, 249–259.

(133) *Novotna, K.; Cermakova, L.; Pivokonska, L.; Cajthaml, T.; Pivokonsky, M. Microplastics in drinking water treatment – Current knowledge and research needs. Sci. Total Environ.* **2019**, *667*, 730–740.

(134) *Jeon, H.; Lee, H.; Kang, K. H.; Lim, G. Ion concentration polarization-based continuous separation device using electrical repulsion in the depletion region. Sci. Rep.* **2013**, *3*, 3483.

(135) *McDonald, J. C.; Duffy, D. C.; Anderson, J. R.; Chiu, D. T.; Wu, H.; Schueller, O. J. A.; Whitesides, G. M. Fabrication of microfluidic systems in poly(dimethylsiloxane). Electrophoresis* **2000**, *21*, 27–40.

(136) *Galloway, M.; Stryjewski, W.; Henry, A.; Ford, S. M.; Llopis, S.; McCarley, R. L.; Soper, S. A. Contact conductivity detection in poly(methyl methacylate)-based microfluidic devices for analysis of mono- and polyanionic molecules. Anal. Chem.* **2002**, *74*, 2407–

2415.

(137) Yoon, E.; Davies, C. D.; Hooper, T. A.; Crooks, R. M. Photoelectrochemical ion concentration polarization: Membraneless ion filtration based on light-driven electrochemical reactions. *Lab Chip* **2017**, *17*, 2491-2499.

(138) Son, S. Y.; Lee, S.; Lee, H.; Kim, S. J. Engineered nanofluidic preconcentration devices by ion concentration polarization. *BioChip J.* **2016**, *10*, 251-261.

(139) Ko, S. H.; Song, Y.-A.; Kim, S. J.; Kim, M.; Han, J.; Kang, K. H. Nanofluidic preconcentration device in a straight microchannel using ion concentration polarization. *Lab Chip* **2012**, *12*, 4472-4482.

(140) Kim, S. J.; Li, L. D.; Han, J. Amplified electrokinetic response by concentration polarization near nanofluidic channel. *Langmuir* **2009**, *25*, 7759-7765.

(141) Swaminathan, V. V.; Gibson, L. R.; Pinti, M.; Prakash, S.; Bohn, P. W.; Shannon, M. A. Ionic transport in nanocapillary membrane systems. *J. Nanopart. Res.* **2012**, *14*, 951.

(142) Sheridan, E.; Hlushkou, D.; Knust, K. N.; Tallarek, U.; Crooks, R. M. Enrichment of cations via bipolar

electrode focusing. Anal. Chem. **2012**, *84*, 7393–7399.

(143) *Sheridan, E.; Knust, K. N.; Crooks, R. M. Bipolar electrode depletion: Membraneless filtration of charged species using an electrogenerated electric field gradient. Analyst* **2011**, *136*, 4134–4137.

(144) *Knust, K. N.; Sheridan, E.; Anand, R. K.; Crooks, R. M. Dual-channel bipolar electrode focusing: Simultaneous separation and enrichment of both anions and cations. Lab Chip* **2012**, *12*, 4107–4114.

(145) *Loget, G.; Zigah, D.; Bouffier, L.; Sojic, N.; Kuhn, A. Bipolar electrochemistry: From materials science to motion and beyond. Acc. Chem. Res.* **2013**, *46*, 2513–2523.

(146) *Mavré, F.; Chow, K.-F.; Sheridan, E.; Chang, B.-Y.; Crooks, J. A.; Crooks, R. M. A theoretical and experimental framework for understanding electrogenerated chemiluminescence (ECL) emission at bipolar electrodes. Anal. Chem.* **2009**, *81*, 6218–6225.

(147) *Knappenberger, T.; Aramrak, S.; Flury, M. Transport of barrel and spherical shaped colloids in unsaturated porous media. J. Contam. Hydrol.* **2015**, *180*, 69–79.

(148) *Duffy, D. C.; McDonald, J. C.; Schueller, O. J. A.; Whitesides, G. M. Rapid prototyping of microfluidic*

systems in poly(dimethylsiloxane). Anal. Chem. **1998**, *70*, 4974–4984.

(149) *Pundik, T.; Rubinstein, I.; Zaltzman, B. Bulk electroconvection in electrolyte. Phys. Rev. E* **2005**, *72*, 61502.

(150) *Dulin, D.; Le Gall, A.; Perronet, K.; Soler, N.; Fourmy, D.; Yoshizawa, S.; Bouyer, P.; Westbrook, N. Reduced photobleaching of BODIPY-FL. Phys. Procedia* **2010**, *3*, 1563–1567.

(151) *Rubinstein, I.; Zaltzman, B. Equilibrium electroconvective instability. Phys. Rev. Lett.* **2015**, *114*, 114502.

(152) *Kwak, R.; Guan, G.; Peng, W. K.; Han, J. Microscale electrodialysis: Concentration profiling and vortex visualization. Desalination* **2013**, *308*, 138–146.

(153) *Pham, S. V; Kwon, H.; Kim, B.; White, J. K.; Lim, G.; Han, J. Helical vortex formation in three-dimensional electrochemical systems with ion-selective membranes. Phys. Rev. E* **2016**, *93*, 033114.

(154) *Kim, S. J.; Ko, S. H.; Kwak, R.; Posner, J. D.; Kang, K. H.; Han, J. Multi-vortical flow inducing electrokinetic instability in ion concentration polarization layer. Nanoscale* **2012**, *4*, 7406–7410.

(155) *Herr, A. E.; Molho, J. I.; Santiago, J. G.; Mungal,*

M. G.; Kenny, T. W.; Garguilo, M. G. Electroosmotic capillary flow with nonuniform zeta potential. *Anal. Chem.* **2000**, *72*, 1053–1057.

(156) Kirby, B. J.; Hasselbrink, E. F. Zeta potential of microfluidic substrates: 1. Theory, experimental techniques, and effects on separations. *Electrophoresis* **2004**, *25*, 187–202.

(157) Huang, K.-D.; Yang, R.-J. A nanochannel-based concentrator utilizing the concentration polarization effect. *Electrophoresis* **2008**, *29*, 4862–4870.

(158) Dumitrescu, I.; Anand, R. K.; Fosdick, S. E.; Crooks, R. M. Pressure-driven bipolar electrochemistry. *J. Am. Chem. Soc.* **2011**, *133*, 4687–4689.

(159) Pham, V. S.; Li, Z.; Lim, K. M.; White, J. K.; Han, J. Direct numerical simulation of electroconvective instability and hysteretic current-voltage response of a permselective membrane. *Phys. Rev. E* **2012**, *86*, 046310.

(160) Mishchuk, N. A.; Takhistov, P. V. Electroosmosis of the second kind. *Colloids Surf. A Physicochem. Eng. Asp.* **1995**, *95*, 119–131.

(161) Mishchuk, N. A. Electro-osmosis of the second kind near the heterogeneous ion-exchange membrane. *Colloids Surf. A Physicochem. Eng. Asp.* **1998**, *140*,

75–89.

(162) *Cho, I.; Sung, G. Y.; Kim, S. J. Overlimiting current through ion concentration polarization layer: Hydrodynamic convection effects. Nanoscale* **2014**, *6*, *4620–4626.*

(163) *Kim, S.; Ganapathysubramanian, B.; Anand, R. K. Concentration enrichment, separation, and cation exchange in nanoliter-scale water-in-oil droplets. J. Am. Chem. Soc.* **2020**, *142*, *3196–3204.*

(164) *Phan, D.-T.; Shaegh, S. A. M.; Yang, C.; Nguyen, N.-T. Sample concentration in a microfluidic paper-based analytical device using ion concentration polarization. Sens. Actuators B Chem.* **2016**, *222*, *735–740.*

(165) *Choi, J.; Huh, K.; Moon, D. J.; Lee, H.; Son, S. Y.; Kim, K.; Kim, H. C.; Chae, J.-H.; Sung, G. Y.; Kim, H.-Y.; Hong, J. W.; Kim, S. J. Selective preconcentration and online collection of charged molecules using ion concentration polarization. RSC Adv.* **2015**, *5*, *66178–66184.*

(166) *Liu, L.; Xie, M.-R.; Chen, Y.-Z.; Wu, Z.-Y. Simultaneous electrokinetic stacking and separation of anionic and cationic species on a paper fluidic channel. Lab Chip* **2019**, *19*, *845–850.*

(167) Dhopeshwarkar, R.; Crooks, R. M.; Hlushkou, D.; Tallarek, U. Transient effects on microchannel electrokinetic filtering with an ion-permselective membrane. *Anal. Chem.* **2008**, *80*, 1039–1048.

(168) Davies, C. D.; Yoon, E.; Crooks, R. M. Continuous redirection and separation of microbeads via faradaic ion concentration polarization. *ChemElectroChem* **2018**, *5*, 877–884.

(169) Anand, R. K.; Johnson, E. S.; Chiu, D. T. Negative dielectrophoretic capture and repulsion of single cells at a bipolar electrode: The impact of faradaic ion enrichment and depletion. *J. Am. Chem. Soc.* **2015**, *137*, 776–783.

(170) Li, M.; Anand, R. K. High-throughput selective capture of single circulating tumor cells by dielectrophoresis at a wireless electrode array. *J. Am. Chem. Soc.* **2017**, *139*, 8950–8959.

(171) Davies, C. D.; Johnson, S. E.; Crooks, R. M. Effect of chloride oxidation on local electric fields in microelectrochemical systems. *ChemElectroChem* **2019**, *6*, 4867–4876.

(172) Burke, J. M.; Huang, Z.; Ivory, C. F. Simultaneous separation of negatively and positively charged species in dynamic field gradient focusing using a

dual polarity electric field. Anal. Chem. **2009**, *81*, 8236-8243.

(173) *Meighan, M. M.; Staton, S. J. R.; Hayes, M. A. Bioanalytical separations using electric field gradient techniques. Electrophoresis* **2009**, *30*, 852-865.

(174) *Courtney, M.; Ren, C. L. Counterflow gradient electrophoresis for focusing and elution. Electrophoresis* **2019**, *40*, 643-658.

(175) *Crooks, R. M. Principles of bipolar electrochemistry. ChemElectroChem* **2016**, *3*, 357-359.

(176) *Tandon, V.; Bhagavatula, S. K.; Nelson, W. C.; Kirby, B. J. Zeta potential and electroosmotic mobility in microfluidic devices fabricated from hydrophobic polymers : 1 . The origins of charge. Electrophoresis* **2008**, *29*, 1092-1101.

(177) *Takayama, S.; McDonald, J. C.; Ostuni, E.; Liang, M. N.; Kenis, P. J. A.; Ismagilov, R. F.; Whitesides, G. M. Patterning cells and their environments using multiple laminar fluid flows in capillary networks. Proc. Natl. Acad. Sci.* **1999**, *96*, 5545-5548.

(178) *Takayama, S.; Ostuni, E.; LeDuc, P.; Naruse, K.; Ingber, D. E.; Whitesides, G. M. Subcellular positioning of small molecules. Nature* **2001**, *411*,

1016.

(179) Holden, M. A.; Kumar, S.; Castellana, E. T.; Beskok, A.; Cremer, P. S. Generating fixed concentration arrays in a microfluidic device. *Sens. Actuators B Chem.* **2003**, *92*, 199–207.

(180) Seong, G. H.; Crooks, R. M. Efficient mixing and reactions within microfluidic channels using microbead-supported catalysts. *J. Am. Chem. Soc.* **2002**, *124*, 13360–13361.

(181) Sia, S. K.; Whitesides, G. M. Microfluidic devices fabricated in poly(dimethylsiloxane) for biological studies. *Electrophoresis* **2003**, *24*, 3563–3576.

(182) Ramette, R. W.; Culberson, C. H.; Bates, R. G. Acid-base properties of tris(hydroxymethyl)aminomethane (Tris) buffers in sea water from 5 to 40 °C. *Anal. Chem.* **1977**, *49*, 867–870.

(183) Li, Z.; Liu, W.; Gong, L.; Zhu, Y.; Gu, Y.; Han, J. Accurate multi-physics numerical analysis of particle preconcentration based on ion concentration polarization. *Int. J. Appl. Mech.* **2017**, *09*, 1750107.

(184) Ehlert, S.; Hlushkou, D.; Tallarek, U. Electrohydrodynamics around single ion-permselective glass beads fixed in a microfluidic device. *Microfluid. Nanofluidics* **2008**, *4*, 471–487.

(185) Huang, X.; Gordon, M. J.; Zare, R. N. Current-monitoring method for measuring the electroosmotic flow rate in capillary zone electrophoresis. *Anal. Chem.* **1988**, *60*, 1837–1838.

(186) Kenig, E. Y.; Su, Y.; Lautenschleger, A.; Chasanis, P.; Grünewald, M. Micro-separation of fluid systems: A state-of-the-art review. *Sep. Purif. Technol.* **2013**, *120*, 245–264.

(187) Smejkal, P.; Bottenus, D.; Breadmore, M. C.; Guijt, R. M.; Ivory, C. F.; Foret, F.; Macka, M. Microfluidic isotachophoresis: A review. *Electrophoresis* **2013**, *34*, 1493–1509.

(188) Giordano, B. C.; Burgi, D. S.; Hart, S. J.; Terray, A. On-line sample pre-concentration in microfluidic devices: A review. *Anal. Chim. Acta* **2012**, *718*, 11–24.

(189) Tetala, K. K. R.; Vijayalakshmi, M. A. A review on recent developments for biomolecule separation at analytical scale using microfluidic devices. *Anal. Chim. Acta* **2016**, *906*, 7–21.

(190) Roelofs, S. H.; Kim, B.; Eijkel, J. C. T.; Han, J.; Berg, A. van den; Odijk, M. Capacitive deionization on-chip as a method for microfluidic sample preparation. *Lab Chip* **2015**, *15*, 1458–1464.

(191) Kwak, R.; Pham, V. S.; Kim, B.; Chen, L.; Han, J.

Enhanced salt removal by unipolar ion conduction in ion concentration polarization desalination. Sci. Rep. **2016**, *6*, 25349.

(192) *Kim, B.; Kwak, R.; Kwon, H. J.; Pham, V. S.; Kim, M.; Al-Anzi, B.; Lim, G.; Han, J. Purification of high salinity brine by multi-stage ion concentration polarization desalination. Sci. Rep.* **2016**, *6*, 31850.

(193) *Yeh, S. H.; Chou, K.-H.; Yang, R.-J. Sample pre-concentration with high enrichment factors at a fixed location in paper-based microfluidic devices. Lab Chip* **2016**, *16*, 925–931.

(194) *Yoon, J.; Cho, Y.; Lee, J. H.; Chung, S. Tunable sheathless microfluidic focusing using ion concentration polarization. Appl. Phys. Lett.* **2015**, *107*, 083507.

(195) *Kim, W.; Park, S.; Kim, K.; Kim, S. J. Experimental verification of simultaneous desalting and molecular preconcentration by ion concentration polarization. Lab Chip* **2017**, *17*, 3841–3850.

(196) *Wei, X.; Panindre, P.; Zhang, Q.; Song, Y.-A. Increasing the detection sensitivity for DNA-morpholino hybridization in sub-nanomolar regime by enhancing the surface ion conductance of PEDOT:PSS membrane in a microchannel. ACS Sens.* **2016**, *1*, 862–

865.

(197) Kim, M.; Jia, M.; Kim, T. Ion concentration polarization in a single and open microchannel induced by a surface-patterned perm-selective film. *Analyst* **2013**, *138*, 1370–1378.

(198) Yang, R.-J.; Pu, H.-H.; Wang, H.-L. Ion concentration polarization on paper-based microfluidic devices and its application to preconcentrate dilute sample solutions. *Biomicrofluidics* **2015**, *9*, 014122.

(199) Kuhn, A.; Crooks, R. M.; Inagi, S. A compelling case for bipolar electrochemistry. *ChemElectroChem* **2016**, *3*, 351–352.

(200) Lifshitz, A.; Perlmutter-Hayman, B. The kinetics of the hydrolysis of chlorine. I. Reinvestigation of the hydrolysis in pure water. *J. Phys. Chem.* **1960**, *64*, 1663–1665.

(201) Spalding, C. W. Reaction kinetics in the absorption of chlorine into aqueous media. *AIChE J.* **1962**, *8*, 685–689.

(202) Wang, T. X.; Margerum, D. W. Kinetics of reversible chlorine hydrolysis: Temperature dependence and general-acid/base-assisted mechanisms. *Inorg. Chem.* **1994**, *33*, 1050–1055.

(203) Black and Veatch Corporation. White`s handbook of

chlorination and alternative disinfectants, 5th ed.; Desiderio, D. M., Nibbering, N. M. M., Eds.; Wiley: Hoboken, 2010.

(204) Johnson, D. E.; Enke, C. G. Bipolar pulse technique for fast conductance measurements. Anal. Chem. **1970**, *42, 329-335.*

(205) Shadpour, H.; Hupert, M. L.; Patterson, D.; Liu, C.; Galloway, M.; Stryjewski, W.; Goettert, J.; Soper, S. A. Multichannel microchip electrophoresis device fabricated in polycarbonate with an integrated contact conductivity sensor array. Anal. Chem. **2007**, *79, 870-878.*

(206) Breiter, M. W. Voltammetric study of halide ion adsorption on platinum in perchloric acid solutions. Electrochim. Acta **1963**, *8, 925-935.*

(207) Patil, R. S.; Juvekar, V. A.; Naik, V. M. Oxidation of chloride ion on platinum electrode: Dynamics of electrode passivation and its effect on oxidation kinetics. Ind. Eng. Chem. Res. **2011**, *50, 12946-12959.*

(208) LeSuer, R. J.; Fan, F.-R. F.; Bard, A. J. Scanning electrochemical microscopy, 52. Bipolar conductance technique at ultramicroelectrodes for resistance measurements. Anal. Chem. **2004**, *76, 6894-6901.*

(209) Rosen, M.; Flinn, D. R.; Schuldiner, S. Double layer

capacitance on platinum in 1 M H_2SO_4 from the reversible hydrogen potential to the oxygen formation region. J. Electrochem. Soc. **1969**, *116*, 1112–1116.

(210) *Bard, A. J.; Faulkner, L. R. Electrochemical methods: Fundamentals and applications, 2nd ed.; Wiley: New York, 2001; Vol. 2nd.*

(211) *Goldin, M. M.; Volkov, A. G.; Khubutiya, M. S.; Kolesnikov, V. A.; Blanchard, G. J.; Evseev, A. K.; Goldin, M. M.; Teselkin, Y. O.; Davydov, B. V. Redox potential measurement in aqueous solutions and biological media. ECS Trans.* **2008**, *11*, 39–49.

(212) *Park, J. H.; Zhou, H.; Percival, S. J.; Zhang, B.; Fan, F.-R. F.; Bard, A. J. Open circuit (mixed) potential changes upon contact between different inert electrodes-Size and kinetic effects. Anal. Chem.* **2013**, *85*, 964–970.

(213) *Yue, Y.; Huo, F.; Yin, C.; Escobedo, J. O.; Strongin, R. M. Recent progress in chromogenic and fluorogenic chemosensors for hypochlorous acid. Analyst* **2016**, *141*, 1859–1873.

(214) *Davies, C. W. 397. The extent of dissociation of salts in water. Part VIII. An equation for the mean ionic activity coefficient of an electrolyte in water, and a revision of the dissociation constants*

of some sulphates. *J. Chem. Soc.* **1938**, 2093–2098.

(215) Goldberg, R. N.; Kishore, N.; Lennen, R. M. Thermodynamic quantities for the ionization reactions of buffers. *J. Phys. Chem. Ref. Data* **2002**, *31*, 231–370.

(216) Kim, Y. H.; Hensley, R. Effective control of chlorination and dechlorination at wastewater treatment plants using redox potential. *Water Environ. Res.* **1997**, *69*, 1008–1014.

(217) Brezonik, P. L.; Arnold, W. Water chemistry : An introduction to the chemistry of natural and engineered aquatic systems. Oxford University Press USA - OSO: Cary, 2011.

(218) Percival, S. J.; Bard, A. J. Ultra-sensitive potentiometric measurements of dilute redox molecule solutions and determination of sensitivity factors at platinum ultramicroelectrodes. *Anal. Chem.* **2017**, *89*, 9843–9849.

(219) James, C. N.; Copeland, R. C.; Lytle, D. A. Relationships between oxidation-reduction potential, oxidant, and pH in drinking water. In *Proceedings of the American Water Works Association Water Quality Technology Conference*; San Antonio, 2004; pp 1–13.